Biomimetic Materials for Hydrogen Production

Samantha L. Peralta-Arriaga

A thesis submitted to the University of Sheffield in partial fulfilment of the requirements for the degree of Doctor of Philosophy

March 2022

Department of Chemistry
University of Sheffield

Abstract

The urgency for new clean technologies for producing renewable fuels has put hydrogen production via photocatalysis and photoelectrochemical (PEC) processes as a viable promising clean technology.[8] Despite all the advances in the development of new systems for hydrogen evolution from water using different hydrogenases with different photosensitizers and semiconductors, there remains a lot of opportunities and questions to be answered to create new and more efficient systems for hydrogen evolution through water splitting via PEC and understand better their mechanism.

This work presents the results obtained in the study of a new biomimetic hybrid photocatalytic system for hydrogen production composed by a highly efficient visible light-absorbing copper complex as photosensitiser (PS) linked to a semiconductor (SC) surface, using a [FeFe] hydrogenase mimic complex as a catalyst for hydrogen production from water splitting via PEC. The newly sensitized hydrogenase mimic FeFe complex $Fe_2(dpet)(CO)_6$ was studied in chapter 3 which describes the photophysical and photoelectrochemical characterization and confirm its efficiency as a co catalyst for proton reduction. The results shown in chapter 4, confirmed that the use of dopants such as Cu and Ni can tune the energy bands of the SC making it suitable for electron transfer (ET) from the PS. Chapter 5, describes the synthesis and characterization of a new Cu complex and proposes it is used as PS in photoanodes. Moreover, this application was studied in chapter 6 where it is confirmed that the use of the Cu complex $[Cu(xantphos)(biq\text{-}COOH)]^+$ is possible and meets with the requirements for its application as PS decreasing the recombination processes on the SC and proposed its application on hydrogen evolution via PEC.

Acknowledgements

I would like to thank first to my supervisor Prof. Julia Weinstein for giving me the opportunity to come to her research group to work, for allowing me to develop the proposed project and of course all the support and guidance through all these years. Secondly to CONACYT-SENER for awarded me with the funding for this project (Grant number 472714).Thanks “Tia Cony”.

To all my friends and colleagues from Weinstein group Andy Sadler, Marta M. Martinez, Isuru Muthukudaarachchi, Luke Price, Callum Jones, Heather Carson, Martin Appleby, Simon Parker, James Shipp, Alex Auty, Catherine Royle, Tao Cheng, Evie Karkera, Scarlet Coddington, Guanzhi Wu, Rory Cowin, Iona Iovalo, Ricardo Fernandez-Teran. For all your support, friendship for your guidance and making my days fun and happy, creating an amazing environment work. Thanks guys!!!!

To all my friends form the department the CPGS team: Amelia C Wood, Benedict J Smith, Freya Cleasby, Nikki Mansouri, Alice Rhind-Tutt, Aysha Mehter, Mengyuan Qian, Sophia Van Mourik, Robert Shaw. Also, to my only Chemistry Department Mexican friend Fernando Lopez for speaking Mexican with me, To Arthur Graph for all those tasty noodle lunches. To all those people who contributed in one or another way in my development and made of this an amazing journey.

To all the amazing people who supported me in Mexico to come here, to all my friends and colleagues. To my Sheffield family for always being there and support me. of course, a big thanks to my family for always believe in me for all their support. To my beautiful sister Gaby Peralta, I love you and I want to thank you for all the support you give me and the right words whenever I need them. To my amazing father David Peralta for never let me give up, for always been there for listening to me and support me with love and for believe in me always, I love you!

And lastly, I want to dedicate all this entire work to my mother Oralia Arriaga, who lost the battle against cancer in 2018. Thank you for encouraging me to come and pursue my dreams thanks for teaching me to dream big and follow those dreams for always believe in me, for making me a strong, stubborn, and determined women. This was the last thing you asked me to do, to come and finish my PhD. Well, Mom I did it!!!

In memory of my beloved Mommy, Oralia Arriaga.

Acknowledgement of collaborative work within the thesis

I want to thank to all the people that helped me through the development of this project, and for this I will describe the collaborations in each chapter.

Chapter 3

First, I would like to thank to **Dr. Michael M. Morris** and his research group for their contribution synthetizing the $Fe_2(dpet)(CO)_6$ complex and allowing me to investigate its application as catalyst for proton reduction. Secondly, to all my colleagues that helped me to conduct some of the experimental work in this chapter. To **James D. Shipp** for his help with the FOWA analysis and guidance with the Spectro electrochemistry experiments. To **Simon Parker** for his guidance with the electrochemical characterization. To **Catherine Royle** for the Transient Absorption analysis and in collaboration with **Alex Auty** for teaching me how to process the data. To **Ricardo Rodriguez-Teran** for his help with the DFT analysis and the setup of the "Ricarduino" for the photostability experiments.

Chapter 4

The synthesis of the aluminates was conducted in The Department of Chemical & Biological Engineering, thanks to **Duncan Schofield**, Assistant Engineering Technician for his training and help with the furnace.

This chapter was conducted in collaboration with the **Eco materials and Energy Department** at **University of Nuevo Leon** in Monterrey Mexico. From this collaboration I would like to thank to **Dra. Leticia Torres-Martínez, Dr. Isaías Martínez, Dra. Edith Luevano** and **Dr. Luis Felipe Garay Rodriguez** for conducting the hydrogen evolution tests and the impedance measurements.

To **Craig Robertson**, X-ray Crystallography Service Manager and NMR Service Support for the XRD analysis and to **Deborah Hammond**, Experimental Officer at The Sheffield Surface Analysis Centre Surface Facility for conducting the XPS analysis, both within the Department of Chemistry.

Chapter 5

This chapter was part of the Master thesis project of **Evie Karkera** to whom I want to massively thank for her enthusiasm and hard work in synthesizing and characterizing the Cu complexes studied in this chapter. To **Martin Appleby** for all his support and guidance in the synthesis and purification of the Cu complexes.

Chapter 6

Dr. Marco Conte and group for their help and facilitated me to use their furnace for the preparation of the films.

To **Dr. Jonathan Foster** and his research group for their help in specific to **Jiangtian Tan (Andy)** for his help with the Spin coater. To **Benedict Smith** with the assistance and conducting some the AFM analysis. To **Freya Cleasby** for the SEM and EDX analysis. And to **Dr David Owen** for training me on the use of the XPS. And latest but not less important to **Dr Alex Auty** for the TA analysis on the films.

Contents

Appendices

List of abbreviations

“H-cluster”	**Active site of hydrogenases**
μJ	microjoules
$\mu mol\ H_2 \cdot g^{-1}$	Micromoles of Hydrogen per gram
A	Acceptor
AFM	Atomic Force Microscopy
Ag/AgCl	Silver/Silver Chloride
AP	Artificial Photosynthesis
APS	Artificial photosynthetic systems
CB	Conduction band
cm^{-1}	wavenumbers
CO	Carbonyl group
CT	Charge Transfer
CV	Cyclic Voltammetry
D	Donor
DCM	Dichloromethane
DFT	Density functional theory
DSSC	Dye Sensitized Solar Cells
E	potential of the electrochemical cell
E_0	standard potential
EDS	Electronic diffraction scanning
E_{fb}	Fermi level potential
Eg	Bandgap
EIS	Electrochemical Impedance Spectroscopy
ET	Electron Transfer
eV	Electron volt
F	Faraday constant
F(R)	Function of reflectance
Fc^0/Fc^+	Ferrocene/ferrocenium redox couple
FOWA	foot-of-the-wave analysis
FRA	Frequency analyser
fs	femtoseconds
FTIR	Fourier Transform Infrared Spectroscopy

FWHM	full width at half maximum
$g \bullet mm^{-1}$	Grams per millimetre
Gt	Gigatons
HOMO	Highest Occupied Molecular Orbital
IC	Internal conversion
IEA	International Energy agency
ISC	Intersystem crossing
JCPDS	Joint Committee on Powder Diffraction Standards
K	Kelvin
K_S	Equilibrium constant of the interaction between the emissive molecule and the quencher in the ground state.
LLCT	Ligand-To-Ligand Charge Transfer
LMCT	Ligand-To-Metal Charge Transfer
LUMO	Lower Unoccupied Molecular Orbital
M	molar
M*	Emissive state
m/z	Mass-to-charge ratio
MC	Metal Centered
MeCN	Acetonitrile
MHz	Megahertz
MJ /kg	Megajoules per kilogram
MLCT	Metal-To-Ligand Charge Transfer
mM	millimolar
Mtoe	Million tonnes of oil equivalent
$mV\ s^{-1}$	millivolts per second
mV/s	Millivolts per second
ν	Frequency
n	Number of electrons
nm	nanometres
NMR	Nuclear Magnetic Resonance
OD	Optical Density
PDF	powder diffraction file
PEC	Photoelectrochemical

ppm	Parts per million
PS	Photosensitizer
ps	picoseconds
PV	Photovoltaics
Q	Quencher molecule
R	Gas constant
S_0	ground electronic singlet state
S1	First singlet excited state
S2	Second singlet excited state
SC	Semiconductor
SEC	Spectroelectrochemistry
SEM	Scanning Electron Microscopy
T	temperature
T1	Triplet excited state
TA	Transient Absorption
$TBAPF_6$	Tetrabutylammonium hexafluorophosphate
TCD	Thermal conductivity detector
TFA	Trifluoro acetic acid
TM	Transition Metal
TOF	turnover frequencies
TOF_0	turnover frequency at zero overpotential
TW	Terawatts
UV	Ultraviolet
V	volts
VB	Valence band
VC	Vibrational cooling
VR	Vibrational relaxation
W/m^2	Watts per square meter
WT%	Weight Percentage
XPS	X-ray photoelectron spectroscopy
XRD	X-Ray Diffraction
ΔA	Differential absorption
$\Delta G^{\#}$	free activation energy

ΔG_{et}	free energy charge of electron transfer
ΔG^{o}	Gibbs free energy
ε	Extinction coefficient
τ	Lifetime decay constant
λ	Reorganisation energy
k_q	Rate constant for the excited state quenching reaction.
a_{red}	Activities of the reduced species in solution
a_{ox}	Activities of the oxidized species in solution

Chapter 1

Introduction

1.1 List of Figures

1.2 Overview of energy crisis

Nowadays, one of the main challenges is overcoming adverse impacts of climate change whilst achieving economic development, where the energy factor is one of the most important contributors. The use of fossil fuels and the increasing energy demand are the principal causes of environmental problems, but producing more energy is still an essential factor for economic and social development to increase the quality of life across all countries.

In 2015, UNESCO set out 17 Development goals for sustainable development in the 2015-2030 agenda where Goal 7 is to ensure "Affordable and clean energy for everyone".[1]

In 2020 the world experienced a terrible pandemic that triggered an unprecedented macroeconomic shock in peacetime. The current COVID-19 pandemic is above all a global crisis with 274,628,461 confirmed cases and 5,358,978 deaths due to the illness to the 21st of December of 2021, as it is reported by the World Health Organization, affecting more than 200 countries.[2]

Beyond the noticeable impact on health worldwide, this crisis has impacted the global economies, energy, and CO_2 emissions. Countries on total lockdown experienced a 25% decline in energy demand per week, and countries in partial lockdown an average of 18% decline. The global energy demand declined by 3.8% or 150 million tonnes of oil equivalent (Mtoe) in the first quarter of 2020 due to the confinement measures enforced in Europe, North America and elsewhere relative to the first quarter of 2019. The worst decline in the last 70 years.[3]

The International Energy Agency (IEA) reported that an entire year energy demand could decline by around 6%, the equivalent to the combined energy demand of France, Germany, Italy, and the United Kingdom in 2019, and the equivalent to more than seven times the impact of the last financial crisis, reversing the growth of global energy demand over the last five years. Other primary energy sources like Oil (9%), Coal (8%), Gas and Nuclear were also affected in contrast with the demand for renewables expected to increase because of low operating costs and preferential access to many power systems.[4]

CO_2 emissions were 5% lower in the first quarter of 2020. Such a year-on-year reduction would be the largest ever, six times larger than the previous record reduction of 0.4 Gt in 2009 and twice as large as the combined total of all previous reductions since the end of World War II; this is associated with the decline in demand for coal at 8%, 4.5% from oil and 2.3% from natural gas.[3]

To put this in perspective, the impacts of COVID-19 on energy demand buys humanity another year of 'allowable' emissions before the 1.5 °C 2029 target and a couple of years before the 2 °C warming carbon budget is exhausted by 2050.

Before the pandemic it was estimated that a total global energy consumption will reach 108 Gt by 2050, however this event will change these predictions. The latest reports show that the impact of COVID will reduce the demand for energy by 8%, this will make the demand levels return to 2018 reported value (14420 Mt).

The latest report generated from the 26th UN Climate Change Conference of the Parties (COP26) in Glasgow in 2021 established that by 2050, almost 90% of electricity generation will come from renewable sources emphasising the importance of producing low emissions fuels such as hydrogen.[4]

Nevertheless, the urgency of developing new clean and sustainable energy sources remains one of the principal goals of humanity, and what we can learn from the last year is how our actions and lifestyle (footprint) have an impact on energy consumption and on CO_2 emissions that affect the negative impacts of climate change.

1.3 Use of renewable energies

Despite the impacts of the COVID-19 pandemic, renewable energies set a record in power generation capacity during 2020 with a growth of 3% and still increasing across all different sectors like power, heating, industry, and transport in 2021. The solar PV and wind are expected to contribute two-thirds of the renewable's growth.

Renewable energy use has been increasing during the last years, and it was set to expand more than 8% during 2021, representing 29% of the global energy generation during 2020, up from 27.3% in 2019.[5]

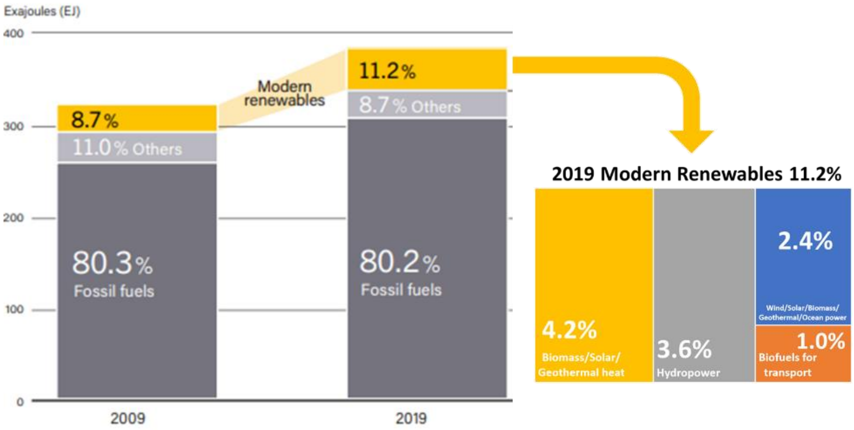

Figure 1. Estimated Renewable Share of Total Final Energy Consumption, 2009 and 2019, source: based on IEA data and reproduced from Ref.[6]

From the 11.2% of the total renewable energy used, only 4.2% use the sun as a primary energy source. However, solar energy represents the highest energy generation potential from renewable energy sources.

Table 1. Overview of global power generating capacities of sustainable energy sources.[7]

Energy source	Power (TW)	Remarks
Wind	4	Represents 10–15% of global technical potential for on- and off-shore installations
Hydroelectric	1-2	Remaining untapped potential is 0.5 TW
Tidal and ocean currents	<2	
Geothermal	12	Only a small fraction of this can be exploited
Nuclear	10	Requires construction of a 1-GW peak-power plant every 35 h for the next 40 years. Finite uranium supplies imply need for fast breeder or thorium reactors
Biomass	10	Requires 10% of earth’s land surface to be covered with switch grass.
Solar	>20	Requires 0.16% of the Earth’s surface to be covered with 10% efficient solar cells. Total solar power reaching the earth’s surface is 120,000 TW

Several technologies have been developed during the last decades using solar energy as the primary source, such as solar cells, solar thermal energy, and the production of hydrogen via photocatalytic process under solar radiation.

The hydrogen production has gained great importance in the last decade, especially with the potential application for energy storage or transportation.

Renewable hydrogen is non-toxic and much lighter than air and represents an excellent energy storage solution with an energy content of 141.8 MJ/kg at 298 K; this is much higher than most of the fuels, i.e., gasoline with a maximum of 44 MJ/kg at 298 K.[8]

There are different pathways to produce hydrogen; some are still in development, and most of them still use fossil fuels as the primary source of energy (see Table 2) more than 99% of global hydrogen is produced in actuality from fossil fuels.[6]

Table 2. Summary of hydrogen production process by category, feedstock, and technology available. [8]

Process	Energy I/P	Feedstock Hydrocarbons (H) Non-Hydrocarbons (N)	Technology	Eff(%)	Clean* (C/N/CCS)	Ref.
Electrolysis	Electric	Water(N)	Anion exchange	62-82	C	9–14
		Brine(N)	Proton exchange membrane	67-84	C	15–17
			Solid oxide cells	75-90	C	
			Chlor-alkali	NA	C	
Electro-Photolysis	Electric-Photonic	Water(N)	Photoelectrochemical	0.5-12	C	8,12,18–23
Photolysis	Photonic	Water(N)/Algae(H)	Photosynthesis	1.6-5	C/N	9,24,25
Bio photolysis	Bioenergy	Cyanobacteria	Photo-fermentation	<1	N	9,18,20,26–30
	Photonic	Photosynthetic-Bacteria	Algal Hydrogen	1-3	N	30
		Fat (H)		2-7	N	12,24,29–31
		Nutrients (H)		12-14	N	
Bio electrolysis	Bioenergy	Biomass(H)	Microbial electrolysis	70-80	N	9,32
	Electric	Hydrogenases	Nitrogen fixation	10	N	33
Biolysis	Bioenergy	Microorganism	Dark Fermentation	60-80	N	32,34
		Fermentative Bacteria	Hydrolysis	NA	N	28,35,36
		Biomass(H)+Water(N)	Aqueous phase reforming	35-55	N	9,37
		CO(N)+Water(N)	Biological shift reaction	NA	N	38
Bio-thermolysis	Bioenergy-Heat	Biomass(H)(microwave) acid pre-treated	Co-fermentation	NA	N	39,40
Thermolysis	Heat	Water (N)	Water thermolysis	20-55	C	9,27,32,41,42
		Biomass (H) (absence of O_2)	Pyrolysis	35-50	N	32,43
		Biomass (H)	Gasification	35-50	N	9,12,26
		Coal (H)	Coal gasification	74-85	N/CCS	34
		Fuels (H)	Steam reforming (SR)	60-85	N/CCS	**44–50**
		Fuels(H)	Membrane reactors	64-90	N/CCS	32,43,51
		Biomass (H)	Partial oxidation	60-75	N	9,26,32
		Methane (H) + CO_2	Autothermal	60-75	N	9,26,32,43
Thermo-electrolysis	Heat-Electric	Fuels(H)	Plasm Reforming	9-85	N	9,52–54
Chemical	Chemical reaction	Water(N)	Redox	3-5 wt.	C	24,55–58
		Metals(N)		NA		24,58,59
Radiolysis	Radiation	Hydrogen Peroxide (H_2O_2)	Radiolysis	NA	C	12,60–63

*Cleanness: Clean with no emissions (C), Non-Clean with emissions (N), Quasi-clean by using Carbon Capture and storage (CCS).

Among all those different approaches, molecular artificial photosynthesis has been receiving a lot of attention from the researchers across the world, with the intention to create systems that mimic green plants to produce chemicals and ultimately solar fuels. The artificial photosynthetic system would ideally utilize a wider region of the solar spectrum, using abundant and inexpensive materials and perform more efficiently for hydrogen production. Relevant approaches utilize coordination chemistry, materials science and nanoscience as well as modified bioengineered, synthetic biomimetic and bioinspired techniques to construct photo-semiconductors and systems based on enzymes.[64,65]

The photocatalytic route via water splitting using only water and sunlight as the hydrogen source ensures an entirely sustainable way to produce this valuable fuel.

As Jules Verne wrote 145 years ago in his book The Mysterious Island published in 1875.[66]

> *"Water will one day be employed as fuel, that hydrogen and oxygen which constitute it, used singly or together, will furnish an inexhaustible source of heat and light, of an intensity of which coal is not capable".*

For all the above, hydrogen production via photocatalysis and photoelectrochemical is considered a viable promising clean technology.[8]

1.4 Artificial photosynthesis

Artificial photosynthesis (AP) is the mimic of natural photosynthesis, and it is responsible for two main reactions: CO_2 reduction and water splitting for hydrogen production. It uses sunlight as the primary source of energy in both reactions.

Biomimicry is one of the research areas that aim to develop technologies based on the principles used in Nature. According to Darwin's theory, *"Any being, if it varies however slightly in any manner profitable to itself, under the complex and sometimes varying conditions of life, will have a better chance of surviving, and thus be naturally selected. From the strong principle of inheritance, any selected variety will tend to propagate its new and modified form"*.[67]

One of the strategies to create new systems for efficient hydrogen production from water has been the development of biomimetic catalysis, which takes natural catalysts (enzymes) and creates functional molecular photosynthetic systems (Figure 2).

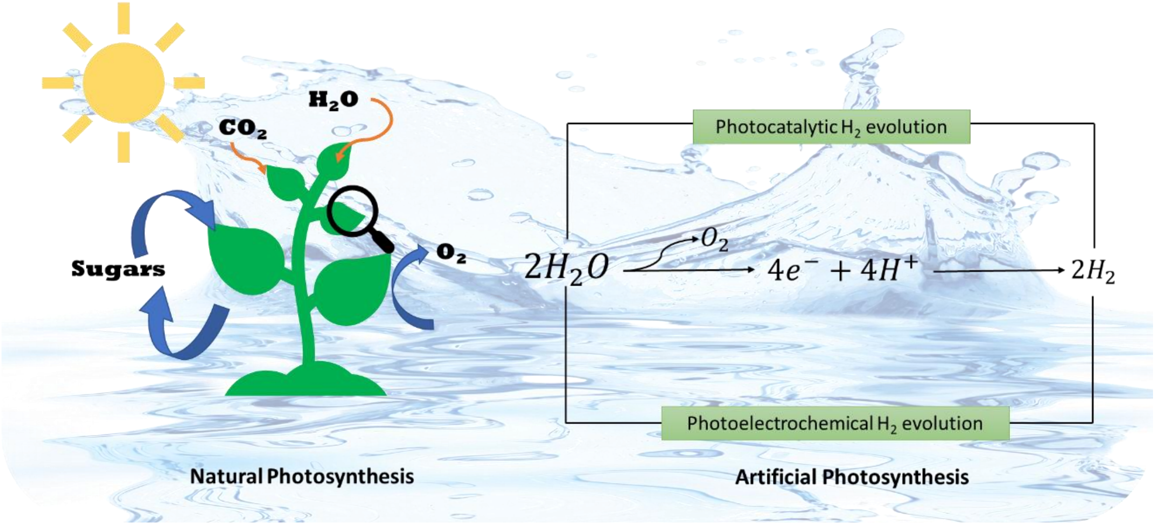

Figure 2. Illustration of the photosynthetic process in nature (left) vs. an artificial photosynthetic system for hydrogen production via photocatalytic and photo electrochemical processes.

The natural photosynthesis process is composed of two different reactions, some of which happen during the night and others during the day; these are called "dark" and "light" reactions. The "light" reactions are powered by the sunlight and involve water splitting and reducing the NADP$^+$ to NADPH for the water oxidation.

The water splitting takes place in the photosystem called PS-II, and the reduction of the NADP$^+$ in the photosystem called PS-I. Then these NADP$^+$/NADPH are used to fix the CO_2 and its conversion into carbon-based compounds like sugars: this process is not light-driven and therefore called “the dark cycle” (or the Calvin cycle). This process is done by a complex group of enzymes.[68] The total reaction of natural photosynthesis is thus the following. (Eq. 1)

$$\boldsymbol{H_2O + CO_2 \overset{hv}{\rightarrow} O_2 + \frac{1}{6}(C_6H_{12}O_6)}$$ Eq. 1 Photosynthesis, the sum reaction.

Artificial photosynthesis gets inspiration from the natural photosynthetic processes and replicates some of these reactions in a simplified way. For example, during the water splitting process (Eq. 2) two half reactions take place (i) the reduction of water; in which two protons are released (Eq. 3) that during the (ii) water oxidation process get reduced directly to produce molecular hydrogen (Eq. 4):

$$\boldsymbol{2H_2O \overset{hv}{\rightarrow} O_2 + 2H_2}$$ Eq. 2 Water splitting reaction.

$$\boldsymbol{2H_2O \rightarrow O_2 + 4H^+ + 4e^-}$$ Eq. 3 Water oxidation reaction

$$\boldsymbol{4H^+ + 4e^- \rightarrow 2H_2}$$ Eq. 4 Water reduction reaction

In Nature, the catalysts, so-called “enzymes” that are used for the conversion of protons to produce hydrogen are the hydrogenases. Many different artificial systems have been studied, both homogeneous and heterogeneous using these natural enzymes and complexes that mimic them.

1.5 Use of semiconductors for hydrogen evolution

In 1972, the first photoelectrochemical system using a semiconductor (SC) for water splitting was created by Honda and Fujishima using TiO_2 as an anode, and Pt-cathode to achieve water splitting in an electrochemical cell under UV light.[65]

To date, numerous semiconductors have been studied for their application in PEC water splitting, including tantalates ($NaTaO_3$, $LiTaO_3$[69–73]), oxides such as the classic TiO_2[25,74–76] and others, for example WO_3[77,78], Cu_2O[79], $BiVO_4$[80], Al_2O_3[81], Ga_2O_3, Ta_2O_5, CoO, and ZrO_2[82,83]. A wide range of perovskites such as $AgMO_3$ (M = Ta, Nb, V)[84], $LaFeO_3$[85], composites of different materials such as CdS/Au/TiO_2[86–88] or NiO/CdS@ZnO[89], ferrites ($NiFe_2O_4$[90,91]). Lately a lot of attention has been attracted to some aluminates such as MAl_2O_4 (M: Sr, Ba and Mg).[92,93] These aluminates have shown a good performance for photocatalytic hydrogen evolution with a maximum Solar-to-hydrogen (STH) efficiencies of 4% for the $MgAl_2O_4/Al_2O_3$ and 1.7% for the $MgAl_2O_4$. And a maximum production rate of 120 $\mu mol \cdot g^{-1}$ after 2hr of irradiation for the $MgAl_2O_4/Al_2O_3$. [93]

Nevertheless, this efficiency is still too low for practical applications, for example the efficiency in the solar panels is over 20%. There are a few different strategies to improve the efficiency of the semiconductors.

Since 1970, a wide variety of photosensitizers has been studied. Sun and co-workers reported the first dye-sensitized photocathode for PEC water splitting based on *p*-type NiO using cobalt complexes as PS.[94] Mallouk and co-workers proposed a dye-sensitized TiO_2 water-splitting cell with hydrated iridium oxide nanoparticles as the oxygen-evolving catalyst[95], porphyrins[96], dyes[97] and quantum dots.[98–100]

However, most of the studied systems so far use noble metals, and the low abundance of these materials will limit large-scale applications. Because of this disadvantage, the development and utilization of low-cost metal complexes based on Mn, Fe, and Ni, have gradually become the hot spot of this field.

1.6 Hybrid systems for water splitting

On the other hand, there is another approach to increase the efficiency in the photocatalytic hydrogen evolution: that is to use multicomponent systems were a photosensitizer is linked to the surface of a semiconductor, and different hydrogenases or hydrogenase mimics are used as catalysts for proton reduction.[101]

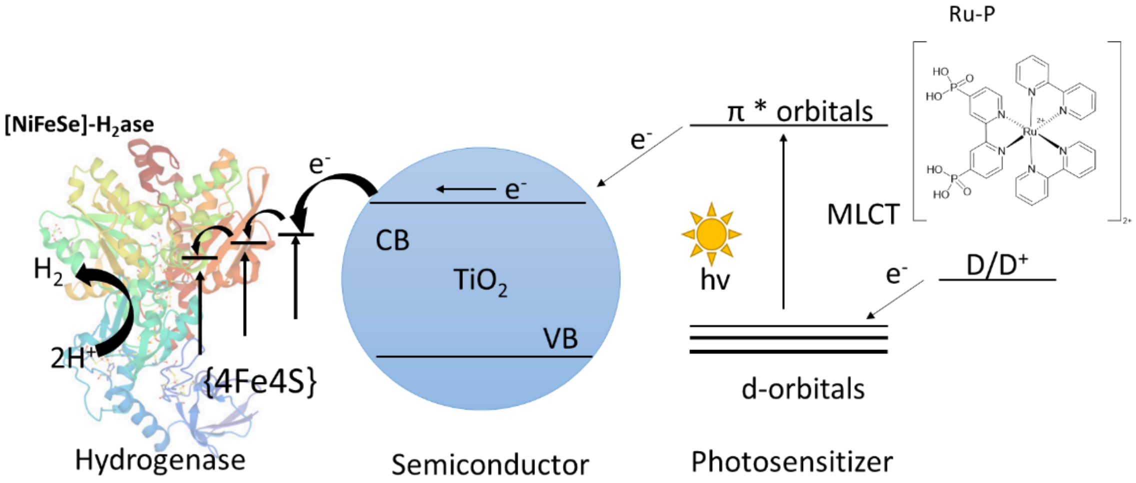

Figure 3. Schematic representation of visible-light driven H_2 evolution hybrid system formed by a PS, a SC, and a hydrogenase RuP–TiO_2-H_2ase, i.e., [NiFeSe]-H_2ase attached to RuP dye-sensitised TiO_2 nanoparticles.[101]

In general, three basic components are needed to create an efficient photochemical system for light driven hydrogen evolution. Those are: a good PS, a highly efficient proton reduction catalyst (in this case the [Fe-Fe]-hydrogenases), and an electron donor (D), Figure 4.

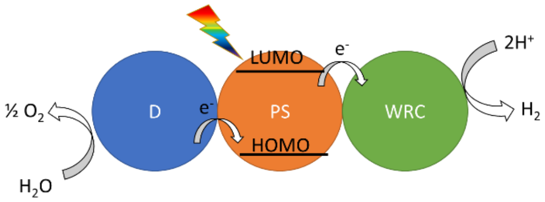

Figure 4. The main components of an artificial photosynthetic system

A closed photo redox catalytic cycle can proceed following two different pathways: an oxidative or a reductive one (Figure 5). Catalytic Fe_2 site proceed via oxidative quenching where the first step is the quenching of the *PS excited state by the donating an electron to the electron acceptor Fe_2 centre (Eq. 5), after this the PS is regenerated by electron transfer from the donor (D) (Eq. 6).

$\boldsymbol{PS^* - Fe_2 \rightarrow PS^+ - Fe_2^-}$ Eq. 5 Oxidative quenching reaction.

$\boldsymbol{PS^+ - Fe_2 + D \rightarrow PS - Fe_2^- + D^+}$ Eq. 6 PS regeneration reaction.

And at the reductive quenching is when the *PS excited state is quenched by accepting electron form the D as it is illustrated in (Figure 5).

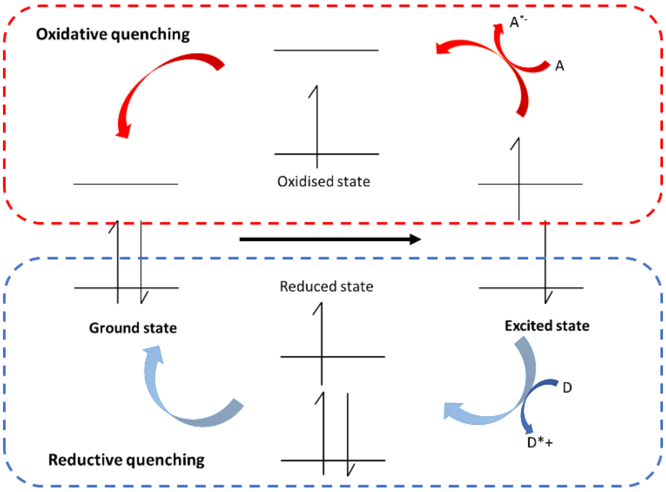

Figure 5. Deactivation of excited state via an oxidative and reductive quenching cycles Reproduced from Ref. J.Org.Chem.2012, 77, 1617−1622

The efficiency of this process is determined by the Gibbs free energy change (ΔGº) of the photoinduced electron transfer, which can be estimated according to the Rehm-Weller equation (Eq. 7).[102]

$$\Delta G^{\circ} = \boldsymbol{E_{ox}} - \boldsymbol{E_{red}} - \boldsymbol{E_{00}} - \boldsymbol{C}$$ Eq. 7 Rehm-Weller equation.

Where the $\boldsymbol{E_{ox}}$ is the oxidation potential of the species donating an electron, $\boldsymbol{E_{red}}$ is the reduction potential of the species accepting an electron, $\boldsymbol{E_{00}}$ is the excitation energy used, and $\boldsymbol{C}$ is the sum of the columbic energy of the formed ion pair in the solution and solvation effect.[103]

1.7 Photosensitizers

A photosensitizer is a molecule that absorbs light (hv) and transfers this energy from the source of light into another nearby molecule or a semiconductor through a series of photochemical processes including a series of internal electron transfer processes (Figure 6).

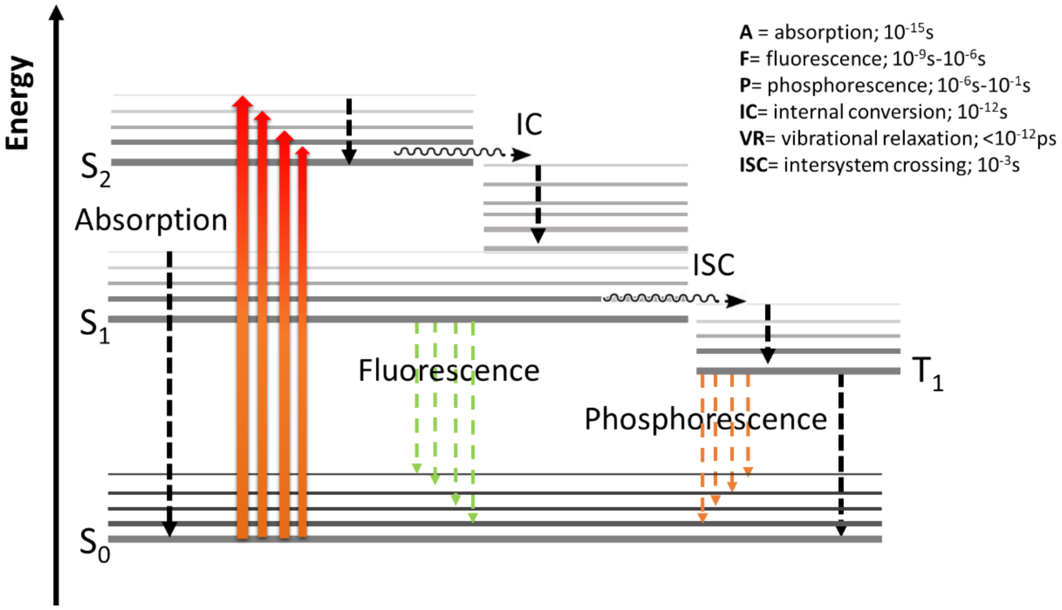

Figure 6. Jablonski diagram showing the associated transitions between the ground state S_0 and excited states (S_1, S_2, T_1) of a molecular complex, and their timescales (note that ISC rate is considerably higher in metal complexes due to high spin-orbit coupling).

Like the function of light-absorbing semiconductors in heterogeneous photocatalysis, molecular chromophores also called PS are used as an antenna for harvesting solar light, an example of this process is the pigments in plants like the chlorophyll in green plants or like carotenoids (Lutein) in vegetables. Those PS use energy captured from sunlight for photosynthesis and other photochemical processes (Figure 7).[104]

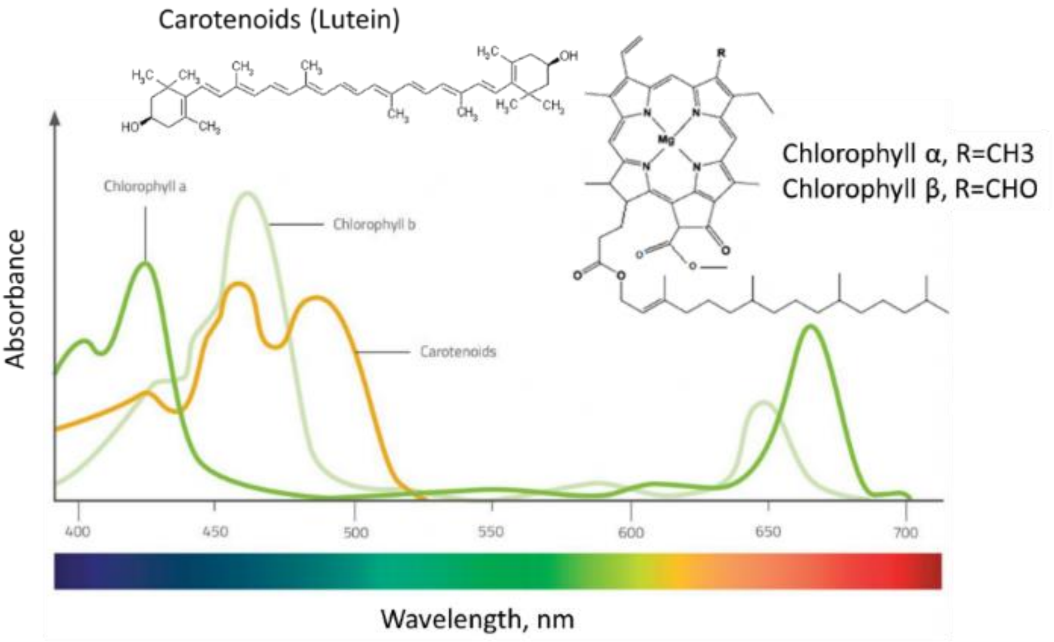

Figure 7. Molecular structure of different complexes used as light harvesters in nature like the carotenoids, Lutein, and the Chlorophyll-α and β and their corresponding UV Vis absorption spectra. Adapted from Ref.104 with permission.[104]

The use of PS is one of the most effective ways to extend the absorption of a semiconductor into the visible light range. A good photosensitiser should have a broad-band visible light absorption, suitable redox potentials, and a relatively long-lived excited state to use as much as possible from the solar radiation (Figure 8). [105]

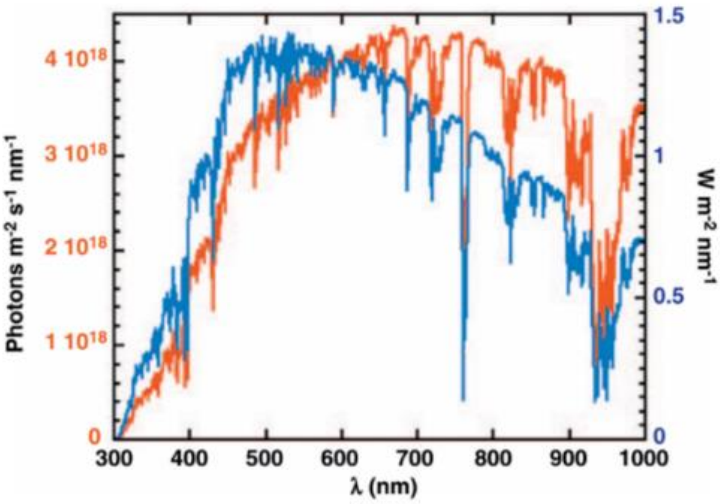

Figure 8. ASTM 1.5 solar output spectra. Standard reference solar spectrum used to evaluate solar cells and photosynthetic efficiency, which can be downloaded at http://rredc.nrel.gov/solar/spectra/am1.5/. Accessed in July 2021. The blue curve is the energy output spectrum, and the red curve is the photon flux spectrum. The photon flux spectrum is more relevant for a quantum energy storage process such as photosynthesis. Reproduced from 105 with permission.[105]

This approach is widely used in sensitized solar cells due to its capacity to enable the absorption in the visible and near infrared regions and accelerate the injection of the electron to the semiconductor: the high injection rate helps to reduce the negative effect of the competing recombination processes. The PS can be assembled onto the SC surface by linkers and anchoring groups, such as carboxylic or silane groups [106].

Transition-metal (TM) coordination compounds have been widely studied as photosensitisers for a few decades. One of the first complexes in this area, reported in 1978, was the $[Ru(bpy)_3]^{2+}$ (bpy = 2,2’-bypiridine) that was shown to act as a photocatalyst. A great diversity of other TM complexes followed, i.e. complexes of Ir(III), Ru(II), Re(I) or Pt(II) that have shown very good properties such as a high absorption of visible light and high redox potentials. Unfortunately, even when these

TM complexes are very efficient photosensitisers, they contain precious metals, and therefore incur high cost. Due to this, more recently a lot of research has been devoted to the development of low-cost metal complexes like Cu and Fe as photosensitisers or photocatalysts.[107–109]

1.8 Hydrogenases

Hydrogenases are in Nature a group of metalloenzymes which are capable to catalyse one of the simplest reactions: the conversion of dihydrogen into protons and electrons and the reverse reaction, for the generation of H_2 (Eq. 8).

$$\boldsymbol{H_2\ (\leftrightarrow H^+ + H^-) \leftrightarrow 2H^+ + 2e^-}$$ Eq. 8 Hydrogen evolution reaction.

In nature the hydrogenases are ubiquitous. They can be classified depending on the metal ion composition of their active sites, into [NiFe], [FeFe] and [Fe] types. Different types of hydrogenases can be found in bacteria, archaea and eukarya (Figure 9).

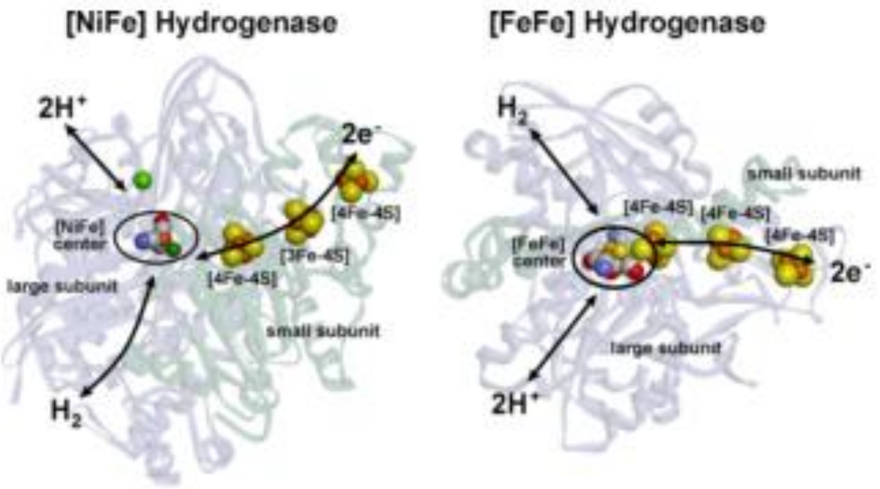

Figure 9. Structures of the natural [NiFe] hydrogenase from *Desulfovibrio vulgaris Miyazaki F* (DvMF) and of the [FeFe] hydrogenase from *Desulfovibrio desulfuricans (Dd)*. Reproduced from ref.[110]

Some of the [FeFe] hydrogenases are highly active for H_2 generation; each molecule can produce up to ~10^4 molecules of H_2 per second at room temperature. In contrast to [NiFe], the [FeFe] hydrogenases are generally more active to produce molecular hydrogen. Additionally, hydrogenases are known to have good stability (acting at elevated temperatures), are inexpensive, and work at low overpotentials.[110]

The structure of the [FeFe] hydrogenases present in *Clostridium pasteurianun* was identified by X-ray crystallography and published in 1998. Since then, a lot of attention has been attracted to study them for their application in photocatalytic processes and many other [FeFe] complexes hydrogenase mimics have been synthesized in the last few decades (Figure 10).[111]

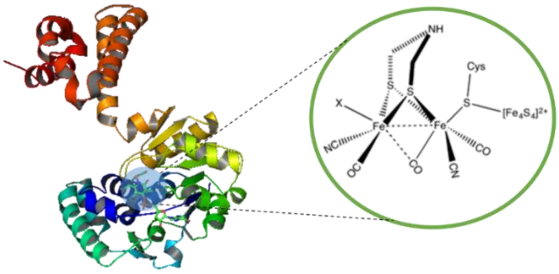

Figure 10. Crystal structure of [FeFe] hydrogenase active site from *Clostridium pasteurianun*. Reproduced from ref.[111]

This crystallographic analysis shows that [FeFe]-hydrogenases has an active centre formed by the Fe_2S_2 subunit coordinated by the cysteine-linked Fe_4S_4 cluster, carbon monoxide and the cyanide ligand and the two irons are bridged by a dithionate (Figure 11).

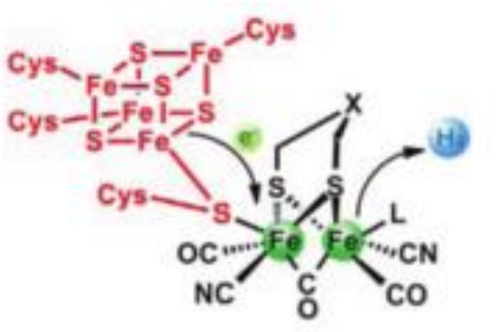

Figure 11. Active site of a Natural [FeFe] Hydrogenase X=CH_2 or NH. Reproduced from ref.[112]

In this structure, the Fe_2S_2 unit acts as the catalytic active site for the proton reduction, and the Fe_4S_4 cluster for the electron transfer to the active site.[112] The electron transfer is a prerequisite for hydrogen evolution.

In the Fe-Fe hydrogenases, the hydride is formed by the oxidative addition of a proton to the diiron site. The proton and electron transfer diagram shows all the possible protonation and electron transfer steps throughout a catalytic cycle (Figure 12). This cycle depends on the ligand set of the Fe_2 site.

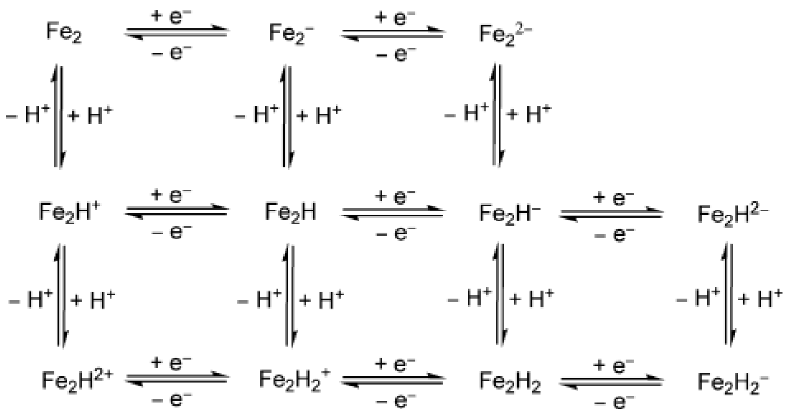

Figure 12. Scheme of the proton and electron transfer steps during hydrogen production, catalysed by FeFe hydrogenase active site model complexes. Reproduced from ref.[102]

The investigation of hydrogenases and the detailed understanding of their enzymatic reactions can provide a structural and functional basis for the chemical development of “artificial hydrogenases”, the future employment of tailor-made modified biological systems for hydrogen production, and the use of molecular hydrogen, e.g., in fuel cells.

Many different hydrogenases model compounds have been synthesized using a wide variety of ligands.[113]

The ligands affect electron density on the diiron centre, therefore affecting their properties. For example, the propyldithiolate (pdt) complexes are reduced irreversibly, while benzenedithiolate bridged (bdt) complexes typically feature a reversible reduction (Figure 13).[114]

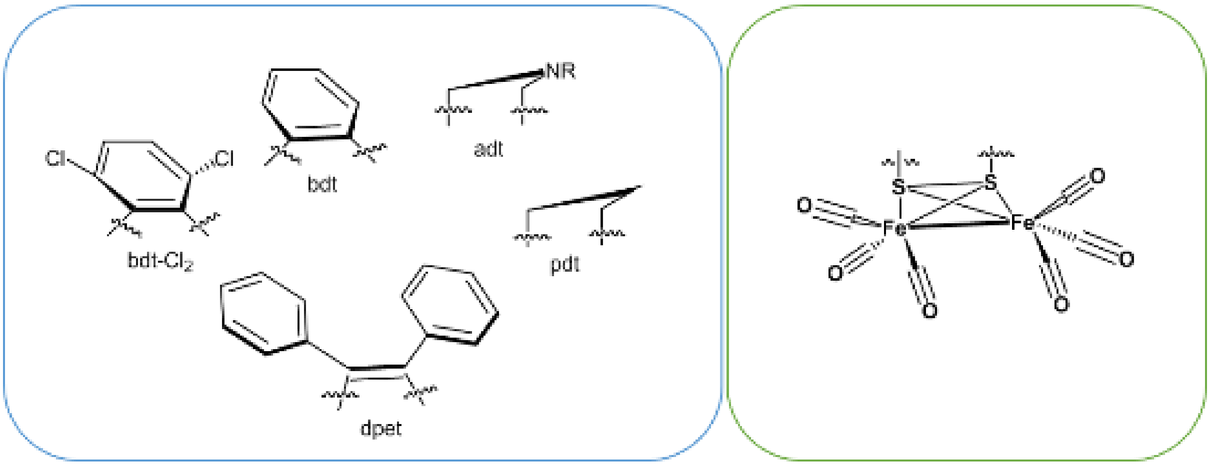

Figure 13. A selection of different [FeFe] hydrogenases model complexes and the different ligands studied.

1.9 Summary

According to the literature review presented, there has been a lot of efforts to develop an efficient hybrid artificial photocatalytic system using different photosensitizers and catalysts, some of them attached to semiconductor surfaces. Nevertheless, many questions on the functioning of these systems are still unanswered. Also, there is a wide range of different complexes that have not been well studied yet, such as aluminates as semiconductors, some new hydrogenase mimic complexes, and other photosensitizers based on Earth-abundant metals like copper. Additionally, there is a great opportunity to generate new knowledge using hybrid systems, where a photosensitizer and a hydrogenase mimic are linked to a semiconductor.

1.10 Research questions, aims and specific objectives.

Despite all the advances in the development of new systems for hydrogen evolution from water using different hydrogenases with different photosensitizers and semiconductors, there remains a lot of opportunities and questions to be answered to create new and more efficient systems for hydrogen evolution through water splitting via PEC and understand better their mechanism.

This work aims to link together a highly efficient visible light-absorbing copper complex as photosensitiser to a semiconductor surface, using a [FeFe] hydrogenase mimic complex as a catalyst for hydrogen production from water splitting via PEC (Figure 14).

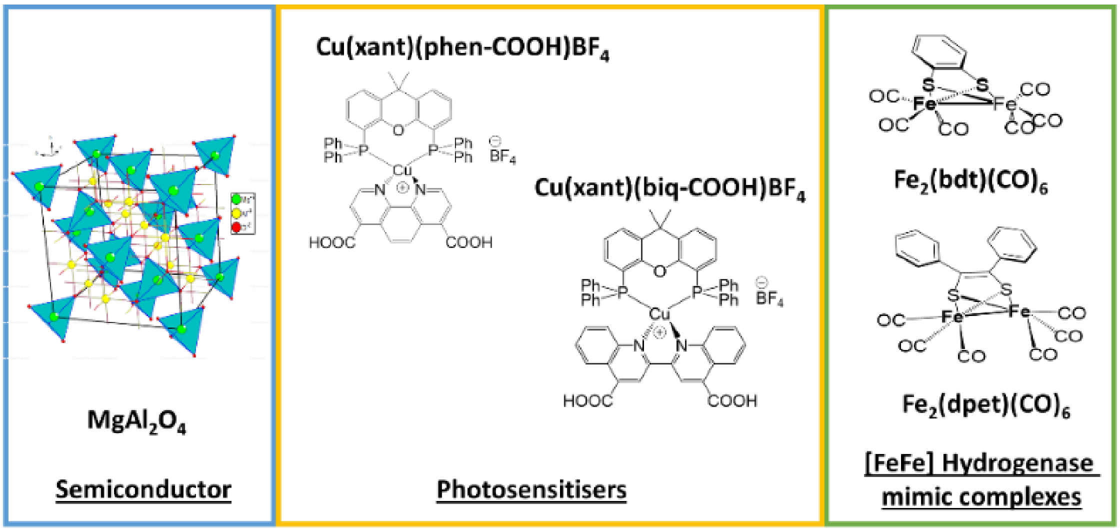

Figure 14. Molecular structures of the semiconductor $MgAl_2O_4$; the [FeFe] hydrogenase mimic complexes used as catalysts $Fe_2(dpet)(CO)_6$ and $Fe_2(bdt)(CO)_6$ used for comparison; and the Cu complexes $Cu(xantphos)(phen\text{-}COOH)BF_4$ and $Cu(xantphos)(biq\text{-}COOH)BF_4$ used as photosensitizers in this research project.

Questions to be answered in this research:

Chapter 3- What is the effect of the ligand of the newly synthesized [FeFe] complex on the photophysical and electrochemical properties and their performance as catalyst for proton reduction?

Chapter 4- Will the use of Ni and Cu as dopants in the $MgAl_2O_4$ semiconductors modify their photophysical properties? How will this affect the position of the energy bands, and therefore their performance for water splitting?

Chapter 5- What are the stability, electrochemical and photophysical properties of the new Cu complexes?

Chapter 6- What is the electron transfer mechanism between the Cu complexes and the SC when those are assembled on the surface of the SC? How are they assembled on the surface? What are the effects of the synthesis and different methods used for the preparation of the films and what impact will this have on their performance as photoanodes for PEC water splitting? And how does the electron transfer mechanism work in the hybrid system “Semiconductor – Photosensitiser – Hydrogenase”? Is this system a viable solution for H_2 PEC evolution?

The **specific objectives** of this project include:

The synthesis of the semiconductors $MgAl_2O_4$ modified by doping with Ni and Cu in 0.1, 1 and 10% wt. in ratio with the metal cation to improve their photocatalytic performance.

The synthesis and characterization of the new [FeFe] hydrogenase mimic complex $Fe_2(dpet)(CO)_6$ and $Fe_2(bdt)(CO_6)$ as comparison.

Investigation of the photophysical and electrochemical properties of the FeFe complex $Fe_2(dpet)(CO)_6$ for its application in water splitting.

Development of a synthetic approach to covalently link the PS to the SC surface.

Systematically vary the light-absorbing properties of the PS, to evaluate the performance of the PS at different excitation energies and their limits to avoid the photo-corrosion processes.

Investigate the photophysical and electrochemical properties of the hybrid photocatalytic systems. The absorption properties of each component of the system will be evaluated. The photophysical characterization includes emission properties of the photosensitiser, and the rates of electron transfer obtained from quenching experiments. These will be obtained by emission spectroscopy, and time-resolved laser spectroscopy.

For the electrochemical characterization, cyclic voltammetry will be used to obtain the redox potentials of the different materials, chronoamperometry will be performed for the photo corrosion tests, and electrochemical impedance spectroscopy analysis will be done to know the position of the valence band and the conduction band (HOMO and LUMO).

The efficiency of the H_2 evolution will be evaluated by conventional gas chromatography. All the above will be performed on a variety of PS-linker-Catalyst systems to evaluate the influence of the systematic variation in the reductive ability of the photosensitizer; The electronic coupling between the components will be adjusted by varying the structure of the linker and the efficiency of various sacrificial electron donors which traditionally are organic amines. Thus, the overall performance, photostability and efficiency, will be optimized.

1.11 References

1. UNESCO 2017. *Education for Sustainable Development Goals - Learning Objectives*. (2017).
2. World Health Organization. *COVID-19 weekly epidemiological update*. *World Health Organization* https://www.who.int/publications/m/item/covid-19-weekly-epidemiological-update (2021).
3. International Energy Agency. *Global Energy Review 2020*. *Global Energy Review 2020* (OECD, 2020). doi:10.1787/a60abbf2-en.
4. International Energy Agency. Net Zero by 2050: A Roadmap for the Global Energy Sector. *Int. Energy Agency* 224 (2021).
5. International Energy Agency. *Global Energy & CO2 Status Report*. (2018).
6. Henner, D. & REN21. *Renewables 2021: Global Status Report*. (2021).
7. Van De Krol, R. & Grätzel, M. *Photoelectrochemical Hydrogen Production*. *Springer* vol. 1 (2012).
8. Dawood, F., Anda, M. & Shafiullah, G. M. Hydrogen production for energy: An overview. *Int. J. Hydrogen Energy* **45**, 3847–3869 (2020).
9. El-Shafie, M., Kambara, S. & Hayakawa, Y. Hydrogen Production Technologies Overview. *J. Power Energy Eng.* **07**, 107–154 (2019).
10. Miao, B. & Chan, S. H. The economic feasibility study of a 100-MW Power-to-Gas plant. *Int. J. Hydrogen Energy* **44**, 20978–20986 (2019).
11. Gillespie, M. I., Van Der Merwe, F. & Kriek, R. J. Performance evaluation of a membraneless divergent electrode-flow-through (DEFT) alkaline electrolyser based on optimisation of electrolytic flow and electrode gap. *J. Power Sources* **293**, 228–235 (2015).
12. El-Emam, R. S. & Özcan, H. Comprehensive review on the techno-economics of sustainable large-scale clean hydrogen production. *J. Clean. Prod.* **220**, 593–609 (2019).
13. Esposito, D. V. Membraneless Electrolyzers for Low-Cost Hydrogen Production in a Renewable Energy Future. *Joule* **1**, 651–658 (2017).

14. Araya, S. S. *et al.* A review of the methanol economy: The fuel cell route. *Energies* **13**, (2020).

15. Wang, Y., Leung, D. Y. C., Xuan, J. & Wang, H. A review on unitized regenerative fuel cell technologies, part-A: Unitized regenerative proton exchange membrane fuel cells. *Renew. Sustain. Energy Rev.* **65**, 961–977 (2016).

16. Robinius, M. *et al. Comparative Analysis of Infrastructures: Hydrogen Fueling and Electric Charging of Vehicles*. *Schriften des Forschungszentrums Jülich* vol. 408 (2018).

17. Davis, J. T., Qi, J., Fan, X., Bui, J. C. & Esposito, D. V. Floating membraneless PV-electrolyzer based on buoyancy-driven product separation. *Int. J. Hydrogen Energy* **43**, 1224–1238 (2018).

18. Das, D. *Microbial fuel cell: A bioelectrochemical system that converts waste to watts*. *Microbial Fuel Cell: A Bioelectrochemical System that Converts Waste to Watts* (2017). doi:10.1007/978-3-319-66793-5.

19. Maljusch, A. & Wullenkord, M. Techno-Economic Analysis of PEC Water Splitting at Various Scales. *RSC Energy Environ. Ser.* 266–284 (2018) doi:10.1039/9781782629863-00266.

20. Wijffels, R. H., Barten, H. & Reith, R. H. *Bio_methane & Bio-hydrogen*. (2003).

21. Acar, C. & Dincer, I. Investigation of a novel photoelectrochemical hydrogen production system. *Chem. Eng. Sci.* **197**, 74–86 (2019).

22. Arifin, K., Majlan, E. H., Wan Daud, W. R. & Kassim, M. B. Bimetallic complexes in artificial photosynthesis for hydrogen production: A review. *Int. J. Hydrogen Energy* **37**, 3066–3087 (2012).

23. Zeng, K. & Zhang, D. Recent progress in alkaline water electrolysis for hydrogen production and applications. *Prog. Energy Combust. Sci.* **36**, 307–326 (2010).

24. Alanne, K. & Cao, S. An overview of the concept and technology of ubiquitous energy. *Appl. Energy* **238**, 284–302 (2019).

25. Ahmed, L. M., Alkaim, A. F., Halbus, A. F. & Hussein, F. H. Photocatalytic hydrogen production from aqueous methanol solution over metallized Tio2. *Int.*

J. ChemTech Res. **9**, 90–98 (2016).

26. Abdalla, A. M. *et al.* Hydrogen production, storage, transportation and key challenges with applications: A review. *Energy Convers. Manag.* **165**, 602–627 (2018).

27. Baykara, S. Z. Hydrogen: A brief overview on its sources, production and environmental impact. *Int. J. Hydrogen Energy* **43**, 10605–10614 (2018).

28. Shukla, M. & Kumar, S. Algal growth in photosynthetic algal microbial fuel cell and its subsequent utilization for biofuels. *Renew. Sustain. Energy Rev.* **82**, 402–414 (2018).

29. Khetkorn, W. *et al.* Microalgal hydrogen production – A review. *Bioresour. Technol.* **243**, 1194–1206 (2017).

30. Kosourov, S., Murukesan, G., Seibert, M. & Allahverdiyeva, Y. Evaluation of light energy to H2 energy conversion efficiency in thin films of cyanobacteria and green alga under photoautotrophic conditions. *Algal Res.* **28**, 253–263 (2017).

31. Eroglu, E. & Melis, A. Microalgal hydrogen production research. *Int. J. Hydrogen Energy* **41**, 12772–12798 (2016).

32. Nikolaidis, P. & Poullikkas, A. A comparative overview of hydrogen production processes. *Renew. Sustain. Energy Rev.* **67**, 597–611 (2017).

33. El-Khouly, M. E., El-Mohsnawy, E. & Fukuzumi, S. Solar energy conversion: From natural to artificial photosynthesis. *J. Photochem. Photobiol. C Photochem. Rev.* **31**, 36–83 (2017).

34. Mah, A. X. Y. *et al.* Review of hydrogen economy in Malaysia and its way forward. *Int. J. Hydrogen Energy* **44**, 5661–5675 (2019).

35. Yang, J., Cui, Z., Ma, J. & Dong, Z. Ru coated Co nanoparticles decorated on cotton derived carbon fibers as a highly efficient and magnetically recyclable catalyst for hydrogen generation from ammonia borane. *Int. J. Hydrogen Energy* **43**, 1355–1364 (2018).

36. Zhao, N. *et al.* Electricity generation and microbial communities in microbial fuel cell powered by macroalgal biomass. *Bioelectrochemistry* **123**, 145–149 (2018).

37. Badran, A., Murad, S., Baydoun, E. & Daghir, N. *Water, energy & food*

sustainability in the middle eaBadran, A., Murad, S., Baydoun, E., & Daghir, N. (2017). Water, energy & food sustainability in the middle east: The sustainability triangle. In Water, Energy and Food Sustainability in the Middle East: . Water, Energy and Food Sustainability in the Middle East: The Sustainability Triangle (2017).

38. Zhao, Y., Cimpoia, R., Liu, Z. & Guiot, S. R. Orthogonal optimization of Carboxydothermus hydrogenoformans culture medium for hydrogen production from carbon monoxide by biological water-gas shift reaction. *Int. J. Hydrogen Energy* **36**, 10655–10665 (2011).

39. Bayrakci, A. G. & Koçar, G. Utilization of renewable energies in Turkey's agriculture. *Renew. Sustain. Energy Rev.* **16**, 618–633 (2012).

40. Lin, R., Cheng, J. & Murphy, J. D. Unexpectedly low biohydrogen yields in co-fermentation of acid pretreated cassava residue and swine manure. *Energy Convers. Manag.* **151**, 553–561 (2017).

41. Lin, R., Cheng, J. & Murphy, J. D. Inhibition of thermochemical treatment on biological hydrogen and methane co-production from algae-derived glucose/glycine. *Energy Convers. Manag.* **158**, 201–209 (2018).

42. Dincer, I. Green methods for hydrogen production. *Int. J. Hydrogen Energy* **37**, 1954–1971 (2012).

43. Luo, M. *et al.* Review of hydrogen production using chemical-looping technology. *Renew. Sustain. Energy Rev.* **81**, 3186–3214 (2018).

44. Bernardo, G., Araújo, T., da Silva Lopes, T., Sousa, J. & Mendes, A. Recent advances in membrane technologies for hydrogen purification. *Int. J. Hydrogen Energy* **45**, 7313–7338 (2020).

45. Shirasaki, Y. & Yasuda, I. *Membrane reactor for hydrogen production from natural gas at the Tokyo Gas Company: A case study*. *Handbook of Membrane Reactors* vol. 2 (Woodhead Publishing Limited, 2013).

46. Drioli, E., Brunetti, A., Di Profio, G. & Barbieri, G. Process intensification strategies and membrane engineering. *Green Chem.* **14**, 1561–1572 (2012).

47. Simmons, T. R., Berggren, G., Bacchi, M., Fontecave, M. & Artero, V. Mimicking hydrogenases: From biomimetics to artificial enzymes. *Coord. Chem. Rev.* **270**–

271, 127–150 (2014).

48. Goldbach, A. *et al.* Evaluation of Pd composite membrane for pre-combustion CO2 capture. *Int. J. Greenh. Gas Control* **33**, 69–76 (2015).

49. Lu, N. & Xie, D. Novel Membrane Reactor Concepts for Hydrogen Production from Hydrocarbons: A Review. *Int. J. Chem. React. Eng.* **14**, 1–31 (2016).

50. Meng, L. & Tsuru, T. Microporous membrane reactors for hydrogen production. *Curr. Opin. Chem. Eng.* **8**, 83–88 (2015).

51. Jang, W. J., Shim, J. O., Kim, H. M., Yoo, S. Y. & Roh, H. S. A review on dry reforming of methane in aspect of catalytic properties. *Catal. Today* **324**, 15–26 (2019).

52. Wang, Y. J. *et al.* Recent advancements in the development of bifunctional electrocatalysts for oxygen electrodes in unitized regenerative fuel cells (URFCs). *Prog. Mater. Sci.* **98**, 108–167 (2018).

53. Saba, S. M., Müller, M., Robinius, M. & Stolten, D. The investment costs of electrolysis – A comparison of cost studies from the past 30 years. *Int. J. Hydrogen Energy* **43**, 1209–1223 (2018).

54. Lai, J., Nsabimana, A., Luque, R. & Xu, G. 3D Porous Carbonaceous Electrodes for Electrocatalytic Applications. *Joule* **2**, 76–93 (2018).

55. Jepsen, L. H. *et al.* Boron-nitrogen based hydrides and reactive composites for hydrogen storage. *Mater. Today* **17**, 129–135 (2014).

56. Dinh, L. N. *et al.* Kinetic measurement and prediction of the hydrogen outgassing from the polycrystalline LiH/Li2O/LiOH system. Journal of Nuclear Materials **347**, 31-43 (2006).

57. G. K. Pitcher. Solid lithium hydride as a hydrogen source for fuel cells. *Proc. Symp. Auton. Underw. Veh. Technol.* 455–460 (1996).

58. Hui, W., Xiaoqiong, F., Xiaofang, W., Sanping, C. & Shengli, G. Hydrogen production by redox of bimetal cation-modified iron oxide. *Int. J. Hydrogen Energy* **33**, 7122–7128 (2008).

59. Ozbilen, A., Dincer, I. & Rosen, M. A. A comparative life cycle analysis of hydrogen production via thermochemical water splitting using a Cu-Cl cycle. *Int.*

J. Hydrogen Energy **36**, 11321–11327 (2011).

60. Esswein, A. J. & Nocera, D. G. Hydrogen production by molecular photocatalysis. *Chem. Rev.* **107**, 4022–4047 (2007).

61. Sullivan, K. K. *et al.* Low-energy (<20 eV) and high-energy (1000 eV) electron-induced methanol radiolysis of astrochemical interest. *Mon. Not. R. Astron. Soc.* **460**, 664–672 (2016).

62. Iwamatsu, K., Sundin, S. & LaVerne, J. A. Hydrogen peroxide kinetics in water radiolysis. *Radiat. Phys. Chem.* **145**, 207–212 (2018).

63. Sterniczuk, M. & Bartels, D. M. Source of Molecular Hydrogen in High-Temperature Water Radiolysis. *J. Phys. Chem. A* **120**, 200–209 (2016).

64. Faunce, T. A. *et al.* Energy and environment policy case for a global project on artificial photosynthesis. *Energy Environ. Sci.* **6**, 695–698 (2013).

65. Fujishima, A. & Honda, K. Electrochemical photolysis of water at a semiconductor electrode. *Nature* **238**, 37–38 (1972).

66. Verne, J. *The Mysterious Island*. (Pierre-Jules Hetzel Publisher, 1874).

67. Darwin, C. *The Origin of Species*. (1859).

68. Lubitz, W., Reijerse, E. J. & Messinger, J. Solar water-splitting into H2 and O2: Design principles of photosystem II and hydrogenases. *Energy Environ. Sci.* **1**, 15–31 (2008).

69. Liu, J. W., Chen, G., Li, Z. H. & Zhang, Z. G. Hydrothermal synthesis and photocatalytic properties of ATaO3 and ANbO3 (A = Na and K). *Int. J. Hydrogen Energy* **32**, 2269–2272 (2007).

70. Li, Y., Li, S., Li, Y., Guo, Y. & Wang, J. Visible-light driven photocatalyst (Er3+:YAlO3/Pt-NaTaO3) for hydrogen production from water splitting. *Int. J. Hydrogen Energy* **39**, 17608–17616 (2014).

71. Ikeda, T., Fujiyoshi, S., Kato, H., Kudo, A. & Onishi, H. Time-resolved infrared spectroscopy of K3Ta3B2O12 photocatalysts for water splitting. *J. Phys. Chem. B* **110**, 7883–6 (2006).

72. Miseki, Y., Kato, H. & Kudo, A. Water splitting into H2 and O2 over niobate and titanate photocatalysts with (111) plane-type layered perovskite structure.

Energy Environ. Sci. **2**, 306 (2009).

73. Gómez-Solís, C., Ruiz-Gómez, M. A., Torres-Martínez, L. M., Juárez-Ramírez, I. & Sánchez-Martínez, D. Facile solvo-combustion synthesis of crystalline NaTaO3 and its photocatalytic performance for hydrogen production. *Fuel* **130**, 221–227 (2014).

74. Agbe, H. *et al.* Recent advances in photoinduced catalysis for water splitting and environmental applications. *J. Ind. Eng. Chem.* **72**, 31–49 (2019).

75. Tian, H. *et al.* Fabrication of an efficient noble metal-free TiO2-based photocatalytic system using Cu-Ni bimetallic deposit as an active center of H2 evolution from water. *Sol. Energy Mater. Sol. Cells* **134**, 309–317 (2015).

76. Hashimoto, K., Irie, H. & Fujishima, A. TiO 2 photocatalysis: A historical overview and future prospects. *Japanese J. Appl. Physics, Part 1 Regul. Pap. Short Notes Rev. Pap.* **44**, 8269–8285 (2005).

77. Stoll, T. *et al.* Visible-light-promoted gas-phase water splitting using porous WO3/BiVO4 photoanodes. *Electrochem. commun.* **82**, 47–51 (2017).

78. Sivula, K. Chapter 6: Emerging Semiconductor Oxides for Direct Solar Water Splitting. *RSC Energy Environ. Ser.* **2018**, 163–182 (2018).

79. Francàs, L., Mesa, C. A., Pastor, E., Le Formal, F. & Durrant, J. R. *Chapter 5: Rate Law Analysis of Water Splitting Photoelectrodes*. *RSC Energy and Environment Series* vols 2018-Janua (2018).

80. Regmi, C. *et al.* Understanding the multifunctionality in Cu-doped BiVO4 semiconductor photocatalyst. *J. Environ. Sci. (China)* **75**, 84–97 (2019).

81. Khan, Z. *et al.* Visible light assisted photocatalytic hydrogen generation and organic dye degradation by CdS-metal oxide hybrids in presence of graphene oxide. *RSC Adv.* **2**, 12122–12128 (2012).

82. Hisatomi, T., Kubota, J. & Domen, K. Recent advances in semiconductors for photocatalytic and photoelectrochemical water splitting. *Chem. Soc. Rev.* **43**, 7520–7535 (2014).

83. Agbe, H. *et al.* Recent advances in photoinduced catalysis for water splitting and environmental applications. *J. Ind. Eng. Chem.* **72**, 31–49 (2019).

84. Carrasco-Jaim, O. A., Torres-Martínez, L. M. & Moctezuma, E. Enhanced photocatalytic hydrogen production of AgMO3 (M = Ta, Nb, V) perovskite materials using CdS and NiO as co-catalysts. *J. Photochem. Photobiol. A Chem.* **358**, 167–176 (2018).

85. Guigoz, V., Bruyère, S., Migot, S., Schneider, R. & Gries, T. Enhanced photoelectrocatalytic hydrogen evolution using off-stoichiometry La0.43FeOy films. *J. Alloys Compd.* **893**, 162238 (2022).

86. Park, H., Choi, W. & Hoffmann, M. R. Effects of the preparation method of the ternary CdS/TiO2/Pt hybrid photocatalysts on visible light-induced hydrogen production. *J. Mater. Chem.* **18**, 2379 (2008).

87. Khan, Z. *et al.* Visible light assisted photocatalytic hydrogen generation and organic dye degradation by CdS-metal oxide hybrids in presence of graphene oxide. *RSC Adv.* **2**, 12122–12128 (2012).

88. Ding, L. *et al.* Butterfly wing architecture assisted CdS/Au/TiO2 Z-scheme type photocatalytic water splitting. *Int. J. Hydrogen Energy* **38**, 8244–8253 (2013).

89. Li, Y. *et al.* Improved photoelectrochemical property of a nanocomposite NiO/CdS@ZnO photoanode for water splitting. *Sol. Energy Mater. Sol. Cells* **132**, 40–46 (2015).

90. Zhu, Z. *et al.* Porous “brick-like” NiFe2O4 nanocrystals loaded with Ag species towards effective degradation of toluene. *Chem. Eng. J.* **165**, 64–70 (2010).

91. Tianyou Peng, Xiaohu Zhang, Hongjin Lv, L. Z. Preparation of NiFe2O4 nanoparticles and its visible-light-driven photoactivity for hydrogen production. *Catal. Commun.* **28**, 116–119 (2012).

92. Nassar, M. Y., Ahmed, I. S. & Samir, I. A novel synthetic route for magnesium aluminate (MgAl2O4) nanoparticles using sol-gel auto combustion method and their photocatalytic properties. *Spectrochim. Acta. A. Mol. Biomol. Spectrosc.* **131**, 329–34 (2014).

93. Gómez-solís, C., Peralta-arriaga, S. L., Torres-martínez, L. M., Juárez-ramírez, I. & Díaz-torres, L. A. Photocatalytic activity of MAl 2 O 4 (M = Mg , Sr and Ba) for hydrogen production. **188**, 197–204 (2017).

94. Li, L. *et al.* Visible light driven hydrogen production from a photo-active cathode

based on a molecular catalyst and organic dye-sensitized p-type nanostructured NiO. *Chem. Commun.* **48**, 988–990 (2012).

95. Youngblood, W. J. *et al.* Photoassisted Overall Water Splitting in a Visible Light-Absorbing Dye Sensitized Photoelectrochemical Cell. 1–13 (2009).

96. Li, X. *et al.* Noncovalent Assembly of a Metalloporphyrin and an Iron Hydrogenase Active-Site Model : Photo-Induced Electron Transfer and Hydrogen Generation Noncovalent Assembly of a Metalloporphyrin and an Iron Hydrogenase Active-Site Model : Photo-Induced Electron Tr. *Society* 8198–8202 (2008) doi:10.1021/jp710498v.

97. Gueret, R. *et al.* Challenging the [Ru(bpy)3]2+ Photosensitizer with a Triazatriangulenium Robust Organic Dye for Visible-Light-Driven Hydrogen Production in Water. *ACS Catal.* **8**, 3792–3802 (2018).

98. Lv, H. *et al.* Semiconductor quantum dot-sensitized rainbow photocathode for effective photoelectrochemical hydrogen generation. *Proc. Natl. Acad. Sci. U. S. A.* **114**, 11297–11302 (2017).

99. Zhang, X., Peng, T. & Song, S. Recent advances in dye-sensitized semiconductor systems for photocatalytic hydrogen production. *J. Mater. Chem. A* **4**, 2365–2402 (2016).

100. Wen, M. *et al.* Integrating CdSe Quantum Dots with a [FeFe]-Hydrogenase Mimic into a Photocathode for Hydrogen Evolution at a Low Bias Voltage. *ChemPhotoChem* **1**, 260–264 (2017).

101. Reisner, E., Fontecilla-Camps, J. C. & Armstrong, F. A. Catalytic electrochemistry of a [NiFeSe]-hydrogenase on TiO2and demonstration of its suitability for visible-light driven H2production. *Chem. Commun.* 550–552 (2009) doi:10.1039/b817371k.

102. Lomoth, R. & Ott, S. Introducing a dark reaction to photochemistry: Photocatalytic hydrogen from [FeFe] hydrogenase active site model complexes. *Dalt. Trans.* 9952–9959 (2009) doi:10.1039/b911129h.

103. Dieter Rehm, A. W. Kinetics of fluorescence quenching by electron and H-Atom transfer. *Isr. J. Chem.* **8**, 259–271 (1970).

104. Guidi, L., Tattini, M. & Landi, M. How Does Chloroplast Protect Chlorophyll

Against Excessive Light? *Chlorophyll* (2017).

105. Chen, M. & Blankenship, R. E. Expanding the solar spectrum used by photosynthesis. *Trends Plant Sci.* **16**, 427–431 (2011).

106. O'Regan, B. & G. M. A low-cost, high-efficiency solar cell based on dye-sensitized colloidal Ti02 films Brian. *Nature* **353**, 737–739 (1991).

107. Lennox, A. J. J., Fischer, S., Jurrat, M., Luo, S. & Rockstroh, N. Photosensitisers in Water Reduction : A More Efficient in Situ Formed System and Improved Mechanistic Understanding . Chemistry - A This document is made available in accordance with publisher policies . Please cite only the Copper-Based Photosensitizers . **22**, 1233–1238 (2016).

108. Lennox, A. J. J. *et al.* Copper-Based Photosensitisers in Water Reduction: A More Efficient in Situ Formed System and Improved Mechanistic Understanding. *Chem. - A Eur. J.* **22**, 1233–1238 (2016).

109. Behm, K. & McIntosh, R. D. Application of Discrete First-Row Transition-Metal Complexes as Photosensitisers. *ChemPlusChem* vol. 85 2611–2618 (2020).

110. Lubitz, W., Ogata, H., Rüdiger, O. & Reijerse, E. Hydrogenases. *Chem. Rev.* **114**, 4081–4148 (2014).

111. Peters, J. W. X-ray Crystal Structure of the Fe-Only Hydrogenase (CpI) from Clostridium pasteurianum to 1.8 Angstrom Resolution. *Science (80-.).* **282**, 1853–1858 (1998).

112. Wang, F. *et al.* Artificial photosynthetic systems based on [FeFe]-hydrogenase mimics: The road to high efficiency for light-driven hydrogen evolution. *ACS Catal.* **2**, 407–416 (2012).

113. Tard, C. & Pickett, C. J. Structural and functional analogues of the active sites of the [Fe]-, [NiFe]-, and [FeFe]-hydrogenases. *Chem. Rev.* **109**, 2245–2274 (2009).

114. Streich, D. *et al.* Comparing the reactivity of benzenedithiolate- versus alkyldithiolate- bridged Fe2(CO)6 complexes with competing ligands. *Eur. J. Inorg. Chem.* **2**, 1106–1111 (2011).

Chapter 2

Fundamentals and Techniques

This chapter contains all the fundamentals and techniques used for this Thesis.

2.1 List of Figures

2.2 Fundamentals and Techniques

Photosynthesis is one of the processes essential for life. Its fundamental basis is in photochemistry, an area of chemistry that studies the chemical effects of light. Like every other photochemical process, it starts with the absorption of energy by a molecule in the form of a photon of light. The energy of the photon is used to promote the molecule into a higher energy, photoexcited state, and is usually accompanied by a redistribution of electron density in the molecule. Since energy levels in the matter are quantized, a transition between two electronic states must also be associated with specific amount of energy. Thus, a direct result of the quantization of the energy levels is that only specific energies of radiation can be absorbed (or emitted) by the molecule.[1–3]

2.3 Absorption

As we have already established, all photochemical reactions start with the absorption of light (photochemical activation). Light absorption follows three laws: (i) the Grothuss-Draper law which states that a molecule must absorb light for a photochemical reaction to take place; (ii) the Stark-Einstein law which states that for each photon of light absorbed by a molecule, only one molecule is activated for a subsequent reaction; and (iii) Kasha's rule that states that the emissive energy level of a given multiplicity is normally the lowest energy excited state of that multiplicity.

The energy gained by a molecule when it absorbs a UV or visible photon, promotes an electron to a higher energy level generating an excited state. This absorption process is governed by the Beer-Lambert law(Eq. 1) where the absorbance is given by the difference in the incident light intensity (I_0) and the transmitted light intensity (I).

This is equal to the extinction coefficient (σ) multiplied by the sample concentration (c) and the path length (l).

$$A = -ln\left(\frac{I}{I_0}\right) = \sigma_v cl \qquad \text{Eq. 1}$$

After the absorption of the light, the formation of an excited state occurs. In the orbital approximation, this process is represented by the transition of an electron from one of the filled orbitals to one that is partially or fully empty. The energy of the transition is equal, in this approximation, to the difference in energy between those two orbitals, and the photon of light should have frequency (ν) given by:

$$hv = E_{final} - E_{initial} \qquad \text{Eq. 2}$$

where *h* is the Planck's constant, and E_{final} and E_{initial} are the energies of the vacant (receiving) and the occupied (donating) orbitals, respectively.

Since these transitions can happen between any pair of a filled and an empty orbitals, a molecule can exist in any of multiple excited states, each populated by absorption of a photon of specific frequency (Eq. 2).[1]

In the Born-Oppenheimer approximation, the motion of nuclei and electrons is separable because of the different timescales of their motions. An application of the Born-Oppenheimer approximation to absorption of light results in the Frank-Condon principle, which states that in the coordinates energy/"internuclear distance", the electronic transitions must be vertical. Therefore, no changes in the nuclear geometry can happen during an electronic transition. In general, the excited state is characterised by somewhat longer interatomic distances than the ground state. Therefore, upon absorption of a photon and the shift of the electron density, the molecule will have a non-favourable nuclear geometry for this new electron density distribution; this leads to the population of the vibrationally excited electronic state. The vibrationally excited (“hot”) electronic state will relax until its ν=0 level is reached, as the most stable molecular geometry is achieved. This process is known as vibrational cooling (VC), and in some cases, no vibrational cooling is observed because sometimes the electron density distribution is very similar in both electronic states, and this makes it suitable to promote an electron to the lowest vibrational level of the electronic state without any vibrational cooling effect (Figure 1).[4]

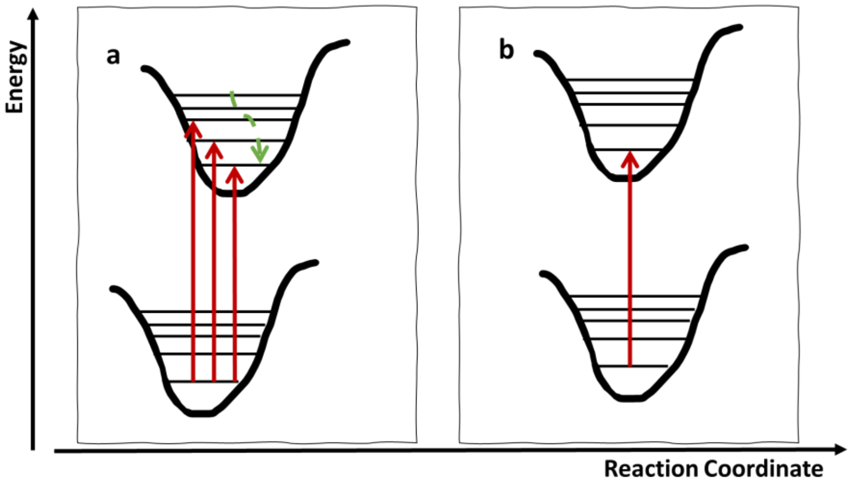

Figure 1. Diagram of both types of vertical vibrational transitions ruled by Frank-Condon principle. a) shows a change in equilibrium distance (x>0) and a VC process, and b) shown an equilibrium (x=0) where no VC is observed.

2.4 Photophysical processes and the excited states

A photochemical reaction is a chemical reaction that starts with the absorption of energy in the form of photons forming an excited state, this process usually occurs at timescales within 10 $^{-16}$ to 10^{-15} s. These excited states can be deactivated by different photophysical processes, and these can be radiative decay, non-radiative decay, and photochemical reactions.

Radiative decay normally occurs when an excited state emits a photon. This decay type can be classified into fluorescence and phosphorescence. In fluorescence emission, both initial and final states have same spin multiplicity (e.g., $S_1 \rightarrow S_0$), a spin-allowed transition with timescales that normally are in the range from 10^{-10} to 10^{-8} s.

Phosporescence is the type of emission where initial and final states have different spin multiplicities (e.g., $T_1 \rightarrow S_0$), this is a spin-forbidden transition. Phosporescence is slower than fluorescence, normally with lifetimes in the range of milliseconds to seconds.

Non-radiative decays can happen through different processes such as: internal conversion (IC), and intersystem crossing (ISC). All these processes have different timescales, all slower than the absorption process. An example of a light-driven ultrafast reaction are the initial steps of photosynthesis.

Figure 2 shows the Jablonski diagram of the principal photophysical radiative and non-radiative processes. There, the symbols S0, S1, S2 and T1 refer to the ground electronic singlet state (S0), first singlet excited state (S1), second singlet excited state (S2), and triplet excited state (T1). Also shown in the diagram, are the fluorescence and phosphorescence processes, that according to Kasha’s rule happen from the lowest energy single state (S1), and the lowest energy triplet state (T1), respectively.

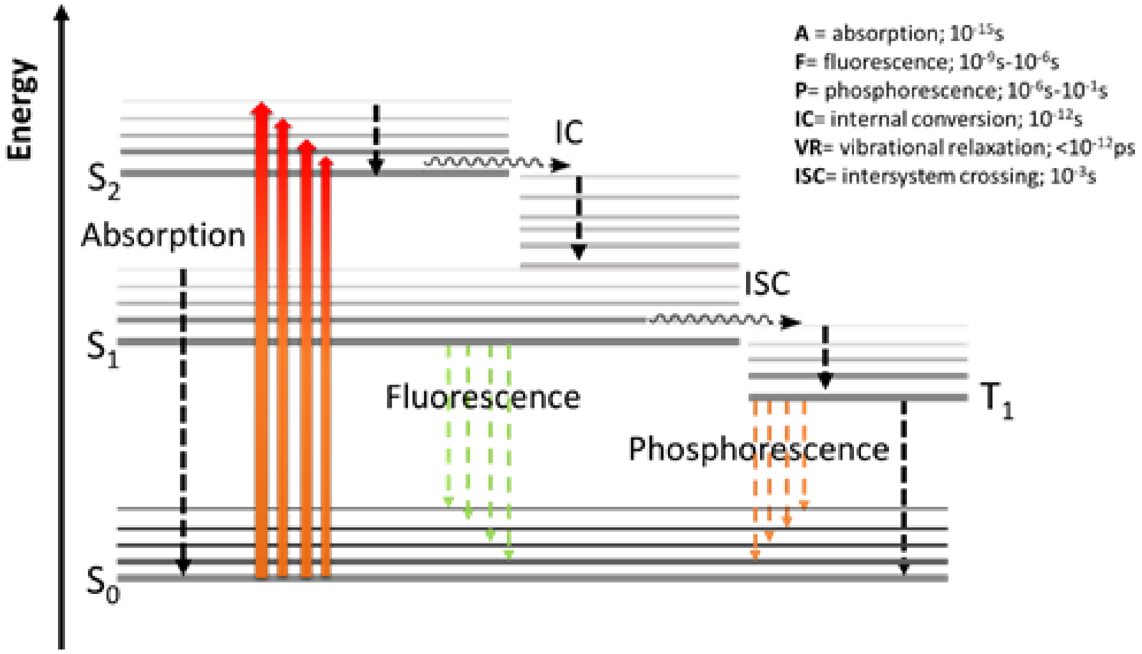

Figure 2. Jablonski diagram representing the different excited states processes after absorption of a photon and the deactivation processes of the excited states. Processes involving absorption or emission of a photon (coloured arrows). Transitions between different excited states (Horizontal black arrows) and vibrational relaxation (VR) (vertical dashed arrows).

2.5 Electron transfer reactions and Marcus theory

The Marcus theory of electron transfer, proposed by Rudolph A. Marcus in 1956, is set to explain the rates of electron transfer. There we have two different types of electron transfer, intramolecular and intermolecular (Figure 3).[5,6]

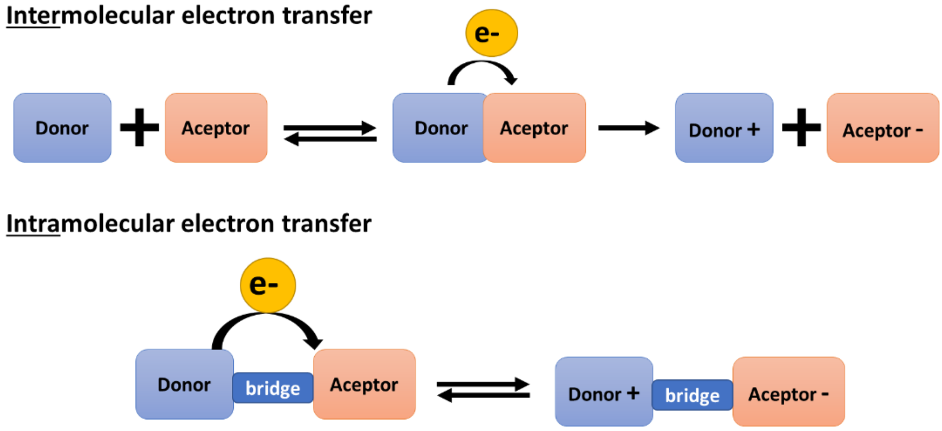

Figure 3. Schematic diagram of the two different types of electron transfer, intramolecular and intermolecular.

We recall Born-Oppenheimer approximation, whereby we can consider electronic and nuclear "subsystems" separately due to very different timescales of their motion. The electron transfer itself is very fast but leaves behind a non-equilibrium configuration of the system, where the solvent molecules are in equilibrium with the D/A configuration, whilst after electron transfer, the electron density distribution is completely different, it becomes D(+)/A(-). Electron transfer process is complete once the solvent molecules rearrange around the final state. The energy required for the rearrangement is called reorganisation energy (Eq. 3), and it is expressed as the sum of the solvent reorganisation and the molecular reorganisation, where λ_s and λ_i are the solvent and intramolecular reorganisation energies:

$$\lambda = \lambda_s + \lambda_i \qquad \text{Eq. 3}$$

This can be represented as is shown in Figure 4 where the reorganisation energy, λ is associated to the free energy curves of the reactant and product states. Where the intersection of the two parabolas we can describe this free activation energy $\Delta G^{‡}$ as:

$$\Delta G^{‡} = \frac{1}{4}\left(1 + \frac{\Delta G_{et}}{\lambda}\right)^2 \qquad \text{Eq. 4}$$

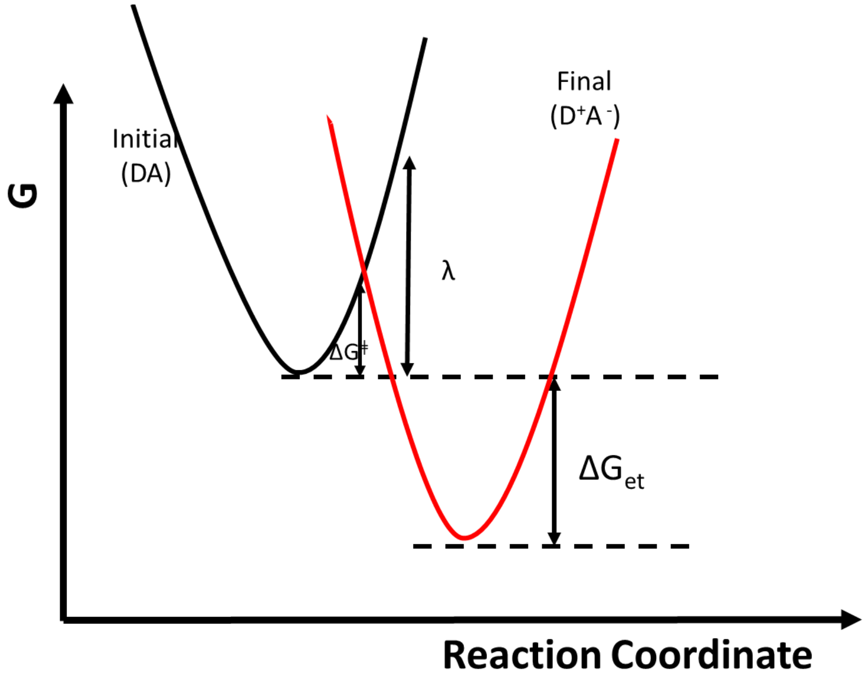

Figure 4. Representation of the initial and final states free energy curves resulting from the electron transfer from the donor (D) to the acceptor (A). The reorganization energy and the free energy charge of electron transfer ΔG_{et} are represented as well.

The rate constant of a reaction is given by:

$$k_{et} = Ae^{-\Delta G^{\ddagger}/k_B T} \qquad \text{Eq. 5}$$

By combining the free energy activation ΔG‡ and the rate constant equations (Eq. 4 and 5), we obtained:

$$k_{et} = Ae^{-(\lambda+\Delta G_{et})^2/4\lambda k_B T} \qquad \text{Eq. 6}$$

This resultant Figure 6predicts the existence of the famous 'inverted region' in conjunction with the quadratic dependence of ΔG‡ and ΔG$_{et}$. This can be explained more clearly in Figure 5.

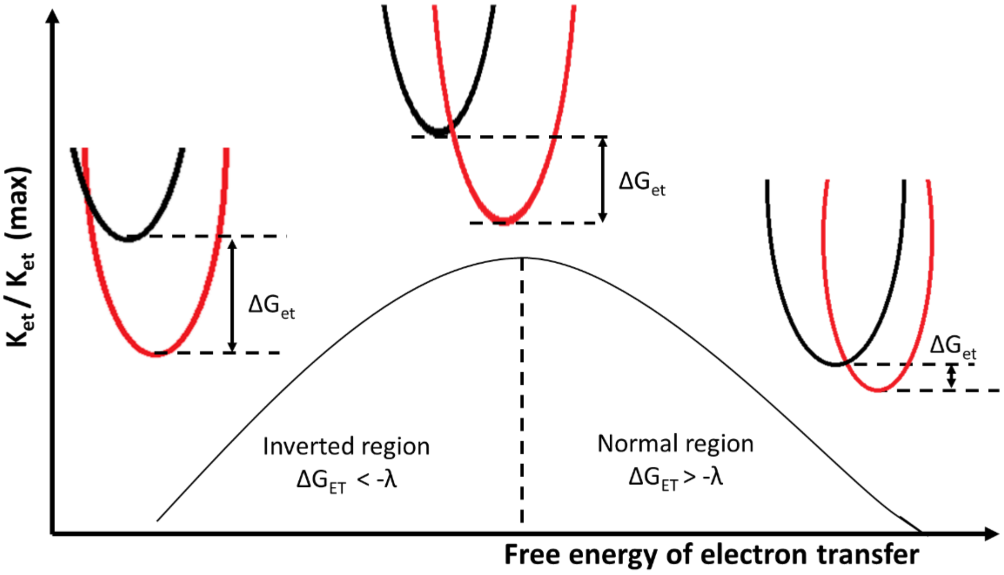

Figure 5. Marcus Theory representation of inverted and normal regions and the rate of ET and the driving force is increased.

Where, when $\Delta G_{et} = -\lambda$ the rate of electron transfer is at its maximum, any increase of the driving force will results in a reduction of the rate of electron transfer.[5,7]

2.6 Electronic transitions in TM complexes

Transition Metal (TM) complexes have many desirable photophysical properties that make them suitable for different applications such as in Dye Sensitised Solar Cells (DSSC), photodynamic therapy, and molecular light-harvesting systems (AP), to mentioned some of them.[8–10]

Not only their photophysical properties make them attractive, but also their facility to be tuned to obtain the ‘desirable’ photophysical properties. This can be achieved by using different ligands than can be bonded to the metal relatively easy. Some ligands can be tuned to modify the absorption of the lowest energy level to make them match with the solar spectrum irradiation. TM complexes have different types of transitions that can happen depending on the nature of their ligands, therefore the involved orbitals. Metal centred (MC) transitions are transitions that happen between the d-orbitals of the TM, d-d transitions typically have extinction coefficients lower than the rest ($1 - 100$ dm^3 mol^{-1} cm^{-1}).[11]

Electronic transitions between molecular orbitals that are localised on different parts of the TM complex resulting in a big change in the electron density distribution. These transitions are known as charge transfer (CT) transitions and can be different depending on their behaviour, classified as follows:

MLCT Transitions of this nature are known as metal-to-ligand charge transfer. A transition from an orbital of mainly metal character to an orbital of mainly ligand character.

LMCT Transitions of this nature are known as ligand-to-metal charge transfer. A transition from an orbital of mainly ligand character to an orbital of mainly metal character.

LLCT Transitions of this nature are known as ligand-to-ligand charge transfer. A transition from an orbital of mainly ligand character to an orbital localised on another ligand.

There is another type of transition that contributes to the final absorption spectra of the TM complexes and those are the ligand-localised transitions. Such transitions occur between orbitals localised on a ligand. This type of ligands exhibit $\pi\pi*$ absorption bands. And their transitions are not forbidden by the Laporte selection rule, therefore often observed as intense absorption bands (10000 − 100000 dm^3 mol^{-1} cm^{-1}).

The $\pi\pi*$ transitions occur normally at higher value energies than CT transitions, (200 – 400 nm). This effect makes them more sensitive to polarity of solvents, leading to a solvatochromic behaviour.

2.7 Quenching of an excited state

This process happens when one molecule transfers an electron (or energy) from its excited state to another molecule. Quenching is the process of reducing the excited state population of a molecule, normally by intermolecular process, but in some cases some molecules can present intramolecular ET processes making them to quench themselves. There are two types of quenching processes: one is dynamic and another one static (Figure 6). The static process occurs in the ground state, where the molecule that acts as a quencher forms a complex with the molecule M that acts as chromophore, changing the absorption properties of this last one, which prevents the emissive state M* from being populated. This interaction changes the quantum yield of emission but does not affect the lifetime of the M*. The second type of quenching is the dynamic process, where the molecule in the excited state (M*) interacts with the quencher molecule (Q), transferring electrons or energy to Q. This process adds an additional decay channel to M*, therefore, the overall emission yield and lifetime of the excited state M* is reduced.

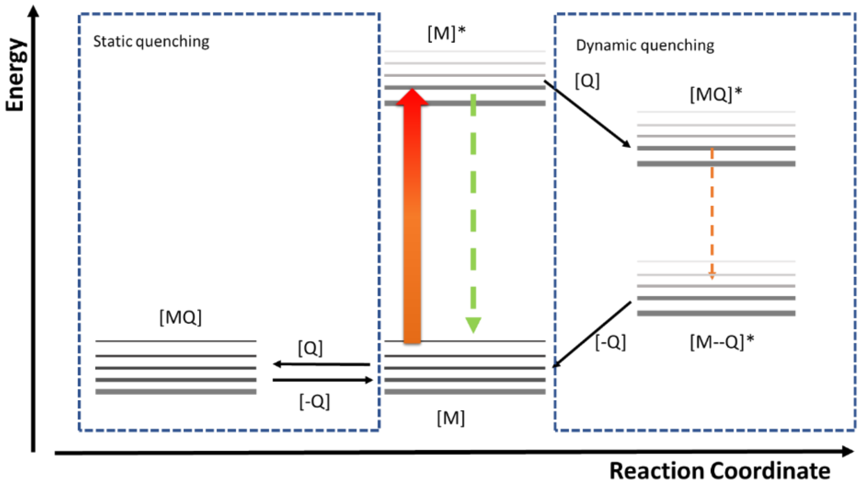

Figure 6. Energy level diagram for different types of quenching processes associated to an emissive molecule and a quencher.

The process of quenching can be quantified by the Stern-Volmer relationship (Eq. 8). There, I_0 is the intensity of the emission without the quencher, I is the emission intensity with the quencher, K is the equilibrium constant of the interaction between the emissive molecule and the quencher in the ground state, [Q] is the quencher concentration, τ_0 is the excited state lifetime of the emissive molecule without the quencher, τ is the excited state lifetime with the quencher, and k_q is the rate constant for the excited state quenching reaction.

$$\frac{I_0}{I} = \frac{\tau_0}{\tau} = 1 + k_q \tau_0 [Q] \qquad \text{Eq. 8}$$

The Stern-Volmer equation can help us to identify the type of quenching we have, dynamic or static. For the static quenching, we will have a linear relationship between I_0/I and [Q], and for this case, the emission intensity will decrease as we increase the quencher concentration, and the lifetime will not change. If the molecules undergo only dynamic quenching, both I_0/I and τ_0/τ will have a linear, and identical, relationship with [Q].

The Stern-Volmer equation can be used to determine the quenching rate constant (k_q) when both quenching mechanisms are possible. If both static and dynamic quenching take place, the relationship between [Q] and τ_0/τ remains linear, and one can does not distinguish this case from the pure dynamic quenching as the static quenching contribution has no effect on the observed emission lifetime. In this case, the equation 8b can be used to obtain k_q, but as the relationship of I_0/I and [Q] now is non-linear and there is a quadratic dependence of [Q] on the emission intensity, changing the equation as follows (Eq. 7):

$$\frac{I_0}{I} = (1 + K_s[Q])(1 + \tau_0 K_q[Q]) \qquad \text{Eq. 7}$$

Figure 7 illustrates different plots for dynamic and static quenching wherein the plot I_0/I vs [Q] a linear gradient indicates either static or dynamic quenching and a non-linear gradient indicates both static and dynamic quenching is happening. And in the plot τ_0/τ vs [Q], we can individually identify the type of quenching whereas a gradient of zero will indicate a static quenching and a linear gradient will indicate a dynamic quenching.[12]

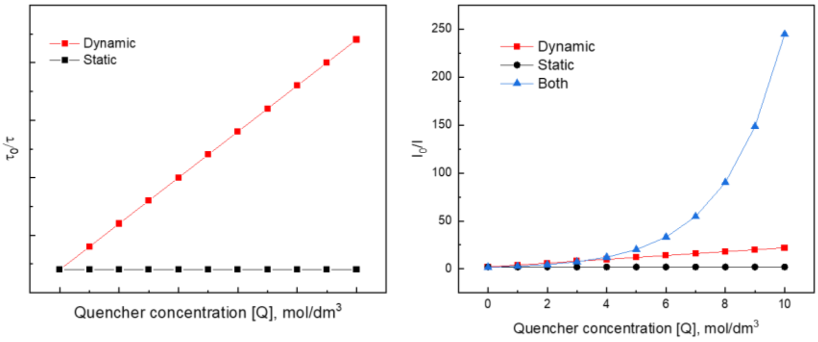

Figure 7. Stern-Volmer plots for dynamic and static quenching

2.8 Fourier Transform Infrared Spectroscopy (FTIR)

Infrared spectroscopy is a very valuable technique to investigate iron carbonyl complexes since the CO ligands on a metal centre give rise to characteristic IR-absorption bands, usually around 1800 - 2100 cm^{-1}. The vibrations of the -CO ligands (ν_{CO}) cause a change in the dipole moment, and hence are IR-active. The frequency of ν_{CO} is a sensitive indicator of the electron density on the -CO ligand and on the metal centre.

There are different interactions between the metal centre and the carbonyl ligand: ligand-to-metal σ-bonding, and the metal-to-ligand d→π*-back bonding interactions. This last one pushes electron density from the metal-d-orbitals into the antibonding π*-orbitals of the CO ligand, weakening the C-O bonding and decreasing the vibrational stretching frequencies ν_{CO}.

The more electron density is available on the metal, the larger is this effect and weaker the CO bond becomes, and this can be translated into a shift of the vibrational frequency towards lower wavenumbers.[13]

Another feature is the number of the ν_{CO} bands. This will depend on the symmetry of the complex and the number of CO ligands. Figure 8 shows the experimental IR spectra for $Fe_2(bdt)(CO)_6$ recorded in MeCN, used as a comparison in this work. The shape of the spectra is representative of the samples studied in this thesis.

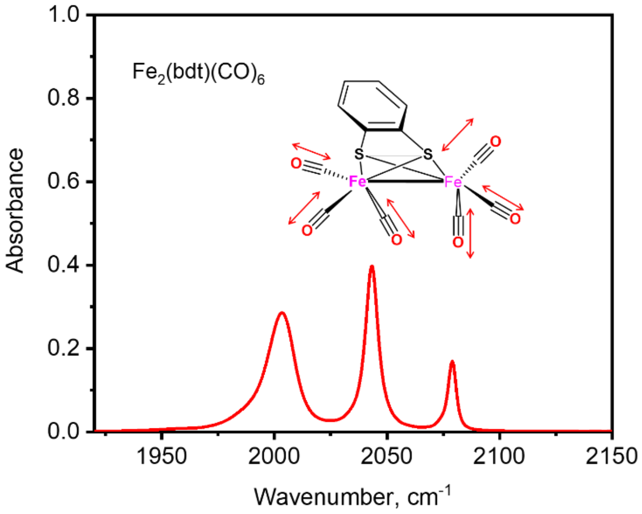

Figure 8. IR experimental spectra recorded in MeCN showing the stretching frequencies of the CO ligands for $Fe_2(bdt)(CO)_6$.

2.9 Pump-probe spectroscopy

Many of the electron transfer processes happening in nature occur on a different range of timescales form seconds to nanoseconds (10^{-09}), or others much faster like picoseconds (10^{-12}) or femtoseconds (10^{-15}), including molecular vibrations, photon absorption and emission. Ultrafast or also so-called time-resolved spectroscopy is the area of science that explores these ultrafast processes in atoms, molecules, crystals, and materials using light-based spectral techniques. To understand the ultrafast photophysical processes, we need high time resolutions, and this can be achieved by using appropriately short laser pulses. Pump-probe is a technique that uses pulsed lasers, where a narrowed excitation pulse called “pump” is used to populate an initial excited state. Then a broadband pulse called “probe” is used to monitor the spectral changes in the samples as these excited states start to relax, coming back to their ground state. These pump and probe pulses need to be synchronised by the laser system; the pump-probe delay is controlled by an optical delay stage of variable path lengths.

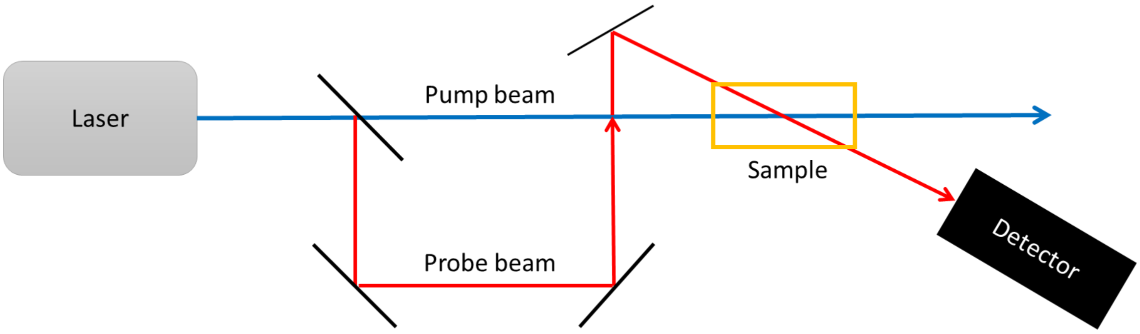

Figure 9. Pump-probe spectroscopy set up. Whereas the laser is split into pump and probe beams. The pump beam excites the sample and the [probe interacts with the sample and then is detected. Laser “hits” a beam splitter, the rest of / lines are mirrors.[14]

The pulses, “pump” and “probe” generated from the laser, are controlled by a chopper in charge of reducing the repetition rate of the narrowband excitation pulses into half the repetition rate of the probe. Then this sequence of pulses allows us to record the probe pulses with and without excitation, which give us spectra of the differential absorption (ΔA), where the positive bands correspond to the excited state transient absorption and the negative bands to the ground state bleaches(Figure 9)(Eq. 8).

$$\Delta A = -log\ (\frac{I_{(pump\ on)}}{I_{(pump\ off)}}) \qquad \text{Eq. 8}$$

There are different types of pump-probe spectroscopies, defined by the region of the electromagnetic spectrum where the pump and the probe fall within. The ones used in this project are: Transient Absorption (TA) that uses a UV-vis pump (267 to 800 nm) and UV-vis-NIR probe (340 to 1500 nm); and Time-resolved infrared (TRIR) that uses a UV-vis pump (267 to 800 nm) and a mid-IR range probe (2500-1200 cm^{-1}).[15,16]

Both techniques are used to monitor relaxation of the electronic excited states after their excitation using visible light[17].

2.10 Electrochemical techniques

a. Cyclic Voltammetry

Electrochemical techniques are widely used for the characterization of redox catalysts. Since redox catalysis involve both electrochemical (electron transfer) and chemical steps (proton transfer), these two processes can be decoupled using an aprotic solvent that allows only the redox reaction to occur. These redox processes can be determined by cyclic voltammetry, where we can follow the reduction and oxidation of the complexes by the changes in the current versus an applied potential. For these measurements, a conventional 3-electrodes cell is used, with an Ag/AgCl electrode as a reference, Pt as counter electrode and a glassy-carbon as working electrode (Figure 10). Normally it uses TBAPF$_6$ (0.1 M – 0.4 M) as electrolyte for non-water-soluble systems, and the typical concentration of the compound studied is 1 mM; this concentration should be sufficient to avoid large ohmic voltage losses across the electrolyte [18].

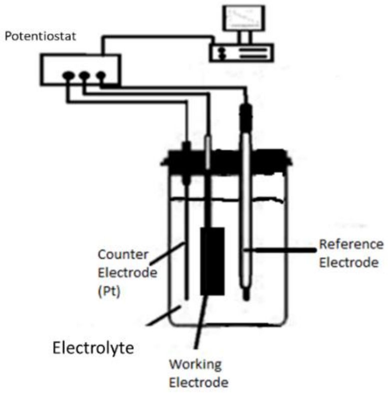

Figure 10. Simplified scheme of an Electrochemical 3-electrode arrange cell.

The applied potential difference is measured relative to the reference electrode, where the use of different reference electrodes leads to different measured values for the redox potentials. To standardize, all the potential redox values measured in this work are referenced against the ferrocene/ferrocenium redox couple (Fc^0/Fc^+). The obtained plot of the measured current against the applied potential is called “cyclic voltammogram”, where we can observe a redox couple if a redox process is occurring. Under ideal conditions, the redox process follows the Nernst equation:

$$E = E^0 - \frac{RT}{nF} \cdot ln\frac{a_{red}}{a_{ox}} \qquad \text{Eq. 9}$$

Whereas E is the potential of the electrochemical cell, E_0 is the standard potential, R is the gas constant, T is the temperature, n is the number of electrons involved in the redox process, F is the Faraday constant, and the a_{red} and a_{ox} are activities of the reduced and oxidized species in solution [18].

When coupled with a spectroscopic technique like FTIR, one can assign the different species formed during reduction or oxidation to catalytic intermediaries. This technique is called Spectroelectrochemistry (SEC) and is useful to monitor when any species are oxidized or reduced and assign these changes to the spectroscopic changes in the spectra. These experiments are performed in an optically transparent thin-layer electrochemical cell (OTTLE® cell), equipped with Pt grids and wires as working electrodes, counter electrodes and an Ag wire as a pseudo reference electrode (Figure 11).[19]

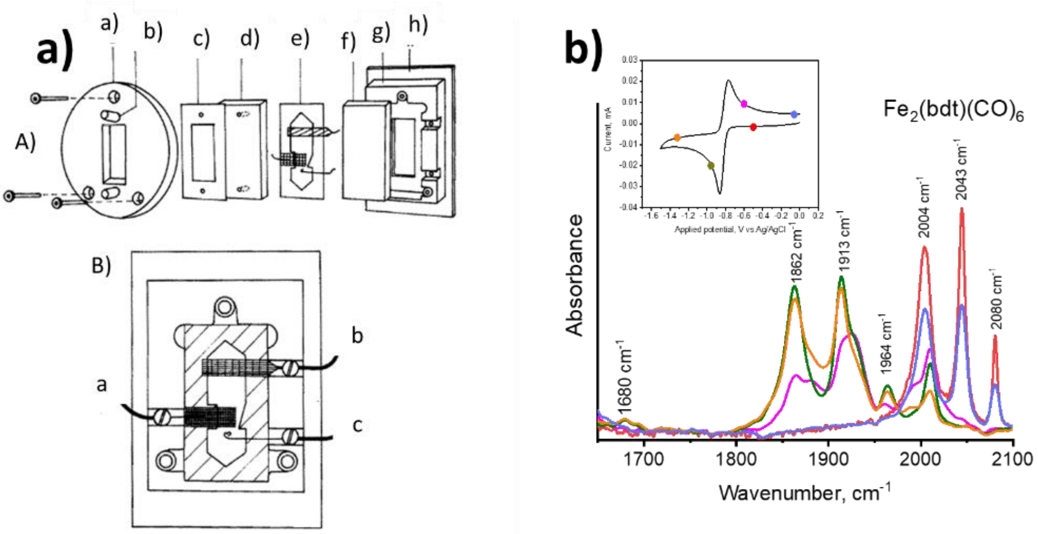

Figure 11. **a)** (A) Schematic diagram of the IR O'ITLE cell with the three-electrode system placed inside the thin layer. (a) Steel pressure plate; (b) inlet; (c) Teflon gasket; (d, f) front and back KBr windows; (e) polyethylene spacer with melt-sealed electrodes; (g) Teflon holder; (h) back plate. (B) Front view of the cell composed of the parts (e)-(h) of <A) showing the position of the electrodes and their soldered contacts with Cu conductors fixed by screws. (a) Au minigrid working electrode with twinned contact Ag wire; (b) Pt mesh auxiliary electrode; <cl Ag wire pseudo reference electrode. **b)** FTIR and CV (inset) spectra collected with the OTTLE® cell for the complex $Fe_2(dpet)(CO)_6$ on dry acetonitrile.[19]

b. Photocurrent transients

Current-Voltage measurement is an essential technique to determine the performance characteristics of the photoanodes for water splitting; from this, we can obtain the following information:

- photocurrent density and energy conversion efficiency as a function of the applied potential
- the dark current as a function of the applied potential
- the sign of the photocurrent
- photocurrent onset potential
- electron vs hole-transport limitations and transient effects that indicate recombination

This technique measures the photocurrent while sweeping the potential at a constant scan rate (1 to 50 mV/s). The measurement can be done with and without illumination or by switching the light ON and OFF at a fixed frequency.

c. Photocurrent-voltage curves

The photocurrent-voltage curve is another proper electrochemical technique used in this project, which allows us to record the photo-response of a material after the excitation with a source of light. Another type of curve used is current vs time (Chronoamperometry); this type of analysis, the so-called “ON-OFF”, are recorded while switching the light on and off with a shutter recording the changes in the photocurrent (Figure 12).

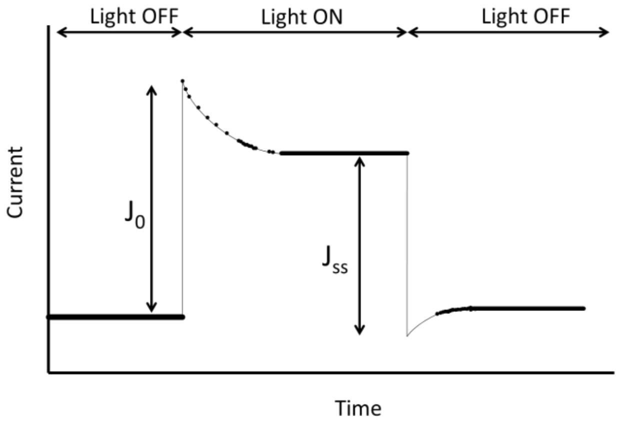

Figure 12. Example of a current vs. time curve using $BiVO_4$ under high-intensity illumination with a 364 nm light.[20]

The photocurrent density under 1 sun (1000 W/m^2) is a standard metric to determine the optimal photoresponse, and to be able to compare the photocurrent for different samples. When the light is switched on, the photocurrent immediately rises to its peak value (J_0); after this peak will decay to a steady-state value (J_{ss}) as a result of the photogenerated electrons and holes recombination (J_0-J_{ss}). This recombination process typically happens due to an accumulation of electrons in the bulk, accumulations of holes on the surface, or trapping electrons or holes at the surface states.

d. Electrochemical Impedance Spectroscopy (EIS)

EIS is a powerful electrochemical analysis technique that measures the impedance of an electrochemical system in a range of frequencies. It has a wide range of applications for the characterization of materials for different applications such as batteries, fuel cells, dye-sensitized solar cells, photoelectrochemical cells. This technique can determinate the donor density and flat band potential on a thin photoelectrode through the Mott-Schottky plot using a simple three-electrode cell arrangement.

The main component of a PEC cell is the semiconductor, which converts incident photons to electron-hole pairs. These electrons and holes are spatially separated from each other due to the presence of an electric field inside the semiconductor.[21] The photogenerated electrons are swept toward the conducting back-contact and are transported to the metal counter-electrode via an external wire. At the metal, the electrons reduce water to form hydrogen gas. The photogenerated holes are swept toward the semiconductor/electrolyte interface, where they oxidise water to form oxygen gas.

The position of the band edges with respect to the redox potentials in the electrolyte is called "flat band potential", Φ_{FB}. And is potential need it to be applied to the semiconductor to reduce the band bending to zero. This flat band potential denotes the position of the fermi level of the semiconductor with respect of the reference electrode potential (Figure 13). This means that if the E_{fb} is slightly below the conduction band edges that it accurately reflects the thermodynamic ability of an n-type semiconductor to reduce water to hydrogen. [22–24]

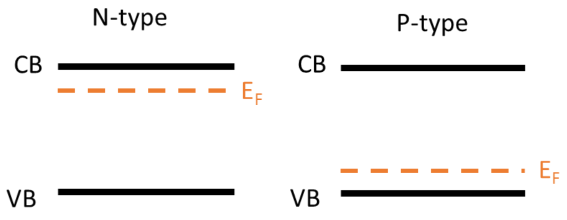

Figure 13. Schematic representation of the flat band and potential position on an electronic band diagram for a p-type and an n-type semiconductor.

To determinate the position of the flat bland potential of a thin film photoelectrode we need to measure the impedance (Z*) of the system, which is a measure of the opposition to electrical flow and is given in ohms using a frequency analyser.

The frequency analyser (FRA) generates a small sinusoidal voltage of a specific frequency and amplitude, which modulates the potential of the sample via the modulation input of the potentiostat. Therefore, the impedance can be represented as a vector in the complex plane.

As the challenge in this technique is to distinguish the C_{sc} from other, capacitive, or resistive in nature, contributions of the PEC cell. Examples of resistive elements present in this systems are the semiconductor bulk, the electrolyte, contacts, and charge transfer resistance. All these contributes to the modelled so-called *equivalent circuit.* But extract the space charge capacitance form the overall response of such a complicated circuit is not possible, instead we can ignored many of these contributions leading to a much more simplified circuit (Figure 14a), whereas we can see that the real part of the impedance is Z_{Re} and corresponds to the resistance R, and the imaginary part Z_{im} is equal to $\frac{1}{\omega C_{sc}}$, the overall impedance is given by:

$$Z^{*} = R - j\frac{1}{\omega C_{sc}} \qquad \text{Eq. 10}$$

ω angular frequency at which the impedance is measured (ω=$2\pi f$) and j (=$\sqrt{(-1)}$) indicates that Z* is a complex number (Figure 14b).[25,26]

When we plot the real part of impedance against the imaginary part, that gives us the Nyquist plot. (Figure 14c). This plot gives us a piece of quick qualitative information about the sample.

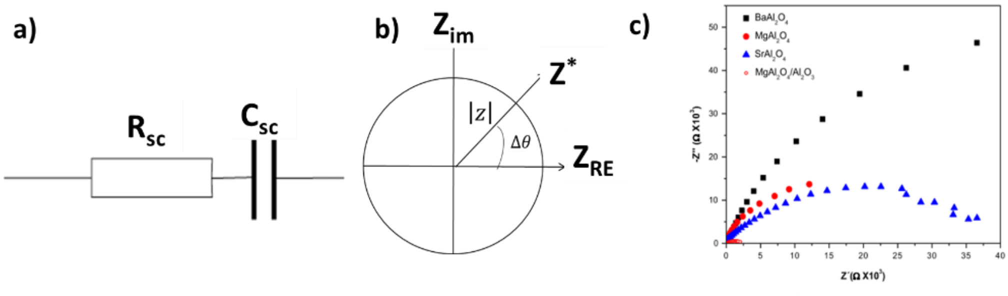

Figure 14.(a) Schematic diagram of a Circuit that is often encountered in practice for photoelectrodes.(b) Representation of the imaginary and real part of the circuit from where the Nyquist plots is constructed.(c) Nyquist plot determined for the aluminates $MgAl_2O_4$, $BaAl_2O_4$, $SrAl_2O_4$ and $MgAl_2O_4/Al_3O_4$ at -0.6 V in a range of frequencies from 0.01 to 100 kHz.[27]

This means that we can determine the donor density by measuring the space charge capacitance from the imaginary part of the impedance and then as measuring the impedance from this imaginary part as a function of the applied potential, we can obtain the Mott-Schottky curve by measuring the charge capacitance C_{sc}, as function of the applied potential, ϕ_A following the Mott-Schottky equation (Eq. 13) :

$$\frac{1}{C_{sC}^2} = \frac{2}{\varepsilon_0 \varepsilon_r e N_D A^2}\left(\phi_A - \phi_{F_B} - \frac{kT}{e}\right) \qquad \textit{Eq. 11}$$

The Mott-Schottky plots the slope of the inverse of the space charge capacitance vs applied potential should give a straight line with a slope that is proportional to 1/ND Donor density, while the intercept with the potential axis gives the flat band potential (Figure 15).

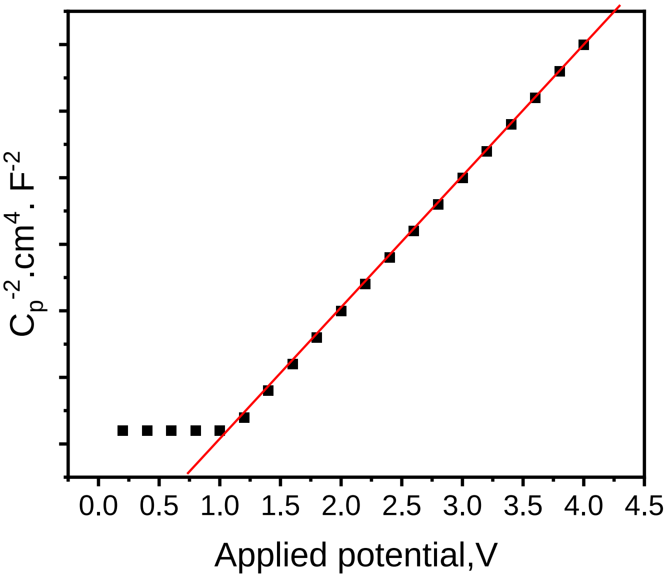

Figure 15. Schematic representation of a Mott-Schottky plot.

2.11 References

1 L. Hammarström and S. Hammes-Schiffer, *Acc. Chem. Res.*, 2009, **42**, 1859–1860.

2 F. Niu, D. Wang, F. Li, Y. Liu, S. Shen and T. J. Meyer, *Adv. Energy Mater.*, 2020, **10**, 1–24.

3 C. Bohne, Q. Pan, P. Ceroni, K. Börjesson, J. Rohacova, F. Lewis, A. Vlcek, D. M. Bassani, F. Würthner, A. Sartorel, A. P. De Silva, D. Nocera, F. Scandola, C. Lemon, C. Allain, G. W. Brudvig, S. Marchesan, V. Sundstrom, S. Campagna, S. W. Sheehan, P. A. Plötz, F. Monti, J. M. Kelly, E. Gibson, M. Maneiro, A. Harriman, A. Ruggi, E. Galoppini, R. Thummel, J. Weinstein, J. Vos, O. Ishitani, D. Gust and A. Díaz-Moscoso, *Faraday Discuss.*, 2015, **185**, 187–217.

4 J. D. Shipp, University of Sheffield, 2021.

5 E. J. Piechota and G. J. Meyer, *J. Chem. Educ.*, 2019, **96**, 2450–2466.

6 A. Arrigo, R. Mazzaro, F. Romano, G. Bergamini and P. Ceroni, *Chem. Mater.*, 2016, **28**, 6664–6671.

7 P. J. de P. Atkins, *Physical Chemistry*, Oxford University Press, 8th edn., 1961, vol. 272.

8 J. M. Hsieh, M. L. Ho, P. W. Wu, P. T. Chou, T. T. Tsai and Y. Chi, *Chem. Commun.*, 2006, **6**, 615–617.

9 A. Carella, F. Borbone and R. Centore, *Front. Chem.*, 2018, **6**, 1–24.

10 F. Wen, X. Wang, L. Huang, G. Ma, J. Yang and C. Li, *ChemSusChem*, 2012, **5**, 849–853.

11 H. C.E. and S. A.G., *Inorganic Chemistry*, Pearson Education Limited, 2008.

12 J. Keizer, *J. Am. Chem. Soc.*, 1983, **105**, 1494–1498.

13 S. Pullen, Uppsala Universitet, 2017.

14 H. Abramczyk, *Introduction to Laser Spectroscopy.*, Elsevier, Amsterdam, 1st editio., 2005.

15 J. D. Shipp, H. Carson, S. J. P. Spall, S. C. Parker, D. Chekulaev, N. Jones, M. Y. Mel’nikov, C. C. Robertson, A. J. H. M. Meijer and J. A. Weinstein, *Dalt. Trans.*, 2020, **49**, 4230–4243.

16 M. Delor, P. A. Scattergood, I. V. Sazanovich, A. W. Parker, G. M. Greetham, A. J. H. M. Meijer, M. Towrie and J. A. Weinstein, *Science (80-.).*, 2014, **346**, 1492–1495.

17 R. Berera, R. van Grondelle and J. T. M. Kennis, *Photosynth. Res.*, 2009, **101**, 105–118.

18 N. Elgrishi, K. J. Rountree, B. D. McCarthy, E. S. Rountree, T. T. Eisenhart and J. L. Dempsey, *J. Chem. Educ.*, 2018, **95**, 197–206.

19 M. Krejčik, M. Daněk and F. Hartl, *J. Electroanal. Chem. Interfacial Electrochem.*, 1991, **317**, 179–187.

20 M. G. Roel van de Krol, *Photoelectrochemical Hydrogen Production*, 2012, vol. 1.

21 K. Scott, *Electrochemical Principles and Characterization of Bioelectrochemical Systems*, Elsevier Ltd., 2016.

22 A. Hankin, F. E. Bedoya-Lora, J. C. Alexander, A. Regoutz and G. H. Kelsall, *J. Mater. Chem. A*, 2019, **7**, 26162–26176.

23 K. Pandey, S. T. A. Islam, T. Happe and F. A. Armstrong, *Proc. Natl. Acad. Sci.*

U. S. A., 2017, **114**, 3843–3848.

24 F. Gao, Y. Wang, D. Shi, J. Zhang, M. Wang, X. Jing, R. Humphry-Baker, P. Wang, S. M. Zakeeruddin and M. Grätzel, *J. Am. Chem. Soc.*, 2008, **130**, 10720–10728.

25 J. Bisquert, *J. Phys. Chem. B*, 2002, **106**, 325–333.

26 Metrohm, Electrochemical impedance spectroscopy (EIS). Part 1 – Basic principles *Metrohm Autolab B.V.*, 2011, 1–3.

27 C. Gómez-solís, S. L. Peralta-arriaga, L. M. Torres-martínez, I. Juárez-ramírez and L. A. Díaz-torres, 2017, **188**, 197–204.

Chapter 3

Photo physics of Fe-Fe complexes as hydrogenase mimics for hydrogen evolution.

This chapter shows the studies done to understand and reveal the photochemical and photo physical properties of the new reported hydrogenase mimic [Fe-Fe] complex $Fe_2(dpet)(CO)_6$ using the $Fe_2(bdt)(CO)_6$ as comparison.

A version of this chapter is in process of publication.

Title: Photo physics of Fe-Fe complexes hydrogenase mimics for hydrogen evolution.

Peralta-Arriaga Samantha L., Fernández-Teran Ricardo J., Royle Catherine, D. Shipp James, Morris Michael, Chekulaev Dimitri, Weinstein Julia A.*.

Department of Chemistry, University of Sheffield, Sheffield S3 7HF, United Kingdom.

*Corresponding author: Julia.Weinstein@sheffield.ac.uk

3.1 List of figures

3.2 Introduction

Hydrogen is one of the promising fuels of the future.[1] To develop a sustainable technology to produce this fuel requires using sunlight as the primary energy source.[2] Accordingly, a lot of effort has been invested in finding a sustainable way to generate hydrogen from water, but most used various Noble-metal catalysts. Iron-based catalysts would offer a low cost, sustainable alternative.[3–7]

Photosynthesis is one of the most important processes on nature, providing the earth with an estimated range between 120 000 TW of energy, that corresponds to nearly the 1% of the total solar energy reaching the earth exceeding our current global demand of ~16TW.[8] From this, around 1 TW is used to cover human needs.[9,10] Photosynthesis occurs in different types of organisms, such as green sulphur bacteria, purple bacteria, or filamentous phototropic cyanobacteria. But only cyanobacteria, plants and algae use the oxygenic photosynthetic process where water is split into protons and oxygen.[11–14]

Amongst different types of hydrogenases - enzymes in charge of the proton reduction, [NiFe], [FeFe], and [Fe] hydrogenases[15,16] - the [FeFe] ones are the most efficient catalysts. They reduce protons with turnover frequencies (TOF) around 10^3 per second, under low overpotential in water. It is therefore desirable to develop synthetic mimics of [FeFe] hydrogenases for solar water splitting.[1,5]

All hydrogenases share the same central structure formed by sulphur ligands and the biologically unique carbonyl ligands.[17] The active site of hydrogenases (Figure 1), commonly called “H-cluster” is normally consisting of the binuclear centre (Fe-Fe), (Fe-Ni) or (Fe-N), a bridging ligand, and non-protic CN^- or CO ligands.[5,18–20] The H cluster responsible for hydrogen evolution.[19,21–23]

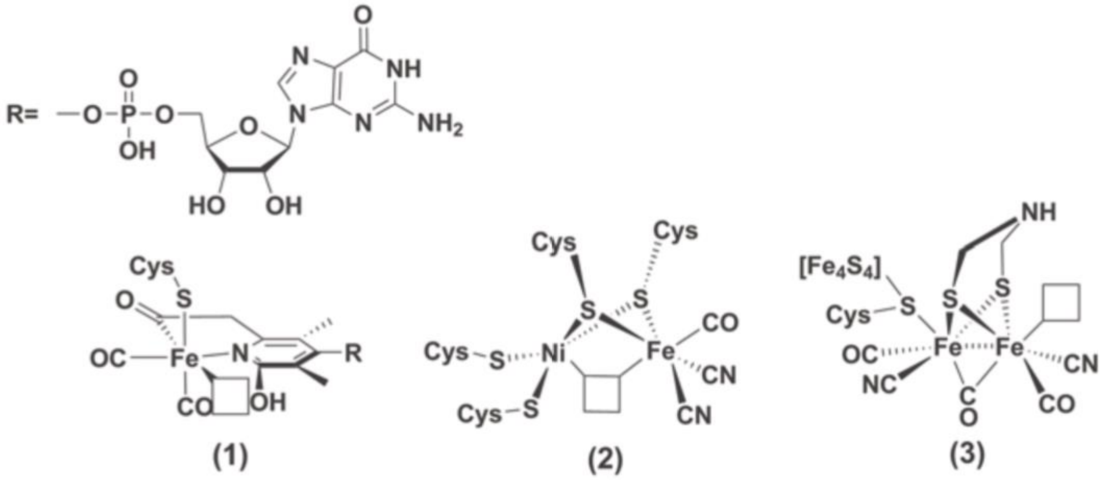

Figure 1. Active sites of different hydrogenase enzyme classes. (1) is the [Fe] hydrogenase, (2) is the [NiFe] hydrogenase and (3) is the [FeFe] hydrogenase active site.[17]

On this active site, the sulphur ligands are soft bases that contribute to make the metal centre softer, which made them more suitable for their interactions with the hydride, this last one also a soft ligand. The carbonyl and cyanide ligands are strong π-acceptors creating low spin metal centres with free orbitals capable of accepting electrons from additional ligands. Also, the fact that the carbonyl ligands are neutral and not negatively charged together with their strong back bonding ability, stabilize the metal centres in low oxidation states necessary for proton reduction.[14]

The catalytic cycle of [FeFe] hydrogenases is presumed to start with a [4Fe-4S]$^{2+}$-Fe(I)Fe(II) state where Fe(II) is the distal iron. This state is known in literature as H_{ox}.[17] Two protons and two electrons are needed to reduce protons to dihydrogen. It should be possible to form the first reduced state using steady-state techniques if the reduction potential for the second reduction is more negative than the first. This seems to be the case for this enzyme and the singly reduced state is formally a [4Fe-4S]$^{2+}$-Fe(I)Fe(I) state, referred to as H_{red} (Figure 2).[24–28]

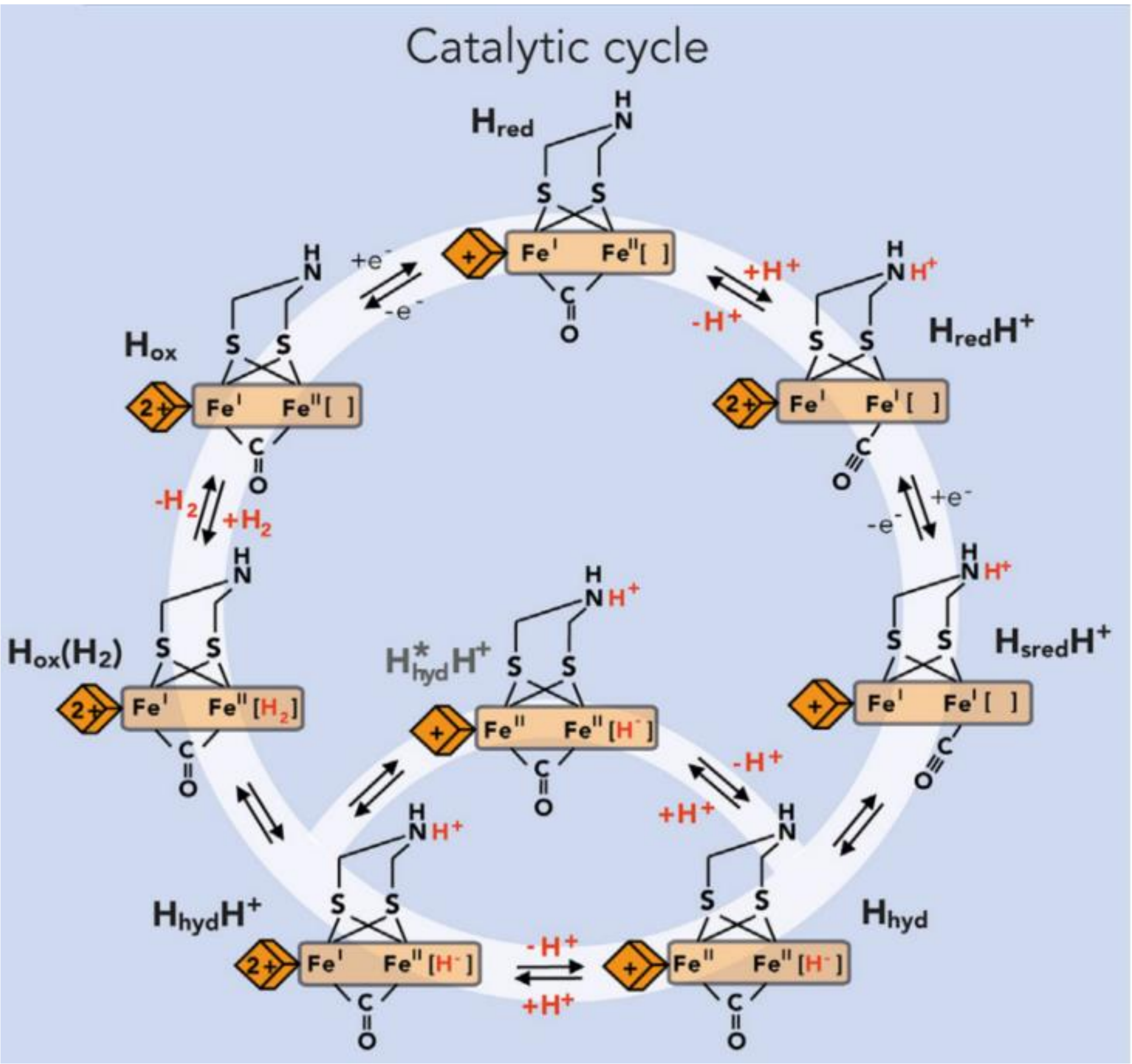

Figure 2. Proposed catalytic cycle for hydrogen conversion by the H-cluster in the [FeFe] hydrogenases. The dark orange diamond represents the [4Fe-4S] and the orange rectangle the [2Fe] subcluster; the oxidation states of the subclusters are given. The states Hox,Hred,HredH+,HsredH+,and Hhyd have been identified by IR spectroscopy under equilibrium or steady-state conditions (printed from REF [26]).

Many [FeFe] mimics has been synthesised which bear different types of aromatic bridging ligands e.g., 1,2-benzene-dithiolate (bdt), alkylic bridging ligands such as ethanedithiolate (edt) or propane-dithiolate (pdt), or azo-dithiolate (adt) ligand.

Catalysts with aromatic bridges are sought after, as those can undergo a reversible two-electron reduction at potentials of approx. –1.3V, considerably less negative than those with the aliphatic (e.g., pdt) bridged ligands, which undergoes an irreversible reduction at –1.67 V (vs Fc^+/Fc^0).[20,29–31] To achieve solar-driven hydrogen production with the [FeFe] mimics requires detailed understanding of excited state dynamics of these complexes, as well as designing those which can be activated by visible light. Previous works reported the stability of $Fe_2(bdt)(CO)_6$ upon reduction in acetonitrile, founding the formation of double reduced species when it is reduced photoelectrochemically, this can be possible since the second reduction is more favourable than the first one, these species can be detected by Spectroelectrochemistry.

For the case of alkylenedithiolate species, the reduction is usually irreversible and can’t be detected so easily, the decomposition path of these species is through the CO loss [32,33].

Different strategies have been incorporated in latest research, like changing the bridges or changes on the ligands or by replacing one of the CO by different ligands[34]. For example, the work by Sun and co-workers reported synthesis of the bioinspired diiron complex, designed with a simple structure containing a pdt bridge and a CO ligand replaced by a water-soluble phosphine ($P(CH_2OH)_3$), which performed the catalytic function using inexpensive electron donors like xanthene PS, Eosin Y, and TEA in water: ethanol solution under alkaline conditions. They found a maximum efficiency for hydrogen production with a TON of 226 after 15 h of reaction under visible light irradiation[35].

Another example is the investigation by Ott et al. where they substituted the ligands on the FeFe core with a variety of aromatic moieties with different electron-withdrawing character i.e., benzene, toluene, 3,6- dichlorobenzene and quinoxaline and studied their effect on the properties of arene-dithiolate complexes ([Fe_2(m-S_2Ar)$(CO)_6$]). They found a direct relationship between increased electron-withdrawing character of the bridging ligands and a lower electron density of the diiron core, resulting in a decreased applied potential that was needed for electrocatalytic proton reduction[36].

All the works previously reported support the idea that an appropriately substituted aromatic dithiolate bridgehead is a promising design strategy for a bioinspired [2Fe2S] to overcome the limitations inflicted by the relatively irreversible reductions at negative potentials that are typical for aliphatic dithiolate bridged catalysts. [34]

With regard to potential photoactivation of hydrogenase mimics, one needs to consider photostability of these [FeFe] complexes. These compounds have been reported to undergo an instantaneous CO loss upon excitation. Kassianis et al. reported the TRIR studies of photochemistry and photo-dynamics of (μ-$S(CH_2)_3S$)$Fe_2(CO)_6$). They stated that the CO loss and the solvent adduct formation occurs on a sub-picosecond time scale while the solvent adduct is observed to remain beyond the 1 ns time window of their experiment.[37] They found three different processes: 7-10 ps, a vibrational cooling on 30-60 ps time scale, and a ~150 ps process, that they ascribed to simultaneously occurring geminate recombination CO and CO-loss product, and vibrational relaxation of the parent molecule.

This work indicates that [FeFe] mimics may not necessarily be suitable as photocatalysts. On the other hand, potentially, they could be photosensitised by a photostable, and more red-light absorbing, photosensitiser.

This work aims to understand the intrinsic photophysical properties and photo-reactivity of the new [FeFe]-hydrogenase mimic complex Fe_2(dpet)$(CO)_6$ (**H2**) which has aromatic groups in the bridging ligand, but is more flexible than the well-known mimic, $Fe_2(bdt)(CO)_6$ (**H1**), and to demonstrate the ability of **H2** as a catalyst in photo-activated hydrogen production.

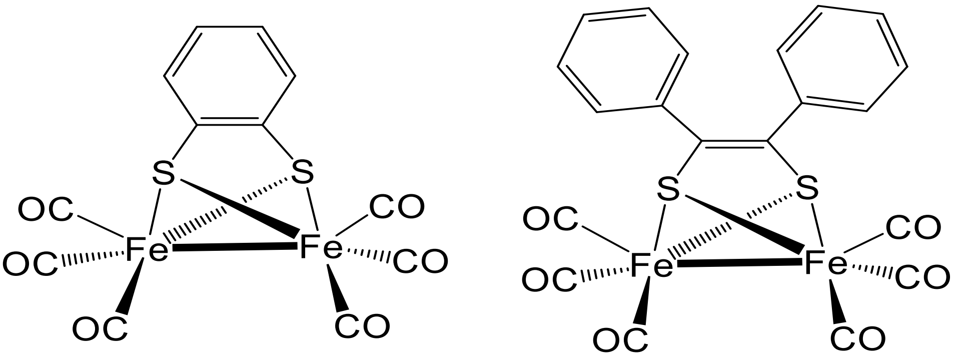

Figure 3. Structures of **H1** $Fe_2(bdt)(CO)_6$ (left side) and **H2** $Fe_2(dpet)(CO)_6$ (right side), studied in this work.

3.3 Experimental section

Synthesis and characterization of Fe-Fe complexes

The Fe-Fe complexes studied in this work, $Fe_2(dpet)(CO)_6$ (**H2**) was synthesized according to the procedure recently published by Michael J. Morris, et al.[29] The compound studied for comparison, $Fe_2(bdt)(CO)_6$ (**H1**) was prepared according to literature method.[38] **H1 and H2** were characterized by NMR spectroscopy, FT-IR spectroscopy, and mass spectrometry. **H2:** IR-absorbances in the region 1900 – 2200 cm^{-1} (in acetonitrile): 2077m, 2042s, 2005s, 1990w cm^{-1}. ^{1}H NMR (DCM) δ 7.20, 7.02 (m, Ph); ^{13}C NMR (DCM)δ 207.8 (CO), 150.2 (CPh), 135.1 (Cipso), 128.9, 128.5, 127.3 (Ph). Mass spectrum m/z 523 (M + H)+. These data are in agreement with those reported previously.[29]

Fourier transform infrared spectroscopy (FTIR) was carried out with a PerkinElmer One Spectrometer using a liquid transmission CaF_2 cell (OMNI Cell®) with a 2 cm^{-1} resolution.

The **Nuclear Magnetic Resonance (NMR)** of the synthetized complexes ^{1}H and ^{13}C spectra were recorded at 400 or 250 MHz on a Bruker Avance 400 spectrometer. Deuterated solvents were purchased from Sigma-Aldrich and were of spectroscopic grade. All chemical shifts are reported in parts per million (ppm), with ^{1}H NMR spectra being calibrated relative to the residual solvent signal.

Mass spectra was analysed in a Water LTC Mass Spectrometry equipment with Atmospheric Pressure Chemical Ionisation (APCI) for non-polar molecules in the mass range 100 to 3000 Daltons.

The redox potentials of **H2** were determined by **Cyclic voltammetry** using an Auto lab PGSTAT100 potentiostat, in a three-electrode cell. Ag/AgCl (0.1 mol L^{-1}), a glassy-carbon electrode and platinum wire were used as a reference, working and counter electrodes, respectively. All measurements were carried out in dry acetonitrile with $[^{n}Bu_4N][PF_6]$ (0.5 M, previously purified by recrystallization from EtOH) as supporting electrolyte. The redox potentials were calculated against the Fc^{+}/Fc^{0} couple as an internal reference. The linear dependence of the current vs the square root of the scan rate for individual redox couples was used to check whether the processes were diffusion controlled.

UV-Vis absorption spectra were recorded on a Cary 50 UV-Vis spectrometer using quartz cuvettes of 1 cm path length.

The photostability of the complexes was evaluated using LED (Thorlabs) at 405 nm at 1 mW/cm^{2} as irradiation source in MeCN and dichloromethane (DCM) using a gas-tight quartz cell to avoid any changes in concentration due to solvent evaporation. Spectra were collected every 10 min up to a total time of 120 min.

The spectroscopic changes upon electrochemical reduction in anhydrous MeCN were investigated by **FTIR (Spectro)electrochemistry** using the same potentiostat and FT-IR spectrometer described above, in an optically transparent thin-layer electrochemical (OTTLE) cell, consisting of two CaF_2 optical windows, Pt grid counter- and working electrodes, and an Ag wire as pseudo-reference electrode.[39]

Femtosecond Transient Absorption (TA) spectroscopy was performed at the Lord Porter Laser Laboratory, University of Sheffield. A Ti:Sapphire regenerative amplifier (Spitfire ACE PA-40, Spectra-Physics) provided 800 nm pulses (40 fs FWHM, 10 kHz, 1.2 mJ). 400 nm pulses for excitation were generated by doubling a portion of the 800 nm output in a β-barium borate crystal within a commercially available doubler/tripler (TimePlate, Photop Technologies). White light supercontinuum probe pulses in the range 340–790 nm, were generated by tightly focusing ca. 1 µJ of the 800 nm output on a CaF_2 crystal (continuously displaced to avoid damage). Detection was achieved using a commercial transient absorption spectrometer (Helios, Ultrafast Systems) using a 2048-pixel CMOS sensor for the UV-vis spectral range. The relative polarisation of the pump and probe pulses was set to the magic angle of 54.7˚ for anisotropy-free measurements. Samples were held in 2 mm path length quartz cells and were stirred during experiments. The optical density at the excitation wavelength was kept at approximately 0.5. The optical density across the probe range was kept below 1.0. Excitation energies were kept below 2 µJ.

Time-resolved infrared spectroscopy (TRIR) was performed at the Lord Porter Ultrafast Laser Spectroscopy Laboratory, University of Sheffield. 400 nm pulses for sample excitation were generated as stated above. A phase-locked optical chopper was used to reduce the repetition rate of the 400 nm excitation pulses to 5 kHz. The broadband mid-IR probe pulse, centred at 2000 cm^{-1}, was produced by an automated commercially available optical parametric amplifier equipped with a difference frequency mixing stage (TOPAS, Light Conversion). A long pass filter was used to remove unwanted NIR light emitted collinearly with the emitted mid-IR, the divergent mid-IR light was then collimated with a telescope. A half-wave plate was used to set the relative polarisation of the 400 nm and mid-IR beams to the magic angle of 54.7° for anisotropy free measurements. The mid-IR light was divided with a 50% transmittance germanium beam splitter, where the reflected light was used as the probe and the transmitted light was used as a reference beam. The pump, probe, and reference beams were focussed on the sample. Samples were prepared in demountable liquid cells (Harrick Scientific) equipped with 2 mm CaF_2 windows. The pathlength used was typically 650 μm. To minimise photodecomposition of the complexes, approx. 20 ml of the sample solution were recirculated with a peristaltic pump and restored with a vertical/horizontal translation stage during irradiation. For all experiments, the optical density across the carbonyl mid-IR spectral region was kept below 1.0.

After passing through the sample, the probe and reference beams were divided with a 50% transmittance beam splitter, where the transmitted and reflected beams were focussed onto individual detectors. Detection was achieved with two liquid-nitrogen-cooled 128-pixel HgCdTe (MCT) arrays (FPAS, Infrared Systems Development). For each detector, the mid-IR probe was focussed onto a 96-pixel array and the reference was focussed onto a 32-pixel array. Monochromators utilising automated interchangeable grating turrets (50, 100, 120 gr mm^{-1}) were used to select the desired spectral regions for data collection. During data processing, the reference data was interpolated and subtracted from the probe data to improve the signal-to-noise ratio, difference spectra were then calculated to produce the TRIR data.

Density functional theory (DFT) calculations were performed in Gaussian 16 rev. C.01,[40] using the B3LYP functional and a split basis set consisting of the 6-311G (d,p) basis set for all light atoms and the LANL2DZ ECP for the Fe atoms. Solvent effects were accounted for by the Gaussian implementation of the IEF-PCM model for MeCN and DCM. For each complex, the ground state (S_0), the lowest triplet excited state (T_1), as well as the corresponding singly and doubly reduced species were calculated in both MeCN and DCM and optimised under tight convergence criteria. Convergence to a minimum was confirmed by frequency calculations, which did not yield any negative frequencies. The frequencies obtained from these calculations were scaled by 0.973 to better match the experimentally obtained frequencies and convoluted with a Lorentzian function with a FWHM of 8 cm^{-1} to generate the calculated absolute and difference spectra in all cases. Time-dependent density functional theory (TD-DFT) calculations were performed under identical conditions as described above, considering the lowest 30 singlet and 30 triplet states. The calculated UV-Vis absorption spectra were generated by convolution with a Gaussian function with a uniform FWHM of 1850 cm^{-1} and were shifted to higher energies to better match the experiment by 0.35 eV (**H1**) and 0.25 eV (**H2**), respectively. Charge density difference isosurfaces were generated from the Gaussian outputs and formatted checkpoint files with the help of the MultiWfn program (version 3.7).[41] The calculations were performed by Dr R Fernadez-Teran.

3.4 Results

UV-Visible and FTIR Spectroscopy

The UV-Vis absorption spectra of both **H1** and **H2** (Figure 4) show an intense band in the range of 300-375 nm (λ_{max} = 333 nm, ε = 10400 cm^{-1} mol^{-1} L) for **H1** and at 320-400 nm (λ_{max} = 340 nm, ε = 7970 cm^{-1} mol^{-1} L) for **H2.**[42] The absorption band at lower energies (ca. 460 nm) is been assigned to the metal-to-ligand charge transfer (MLCT) transition from the σ Fe−Fe to the σ* S−S orbitals, whereas the highest occupied molecular orbital (HOMO) of the Fe$_2$(CO)$_6$(μ-S$_2$) is dominantly Fe-Fe σ-bonding and the lowest unoccupied molecular orbital (LUMO) corresponds mainly to the S-S σ.[43–45] Additionally, it has been reported that in the absence of the S-S bond, the transition in Fe$_2$(μ-pdt)(CO)$_6$ is likely to become metal-to-metal charge transfer (MMCT) character and that the band at lower energies is primarily due to MLCT involving the Fe-Fe, Fe-S and Fe-CO bonds with some MMCT character; this idea was later confirmed by TD-DFT studies.[46,47]

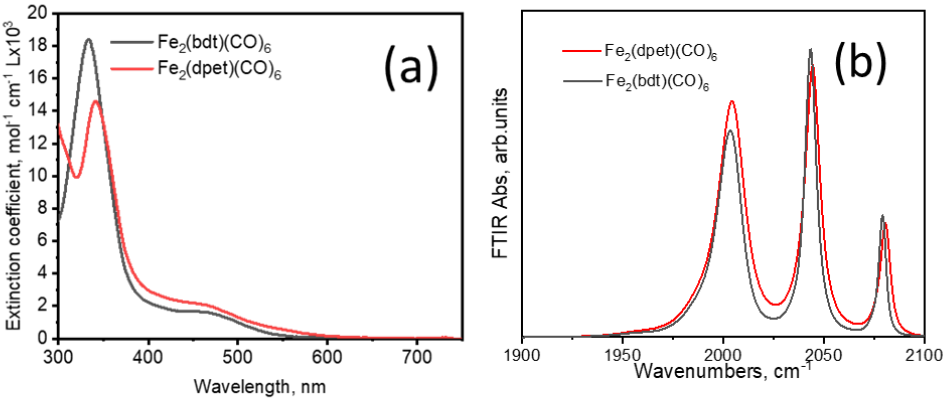

Figure 4. UV Vis (a) and Normalized FTIR (b) absorption spectra of **H1** Fe$_2$(bdt)(CO)$_6$ (black) and **H2** Fe$_2$(dpet)(CO)$_6$ (red) recorded in a 50 μM solution in acetonitrile at room temperature.

The FTIR spectra of **H1** and **H2** show characteristic bands that correspond to the CO group vibrations in the region 1900 to 2100 cm^{-1} (Figure 4). The spectra of **H1** and **H2** are very similar; a small shift to higher frequencies for ν(CO) in **H2** this is due to a slight change in electron density on the Fe-centres upon replacement of the benzene with the -C=C- backbone. A decrease in electron density reduces back-donation from the iron atom to the antibonding π* orbitals of the CO ligands, increasing the frequency of the ν(CO).

Photostability

The photostability of **H2** and **H1** as comparison were monitored by UV-Vis spectroscopy in DCM and MeCN under 405 nm irradiation at 1 mW/cm^2, an equivalent to one Sun. For the complexes **H1** in both solvents and **H2** in MecN, there was a noticeable reduction of the band at 333 nm within the first 5 min of irradiation, this band corresponds to the Fe-CO transitions, which means the molecule starts losing their -CO. At the same time new bands centred around 460 nm and 700 nm appeared and grow in intensity until ca. 90 min of irradiation. These bands later decay due to photoproduct decomposition. The new absorption band (at ca. 700 nm) is attributed to the formation of a photo-reduced species $[Fe_2(dpet)(CO)_6]^{2-}$, an assignment also supported by the DFT analysis (see below) and agrees with the previously reported observations for **H1 (**Figure 5**).**[14]

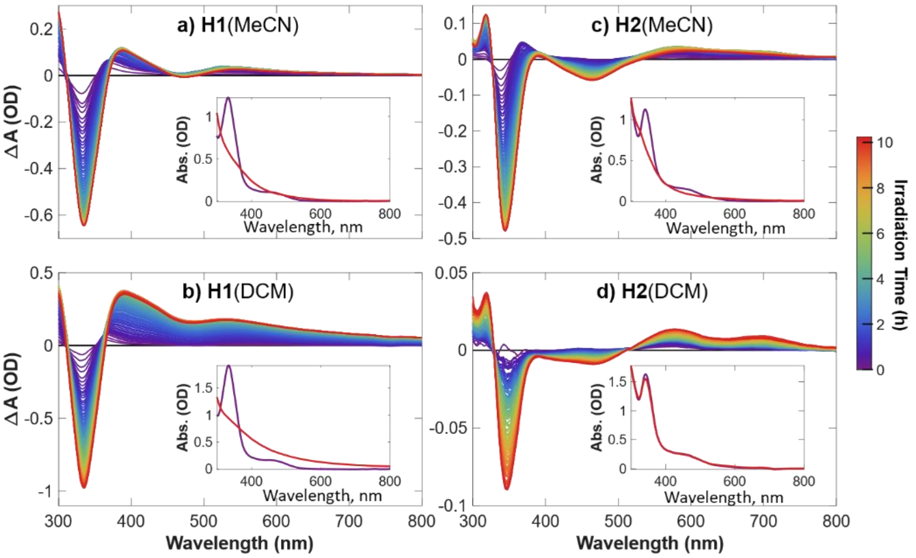

Figure 5. UV Vis absorption spectra as a function of irradiation time of a 0.1 mM solution of $Fe_2(bdt)(CO)_6$ (**H1**) and $Fe_2(dpet)(CO)_6$ (**H2**) in different solvents MeCN (a)(c) and DCM (b)(d), respectively. Both irradiated under 405 nm light at 1mW/cm^2 over 120 min.

Figure 6, shows the degradation kinetics of each sample whereas we can observe that **H2** in DCM is far more stable in comparison to the other samples with a degradation rate constant higher than 10 h^{-1}.

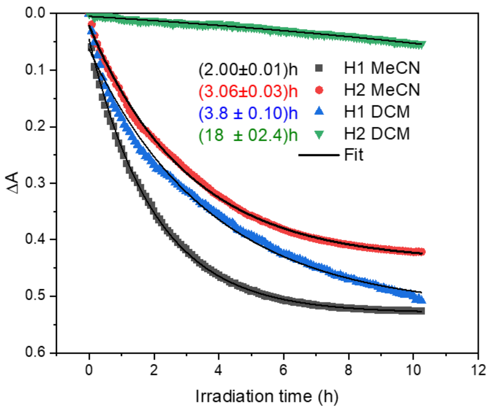

Figure 6. Photodegradation Kinetics of FeFe hydrogenase mimic complexes **H1** and **H2** in DCM and MeCN under 405 nm at 1 mW/cm^2 irradiation for 12 hrs.

Electrochemical characterization

The cyclic voltammograms for the solutions of complexes **H2** and **H1** in acetonitrile show a reversible two-electron reduction process with half wave potentials of $E_{1/2}$ = -1.21V for **H2** and $E_{1/2}$= –1.32 V for **H1** vs Fc+/Fc^0 (Figure 7). The obtained $E_{1/2}$ value for **H1** agrees with the previously reported value for this complex.[48] The 1st reduction process in both complexes is electrochemically reversible (as evident from a linear dependence of the peak current vs. $v^{1/2}$, according to the Randels-Sevcik equation and corresponds to a two-electron reduction process (Figure 8).[49]

$$i_p = (2.96 \times 10^5)\, n^{3/2}\, A_{electrode}\, C \sqrt{D\, v}$$

Eq. 1. Randles–Sevcik Equation. $A_{electrode}$ is the electrode surface area (cm^2), C is the concentration of the species (mol/cm^3), n is the number of electrons transferred during the reaction, D is the diffusion coefficient (cm^2/s) and ν is the scan rate (V/s).

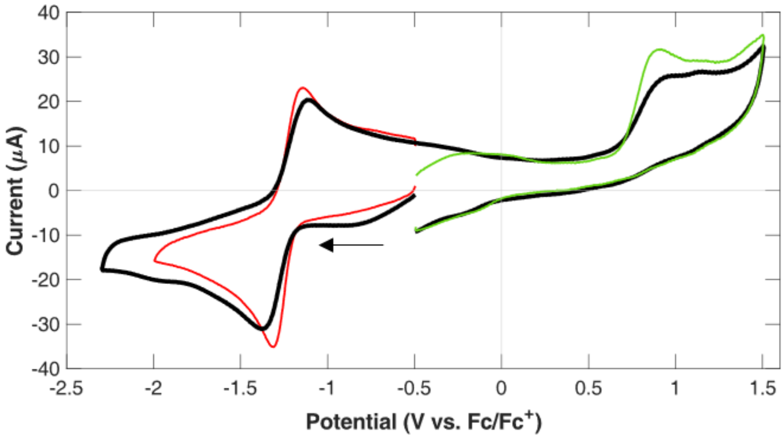

Figure 7. Cyclic voltammogram of 1mM solution of **H2** in 0.1 M of $[^nBu_4N][PF_6]$ supporting electrolyte solution in dry acetonitrile at a scan rate of 100 mV s^{-1} under N_2 atmosphere against Ag/AgCl. The values are reported against the (Fc^+/Fc^0).

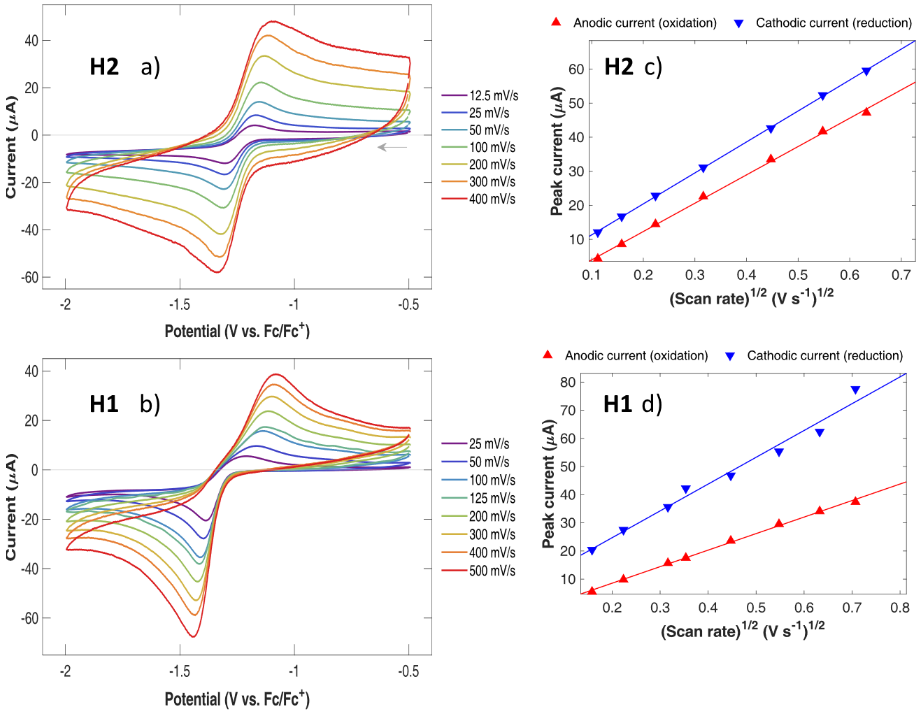

Figure 8. Scan Rate analysis from 10 to 200 mV s^{-1} of 1mM solution of **H2** and **H1** in 0.1 M nBu_4NPF_6 supporting electrolyte solution in dry acetonitrile recorded against Ag/AgCl electrode under N_2 atmosphere and their corresponding Randles–Sevcik plot for each sample.

Current Enhancement in the presence of proton source

To evaluate in the potential of **H2** as a possible proton reduction agent,[50] cyclic voltammograms of 1 mM of **H2** in acetonitrile were recorded in the presence of trifluoroacetic acid (TFA) in a range 2 mM to 80 mM to a 1 mM hydrogenase solution in acetonitrile. For **H1**, Figure 9 (left) demonstrates an increase in the reduction peak current with an increase of the acid concentration, which can be indicative of that the species formed upon 1st reduction of **H1** are able to catalyse proton reduction.

Complex **H2, behaves differently to H1:** Figure 9 (right) demonstrates that upon addition of a strong acid, TFA, a band appears around -2.3 V and shift to negative values with the increase in the TFA concentration.

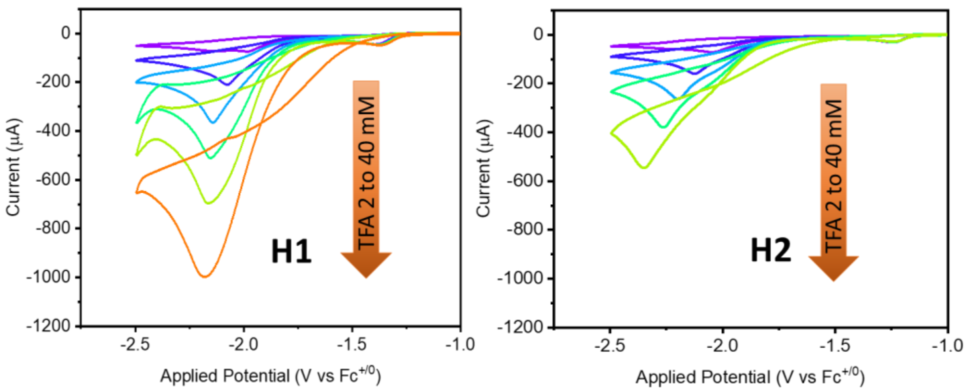

Figure 9. Cyclic voltammetry of the current enhancement analysis **H1** (left) and **H2** (right) hydrogenases increasing concentration of TFA (2 mM to 80 mM) in 0.1 M of nBu_4NPF_6 in dry acetonitrile at a scan rate of 100 mV s^{-1} under N_2 atmosphere against Ag/AgCl.

Both reduction processes showed a linear increase in the current with the addition of TFA this increment in the current suggested that both of them represented catalytic waves for proton reduction.[50,51] form the CV obtained data at 100 mV s^{-1} and the current enhancement we can obtained the catalytic current generated and the calculated TOF for both hydrogenases form the current ratio $TOF = {}^{i_{cat}}/_{i_p}$, obtaining values of $3.3x10^4 s^{-1}$ for H1 and $1.8x10^4$ s^{-1} for H2 with the addition of 40 mM of TFA. This results confirms that **H1** has much more proton reduction capability than **H2** under this conditions.

FTIR (Spectro)electrochemistry

To elucidate the changes in the structure in response to the reduction, the [Fe-Fe] complexes were analysed by IR Spectro-electrochemistry. Upon reduction of **H1**, the three absorption bands at 2080, 2043 and 2004 cm^{-1} corresponding to the carbonyl stretching vibration in the $Fe_2(bdt)(CO)_6$, decrease in intensity, whilst new bands, at lower energies (1964, 1913 and 1862 cm^{-1}) appear (Figure 10). Such behaviour reflects a decrease in the strength of CO bond due to the reduction of one of the iron agrees with previously reported studies for other [Fe-Fe] complexes. [42]

These signals that's appeared at lower energies have been assigned to the doubled reduced specie $[Fe_2(bdt)(CO)_6]^{2-}$, based on similar results previously reported with a slightly shift on the singlas.[14] An additional signal that appears transiently at 1680 cm^{-1} that according with literature clearly indicates a bridging CO at 1682 cm^{-1} leading to the theory of the 1e$^-$ reduced species formation.[14] After completion of the redox cycle, and re-oxidation of the reduced species back to Fe^{0}Fe^0, the IR-spectrum restored almost its original shape, indicating that the redox couple is partially reversible (Figure 10).

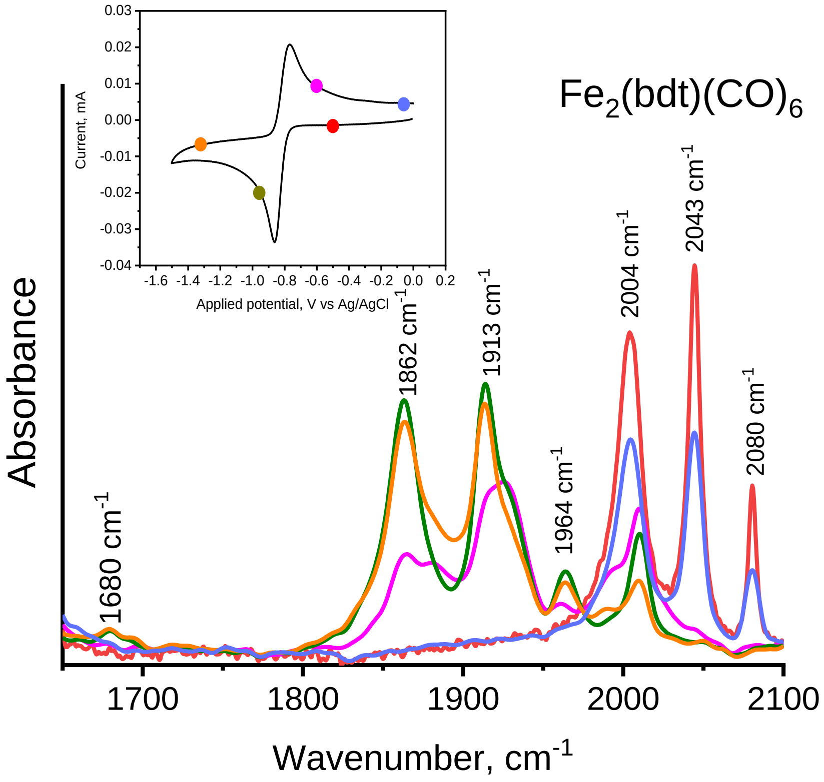

Figure 10. IR spectra of hydrogenase and Cyclic voltammetry (left up) recorded at 0.1 Vs^{-1} of **H1** $Fe_2(bdt)(CO_6)$ in a 0.5 M $[^nBu_4N][PF_6]$ solution in dry MeCN.

Figure 11 shows the changes on the IR spectra for the **H2** complex where three carbonyl stretching vibration peaks were found at 2080, 2043 and 2003 cm^{-1} on the steady state FTIR that corresponds to the carbonyl stretching vibrations of the $Fe_2(dpet)(CO)_6$ complex, similarly to **H1**.

Additionally, the association of the three peaks at lower energies (1860, 1909 and 1960 cm^{-1}) to the generation of two electron reduced species has been reported before in the formation of super-reduced species.[52] Mirmohades and Pullen, reported the study of 1e- reduction species triggered by laser flash-quenching methods and FTIR and TRIR, confirming the direct observation of $[Fe_2(bdt)(CO)_6]^-$ and its protonation product $[Fe_2(bdt)(CO)_6H]$.

They also reported the UV-VIS absorbance spectra of the single reduces specie $[Fe_2(bdt)(CO)_6]^-$ with a band that appearing at 500 nm after illumination steady-state, suggesting that overall there is a formation of 2e$^-$ reduced species by disproportionation of $[Fe_2(bdt)(CO)_6]^-$ is hence kinetically disfavoured relative to the faster recombination reaction and in particularly will not be able to compete with the pseudo-first order kinetics of protonation of $[Fe_2(bdt)(CO)_6]^-$ leading to the observation only of the 2e$^-$ reduces species. [14,53] their FTIR spectra suggest the formation of a mixture of double and single reduced species $[Fe_2(bdt)(CO)_6]^-$ /$[Fe_2(bdt)(CO)_6]^{2-}$ with bands appearing at 1890, 1980 and 2035 cm^{-1}. This bands seems to appear in a very low intensity in the analysis performed in this work. unfortunately, these theory can be only suggested in accordance with literature but in the SEC analysis performed in this work is only observable the presence of the double reduced species.

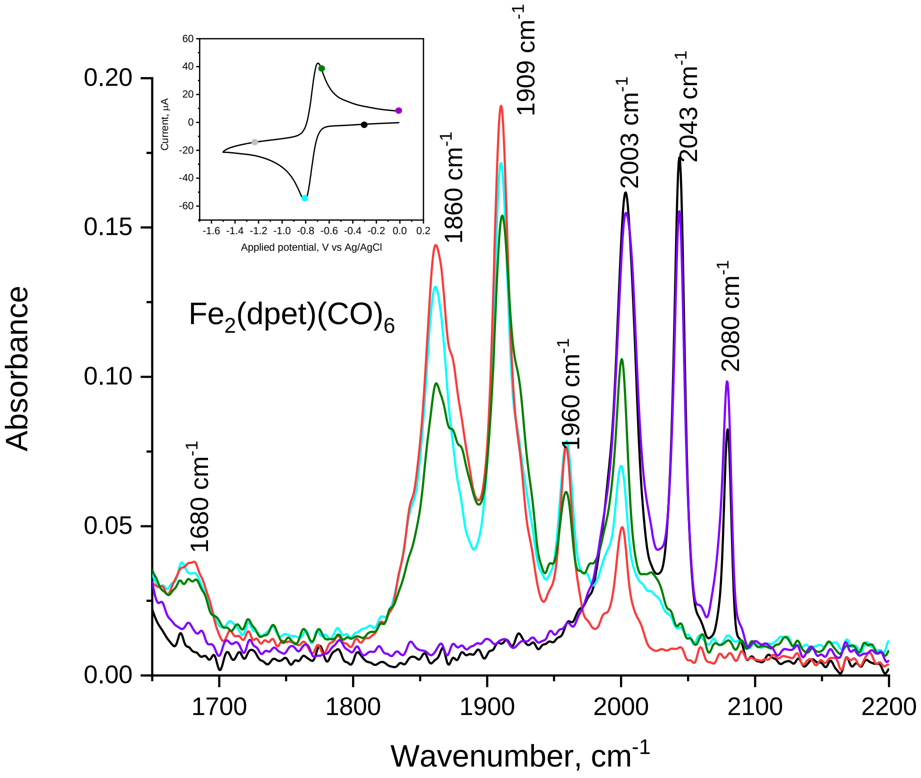

Figure 11. IR spectra and Cyclic voltammetry recorded at 0.01 Vs^{-1} of **H2** $Fe_2(dpet)(CO_6)$ in a 0.5 M $[^nBu_4N][PF_6]$ in dry acetonitrile solution obtained at different potentials as indicated in the CV (right side).

Nevertheless, the obtained results from the SEC analysis can be supported by the DFT calculations as we can observe in Figure *12* the IR spectra of the different redox species, we found same signals in the calculated spectra for the different mono and doubled reduced species.

With the aid of DFT calculations, we propose the mechanism for reduction processes in **H2**. According with the work done by Pullen et, al,[24,54] whereas it is suggested that the first reduction leads to a distortion of the molecule due to the reduction of one of the Fe-atoms in the "H-cluster" accompanied by reduction in FeFe bond order, and elongation of the FeFe, Fe-S distances for the reduced Fe-atom. The second reduction leads to breaking of the Fe-Fe bond, and the rearrangement of one of the -CO ligands into a bridging CO moiety between the two irons (Figure 13). The calculated values and the experimental ones are similar this can confirm our findings observed in the SEC experiments (Table 1).

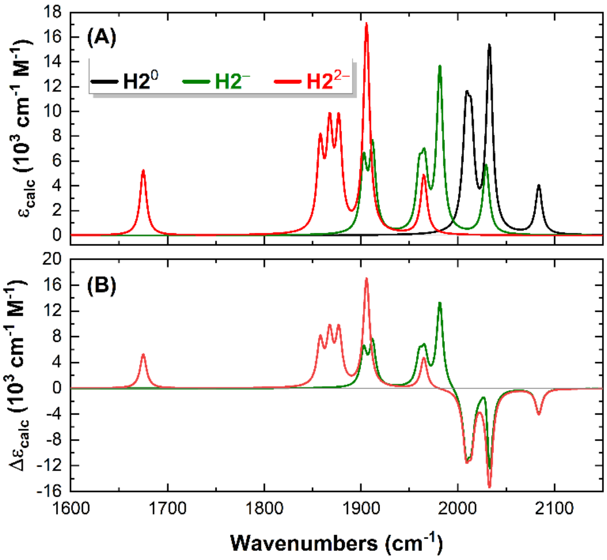

Figure 12. DFT calculated absolute (A) and difference (B) IR spectra of the different redox species associated with the reduction of complex **H2** in MeCN. Frequencies were scaled by 0.973 to better match the experimental values.

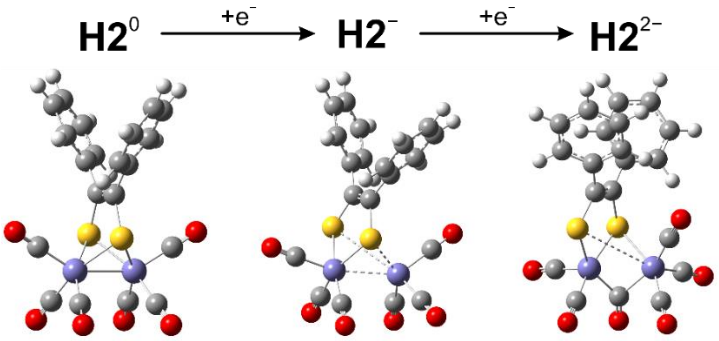

Figure 13. Optimised structures of the sequentially reduced states of complex **H2**.

Table 1. IR spectroscopic data for $Fe_2(dpet)(CO)_6$ and its reduced species, experimental and DFT values (in MeCN).

Compound	$\boldsymbol{\upsilon_{\mathrm{EXP}}(C \equiv O)}$	$\boldsymbol{\upsilon_{\mathrm{DFT}}(C \equiv O)}$
$Fe_2(dpet)(CO)_6$	2080,2043,2003	2084,2032,2010
$[Fe_2(dpet)(CO)_6]^{1-}$	2027,1976,1915	2029,1981,1911
$[Fe_2(dpet)(CO)_6]^{2-}$	1960,1909,1860	1964,1905,1865

Transient absorption

The transient absorption spectra of the $Fe_2(dpet)(CO)_6$ have been recorded in MeCN and DCM using 400 nm excitation pulses in intervals of 0 to 1000 and 0 to 6000 ps after excitation (Figure 14 a and b). The spectra of both solvents present a broad and initially structureless band centered around 500 nm, that evolves into two broad and overlapping bands centered around 450 and 525 nm. Target analysis of the spectra was carried out with a sequential four-state model, where the fourth component was assumed to persist beyond timescale of both experiments ($\tau_4=\infty$). The analysis revealed the species-associated difference spectra (SAS) shown in figure (Figure 15 c and d). Obtained constants for both TA and TRIR in both solvents are summarized in Table 2.

Following the current literature on excited-excited state of this type of Fe-Fe mimic hydrogenase complexes,[7,19,31,55,56] [57]we believe that upon excitation with 400 nm we populate a high single state (S_n). After the initial event, spectroscopic signatures are observed that we assigned to the lowest ^{5}MLCT state (T_1). The relaxation/vibrational cooling process occurring on the singlet state or triplet manifolds remains unclear form this experimental results. Relaxation on DCM appears to be slower than in MECN. It is known that MeCN has faster dielectric relaxation time than DCM, in line with the fact that both τ_1 and τ_2 are larger in the latter. The largest change in the dynamics of H2 in between the two solvents corresponds to τ_3, which increases from ca.135 ps in MECN to ca.210 ps in DCM.

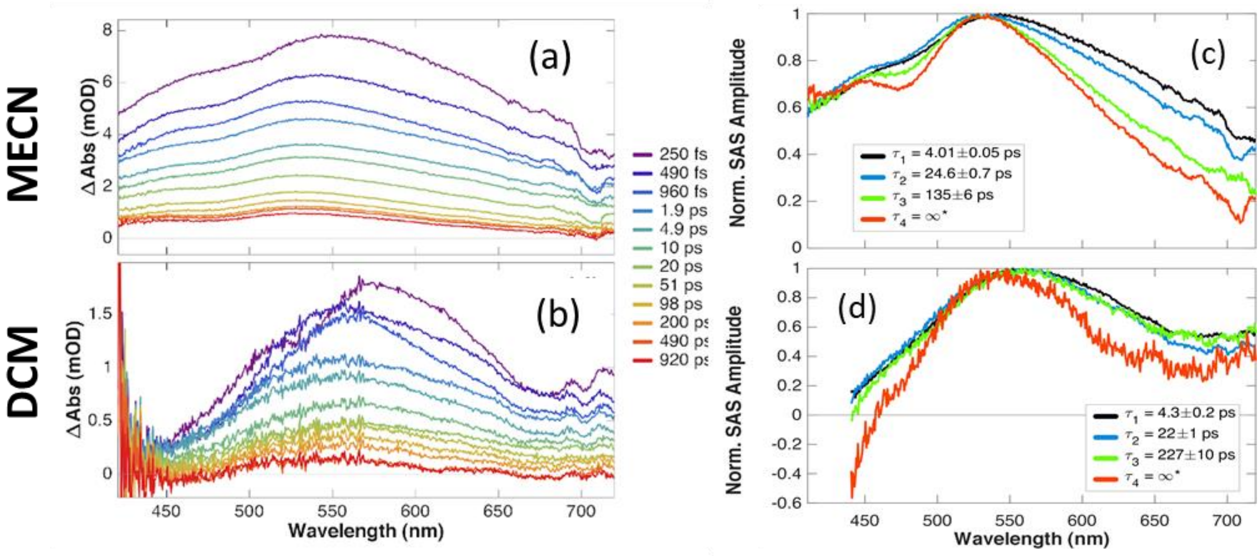

Figure 14. Transient absorption spectra of $Fe_2(dpet)(CO)_6$ recorded after excitation with 400 nm light between 0 and 1000 ps in two solvents dichloromethane (a) and acetonitrile (b). Normalised species-associated spectra derived from target analysis datasets for H2 in MeCN (c) and DCM (d). All data was fitted t≥1 ps, step IRF, sequential 4-state model (p0=GA).

Time resolved infrared spectroscopy (TRIR)

TRIR experiments were performed on $Fe_2(dpet)(CO)_6$ in two different solvents, DCM and MeCN using 400 nm, 40 fs excitation with the IR probe light centered at the carbonyl region near 2000 cm^{-1}.

The processed data from the $Fe_2(dpet)(CO)_6$ recorded in acetonitrile is shown in Figure 15. Three strong bleaches (negative bands) at 207, 2041 and 2004 cm^{-1} associated with the ground state carbonyl stretching vibrations are observed immediately after excitation. Four broad transient absorption bands (positive signals) were detected at 2068, 2027, 1985 and 1955 cm^{-1}. The first three absorption bands are shifted to lower energies relative to the bleach signals by 5 - 20 cm^{-1}. This decrease in vibrational frequency upon excitation indicates the C≡O bonds are weaker. Therefore, the Fe-C d-π* back-bonding interaction is stronger, and the electron density on the Fe centre was increased. From 10 – 50 ps, the transient absorption bands shift to higher frequency, which was associated with vibrational cooling of the excited state. An additional band was detected at 1955 cm^{-1} this band at lower energies is originated form new absorptions by photoexcitation.[7] Target analysis of the spectra was carried out with a sequential four-state model, the obtained time constants are summarized in Table 2.

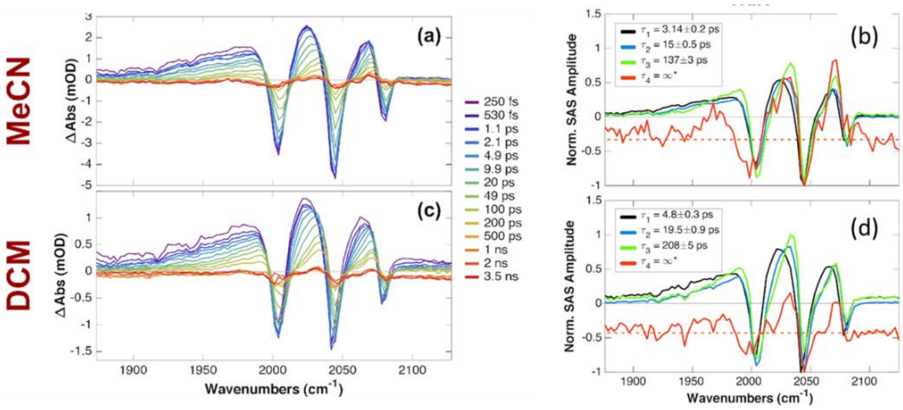

Figure 15. TRIR spectra of Fe2(dpet)CO)6 in DCM (a) and MeCN (c) recorded from 1800 to 2200 cm-1 at following 400 nm excitation and their corresponding SAS (b) and (d), respectively for each solvent. The kinetic traces at selected positions are shown. The solid lines in (b) and (c) t≥0.3 ps, step IRF, sequential 4-state model (p0=GA).

Table 2. Time constants obtained from the TA and TRIR analysis using a sequential four-state model.

Solvent	Components, ps	TRIR	TA
MeCN	τ_1	3.1±0.2	4.01±0.05
	τ_2	15±0.5	24.6±0.7
	τ_3	137±3	135±6
DCM	τ_1	4.8±0.3	4.3±0.2
	τ_2	19.5±0.9	23±1
	τ_3	208±5	227±10

3.5 Conclusions

In summary, this chapter has investigated the photophysical behaviour of a new FeFe hydrogenase mimic complex, $[Fe_2(dpet)(CO)_6]$ using a known compound,$[Fe_2(bdt)(CO)_6]$ as a comparison, by applying electrochemical and time-resolved spectroscopic techniques.

An inclusion of an additional aromatic ring in the new complex **H2** decreases its reduction potential relative to **H1** (making it less negative), making the complex easier to reduce and therefore more suitable for hydrogen evolution. The redox mechanism was proposed based on electrochemical data and supported by DFT calculations. Addition of proton source leads to an increase in current observed at the 1st reduction potential of **H2** and **H1**, suggesting that the complexes are suitable for proton reduction. Preliminary ultrafast transient absorption and infrared spectroscopy have been performed to evaluate the potential of **H2** for photocatalysis and understand the electron transfer processes happening in the “H cluster”. This study confirms the presence of 4 components both TA and TRIR, this lifetime constants are in perfectly agreement in both analysis, suggesting that the chosen model adequately describes the excited-state dynamics observed in these two experiments.

These observations are in line with the lower photostability exhibited by both complexes upon photoirradiation in MeCN versus the slower photobleaching observed in DCM. It is noteworthy that complex H2 degrades ca. 6 times slower than the parent complex (H1) in DCM, whilst the photobleaching kinetics are very similar in MeCN.

Altogether, these results illustrate that both the solvent and ligand environment play a crucial role in determining the (photo)stability of [FeFe]hydrogenase active site mimics. Introduction of the additional phenyl groups in the dpet ligand (vs. the model pdt ligand) allows for better stabilisation of the charge-transfer states (^{3}MLCT), also evidenced by the observed red shift in the UV-Vis absorption spectra. An explanation could be that the larger conjugated system in H2 can thus accommodate more electron density that would otherwise be injected into the d-sigma* orbitals that facilitate CO loss.

3.6 References

1 D. Streich, Y. Astuti, M. Orlandi, L. Schwartz, R. Lomoth, L. Hammarström and S. Ott, *Chem. - A Eur. J.*, 2010, **16**, 60–63.

2 Y. Tachibana, L. Vayssieres and J. R. Durrant, *Nat. Photonics*, 2012, **6**, 511–518.

3 S. Gao, W. Fan, Y. Liu, D. Jiang and Q. Duan, *Int. J. Hydrogen Energy*, 2020, **45**, 4305–4327.

4 T. Nann, S. K. Ibrahim, P. M. Woi, S. Xu, J. Ziegler and C. J. Pickett, *Angew. Chemie - Int. Ed.*, 2010, **49**, 1574–1577.

5 M. Frey, 2002, ChemBioChem, (2002),3, 153–160.

6 T. R. Simmons, G. Berggren, M. Bacchi, M. Fontecave and V. Artero, *Coord. Chem. Rev.*, 2014, **270**–**271**, 127–150.

7 P. W. J. M. Frederix, K. Adamczyk, J. A. Wright, T. Tuttle, R. V. Ulijn, C. J. Pickett and N. T. Hunt, *Organometallics*, 2014, **33**, 5888–5896.

8 N. Sekar and R. P. Ramasamy, *J. Photochem. Photobiol. C Photochem. Rev.*, 2015, **22**, 19–33.

9 OECD/IEA, *Glob. Energy CO2 Status Rep.*, 2018, 1–15.

10 G. National and H. Pillars, *Sustainable Development and Innovation in the Energy Sector*, .

11 R. E. Blankenship, *Plant Physiol.*, 2010, **154**, 434–438.

12 N. Nelson and C. F. Yocum, *Annu. Rev. Plant Biol.*, 2006, **57**, 521–565.

13 D. Bhattacharya, H. S. Yoon and J. D. Hackett, *BioEssays*, 2004, **26**, 50–60.

14 M. Mirmohades, S. Pullen, M. Stein, S. Maji, S. Ott, L. Hammarström and R. Lomoth, *J. Am. Chem. Soc.*, 2014, **136**, 17366–17369.

15 C. Bagyinka, *Int. J. Hydrogen Energy*, 2014, **39**, 18521–18532.

16 A. Meyers, E. J. Heilweil and C. J. Stromberg, *J. Phys. Chem. A*, 2021, **125**, 1413–1423.

17 W. Lubitz, H. Ogata, O. Rüdiger and E. Reijerse, *Chem. Rev.*, 2014, **114**, 4081–4148.

18 J. W. Peters, *Science (80-.).*, 1998, **282**, 1853–1858.

19 M. Sensi, C. Baffert, C. Greco, G. Caserta, C. Gauquelin, L. Saujet, M. Fontecave, S. Roy, V. Artero, P. Soucaille, I. Meynial-Salles, H. Bottin, L. De Gioia, V. Fourmond, C. Léger and L. Bertini, *J. Am. Chem. Soc.*, 2016, **138**, 13612–13618.

20 W. Thornley, S. A. Wirick, M. Riedel-Topper, N. J. Deyonker, T. E. Bitterwolf, C. J. Stromberg and E. J. Heilweil, *J. Phys. Chem. B*, 2019, **123**, 7137–7148.

21 Ö. F. Erdem, L. Schwartz, M. Stein, A. Silakov, S. Kaur-Ghumaan, P. Huang, S. Ott, E. J. Reijerse and W. Lubitz, *Angew. Chemie - Int. Ed.*, 2011, **50**, 1439–1443.

22 E. R. and W. L. Alexey Silakov,* Brian Wenk, *Phys. Chem. Chem. Phys.*, 2009, **11**, 6553–6554.

23 G. Berggren, A. Adamska, C. Lambertz, T. R. Simmons, J. Esselborn, M. Atta, S. Gambarelli, J. M. Mouesca, E. Reijerse, W. Lubitz, T. Happe, V. Artero and M. Fontecave, *Nature*, 2013, **499**, 66–69.

24 A. Adamska-Venkatesh, D. Krawietz, J. Siebel, K. Weber, T. Happe, E. Reijerse

and W. Lubitz, *J. Am. Chem. Soc.*, 2014, **136**, 11339–11346.

25 A. Silakov, C. Kamp, E. Reijerse, T. Happe and W. Lubitz, *Biochemistry*, 2009, **48**, 7780–7786.

26 J. A. Birrell, O. Rüdiger, E. J. Reijerse and W. Lubitz, *Joule*, 2017, **1**, 61–76.

27 C. Sommer, A. Adamska-Venkatesh, K. Pawlak, J. A. Birrell, O. Rüdiger, E. J. Reijerse and W. Lubitz, *J. Am. Chem. Soc.*, 2017, **139**, 1440–1443.

28 E. J. Reijerse, C. C. Pham, V. Pelmenschikov, R. Gilbert-Wilson, A. Adamska-Venkatesh, J. F. Siebel, L. B. Gee, Y. Yoda, K. Tamasaku, W. Lubitz, T. B. Rauchfuss and S. P. Cramer, *J. Am. Chem. Soc.*, 2017, **139**, 4306–4309.

29 H. Adams, M. J. Morris, C. C. Robertson and H. C. I. Tunnicliffe, *Organometallics*, 2019, **38**, 665–676.

30 R. C. Puthenkalathil, M. Etinski and B. Ensing, *Phys. Chem. Chem. Phys.*, 2020, **22**, 10447–10454.

31 J. L. Bingaman, C. L. Kohnhorst, G. A. Van Meter, B. A. McElroy, E. A. Rakowski, B. W. Caplins, T. A. Gutowski, C. J. Stromberg, C. E. Webster and E. J. Heilweil, *J. Phys. Chem. A*, 2012, **116**, 7261–7271.

32 J. F. Capon, F. Gloaguen, P. Schollhammer and J. Talarmin, *Coord. Chem. Rev.*, 2005, **249**, 1664–1676.

33 M. Mirmohades, Uppsala Universitet, 2016.

34 J. Amaro-Gahete, M. V. Pavliuk, H. Tian, D. Esquivel, F. J. Romero-Salguero and S. Ott, *Coord. Chem. Rev.*, 2021, **448**, 214172.

35 X. Li, M. Wang, L. Chen, X. Wang, J. Dong and L. Sun, *ChemSusChem*, 2012, **5**, 913–919.

36 L. Schwartz, P. S. Singh, L. Eriksson, R. Lomoth and S. Ott, *Comptes Rendus Chim.*, 2008, **11**, 875–889.

37 S. Kaziannis, S. Santabarbara, J. A. Wright, G. M. Greetham, M. Towrie, A. W. Parker, C. J. Pickett and N. T. Hunt, *J. Phys. Chem. B*, 2010, **114**, 15370–15379.

38 L. Cletheroe, University of Sheffield, 2017.

39 S. R. Domingos, H. Luyten, F. Van Anrooij, H. J. Sanders, B. H. Bakker, W. J. Buma, F. Hartl and S. Woutersen, *Rev. Sci. Instrum.*, 2013, **84**, 2–6.

40 M. J. Frisch, G. W. Trucks, H. B. Schlegel, G. E. Scuseria, M. A. Robb, J. R. Cheeseman, G. Scalmani, V. Barone, G. A. Petersson, H. Nakatsuji, X. Li, M. Caricato, A. V. Marenich, J. Bloino, B. G. Janesko, R. Gomperts, B. Mennucci, H. P. Hratchian, J. V. Ortiz, A. F. Izmaylov, J. L. Sonnenberg, D. Williams-Young, F. Ding, F. Lipparini, F. Egidi, J. Goings, B. Peng, A. Petrone, T. Henderson, D. Ranasinghe, V. G. Zakrzewski, J. Gao, N. Rega, G. Zheng, W. Liang, M. Hada, M. Ehara, K. Toyota, R. Fukuda, J. Hasegawa, M. Ishida, T. Nakajima, Y. Honda, O. Kitao, H. Nakai, T. Vreven, K. Throssell, J. Montgomery, J. A., J. E. Peralta, F. Ogliaro, M. J. Bearpark, J. J. Heyd, E. N. Brothers, K. N. Kudin, V. N. Staroverov, T. A. Keith, R. Kobayashi, J. Normand, K. Raghavachari, A. P. Rendell, J. C. Burant, S. S. Iyengar, J. Tomasi, M. Cossi, J. M. Millam, M. Klene, C. Adamo, R. Cammi, J. W. Ochterski, R. L. Martin, K. Morokuma, O. Farkas, J. B. Foresman and D. J. Fox, 2019.

41 T. Lu and F. Chen, *J. Comput. Chem.*, 2012, **33**, 580–592.

42 B. W. Caplins, J. P. Lomont, S. C. Nguyen and C. B. Harris, *J. Phys. Chem. A*, 2014, **118**, 11529–11540.

43 I. Silaghi-Dumitrescu, T. E. Bitterwolf and R. B. King, *J. Am. Chem. Soc.*, 2006,

128, 5342–5343.

44 D. L. Fay, *Angew. Chemie Int. Ed.*, 1967, **2**, 951–952.

45 J. P. H. Oudsen, B. Venderbosch, D. J. Martin, T. J. Korstanje, J. N. H. Reek and M. Tromp, *Phys. Chem. Chem. Phys.*, 2019, **21**, 14638–14645.

46 L. Bertini, C. Greco, P. Fantucci and L. De Gioia, *Int. J. Quantum Chem.*, 2014, **114**, 851–861.

47 F. Co, R. L. Dekock, E. J. Baerends and R. Hengelmolen, 1984, **2**, 289–292.

48 S. Pullen, Uppsala Universitet, 2017.

49 W. N. Cao, F. Wang, H. Y. Wang, B. Chen, K. Feng, C. H. Tung and L. Z. Wu, *Chem. Commun.*, 2012, **48**, 8081–8083.

50 S. Gao, Q. Liang, Q. Duan, D. Jiang and J. Zhao, *Int. J. Hydrogen Energy*, 2018, **43**, 7245–7256.

51 W. L. James Loke and W. Y. Fan, *Int. J. Hydrogen Energy*, 2020, **45**, 31976–31984.

52 A. Jablonskyte, J. A. Wright, S. A. Fairhurst, L. R. Webster and C. J. Pickett, *Angew. Chemie - Int. Ed.*, 2014, **53**, 10143–10146.

53 C. Orain, F. Quentel and F. Gloaguen, *ChemSusChem*, 2014, **7**, 638–643.

54 S. Wang, S. Pullen, V. Weippert, T. Liu, S. Ott, R. Lomoth and L. Hammarström, *Chem. - A Eur. J.*, 2019, **25**, 11135–11140.

55 B. W. Caplins, J. P. Lomont, S. C. Nguyen and C. B. Harris, *J. Phys. Chem. A*, 2014, **118**, 11529–11540.

56 P. A. Eckert and K. J. Kubarych, 2019, pp. 237–258.

57 F. Quentel, G. Passard and F. Gloaguen, *Chem. - A Eur. J.*, 2012, **18**, 13473–13479.

Chapter 4

Synthesis and characterization of Doped Aluminates for its application in Photoelectrochemical systems.

This chapter describes the synthesis and characterization of the aluminates $MgAl_2O_4$ doped with Cu and Ni in different ratios (0.1, 1 and 10%) as dopants, to evaluate their influence on the photophysical and photocatalytic properties for its application as support on sensitized photoanodes for photoelectrochemical (PEC) water splitting.

4.1 List of figures

4.2 Introduction

Nowadays, hydrogen has been recognized as one of the promising clean energy sources, with a high potential to substitute fossil fuels and address the environmental problems associated with the excessive use of those. Among many hydrogen production technologies proposed so far, photocatalytic water splitting represents a promising technology due to being a potentially effective and clean way to produce hydrogen.[1,2]

It would have been highly desirable to achieve water splitting by visible light. Naturally, this would require a compound absorbing light and then using its energy to split water. In 1972, the work published by Honda and Fujishima[3] reported the use of TiO_2 for water splitting under light. TiO_2 is an excellent candidate for water splitting application, due to its photoactive properties, low cost, and durability. However, it only absorbs on the UV region limiting its application. To find a catalyst that can be active in water splitting across the whole solar spectrum whilst maintaining low cost, durability, and the right energy levels for the task, a wide range of different semiconductor materials has been reported, with applications as photocatalysts in photocatalytic and photoelectrochemical (PEC) water splitting. For example, TiO_2, CdS, Ta_2O_5, $BiVO_4$, and many others have been reproted.[4]

The research reported here focusses on metal oxides as one of the promising materials for water splitting.

Spinel oxides including normal- and inverse- spinel-type semiconductors have been shown to have the potential to fulfil all the criteria needed for PEC applications. A normal spinel structure is denoted as AB_2O_4 where the divalent A^{II} ions fill the tetrahedral holes, and the trivalent B^{III} ions fill the octahedral holes in a close-packed arrangement of oxide ions (Figure 1).[5]

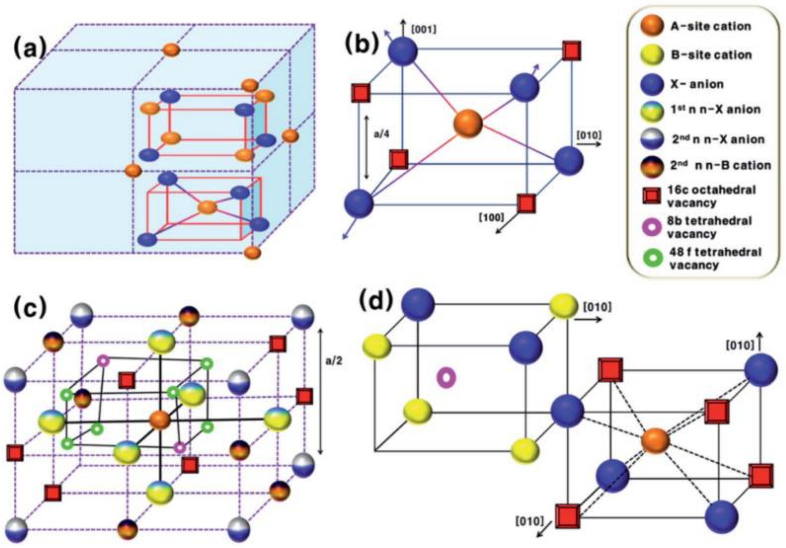

Figure 1. Schematic of the spinel-type semiconductors with a primitive tetragonal and cubic cells. The primitive cell contains two octants of the cubic unit cell. Atomic positions are exposed for the primitive unit cell only. Lattice arrangements and the nearest neighbours for (b) the tetrahedral A-site (8a), where the anion dilations are shown by solid a blue-coloured arrows. (c) The octahedral B-site (16d), and (d) the tetrahedral anion X-site. [5]

Spinel-type oxides has been proven to be good candidates for water splitting due to their photochemical stability, luminescent properties (which allows one to monitor the reaction), and cation/anion vacancies which allow for doping.[6,7] One example of this type are the aluminates, such as $MgAl_2O_4$, which showed a production rate of 120 μm $H_2{\cdot}g^{-1}$ after 2 h of reaction under 254 nm irradiation with an efficiency of 4%.[8–10]

However, almost all these aluminates absorb in the UV range, making them not suitable for application under solar light. Therefore, it is necessary to design semiconductor with a band gap (Eg) higher than 1.23 eV (the minimum energy required per electron in water oxidation) and lower than 3 eV to absorb in the visible range for its optimal use under solar light.[11] Lots of effort has been spent in the last decades to enhance the photocatalytic activity of aluminates, and make them active in visible range through different approaches including doping, surface modification, hetero-junctions and the use of molecular co-catalysts.[12,13]

The use of earth abundant metals such as Co, Ni and Cu as dopants in H_2-production has been widely studied. The addition of these metals on the semiconductors creates a Schottky barrier at the metal/semiconductor interface. This Schottky barrier is a type of junction that promotes the charge separation, retarding the recombination processes. Additionally, the earth abundant metals are able to catalyse the proton reduction, further enhancing the photocatalytic production of H_2. [2,14–161718–21]

This chapter presents the study of aluminates doped with copper and nickel for their application for photocatalytic water splitting. The addition of Cu and Ni as a dopants will modify the band-gap as well as the band position, and therefore their photophysical properties and photocatalytic performance.

4.3 Experimental methods

Synthesis

Doped aluminate powders were synthetized by sol-gel method using nitrates of Mg, Al and the dopants Cu and Ni in different ratios (0.1, 1 and 10%). [21–23]

$Mg(NO_3)_2$ (Alfa Aesar® 98%) and $Al(NO_3)_3$ (Alfa Aesar® 98%) were weighted and dissolved in Ethylene Glycol Monomethyl ether (EGME) (Acros Organics® 99%) with citric acid (Sigma-Aldrich ® 99%) and stochiometric amounts $Cu(NO_3)_2$ (Aldrich 99%) and $Ni(NO_3)_2$ (Aldrich 99%) respectively, was added to the solution and heated at 70°C until gel was formed; the gel was then dried at 120 °C for 24 hr. The obtained powder was grinded in a mortar and annealed at 1000 °C in a furnace overnight in air (Eq. 1).

$$Mg(NO_3)_2 + Al(NO_3)_3 + M(NO_3)_2 \rightarrow MgAl_2O_4{:}M + CO_2$$

M=Ni, Cu. Eq. 1

Characterization

The obtained powders of doped aluminates were analysed by various techniques. The crystallinity and phase composition of the samples was analysed by **X-Ray Diffraction (XRD)** in a Bruker D8 Advance instrument using Cu Kα radiation (λ=1.54 Å) to obtain the diffractograms. Crystal size was calculated using Scherrer equation (Eq.2). [24]

$$\Phi = \frac{K\lambda}{\beta \cos\theta} \qquad \text{Eq. 2}$$

Where Φ is the crystal size; K is the shape factor with a value of 1; λ is the wavelength of the X-rays used (λ=1.54 Å); β is the full width half-maximum (FWHM) of the main intensity peak and θ is the Bragg angle.

Optical density was measured in a Cary 5000 NIR-UV-Vis Spectrometer equipped with integrated sphere using diffuse reflectance. From the absorbance in F(R) data the energy band gap (Eg) values were obtained from Tauc's plots.

The oxidation states of the elements as well as the bonding interactions were analysed by **X-ray photoelectron spectroscopy (XPS)** using a Kratos Axis Supra X-ray photoelectron spectrometer. XPS spectra were obtained using a monochromate Al Kα X-ray source (186.6 eV). Survey spectra was acquired using a pass energy of 160 eV. High resolution core level spectra for elements were acquired using a pass energy of 20 eV. All the element spectra were charge referenced against the C1s peak at 284 eV to correct the charging effects during acquisition. The percentage of dopant in each sample was calculated from the core level spectra following the removal of a non-lineal (Tougaard) background.

Electrochemical Impedance Spectroscopy (EIS) was conducted using a potentiostat AUTOLAB PGSTAT302N at different potentials in a range of 100 kHz to 0.01 kHz. In a typical three- electrode electrochemical cell was used for all the samples used as working electrode, Ag/AgCl as reference electrode and Pt as counter electrode. 0.5 M Na_2SO_4 aqueous solution was used as electrolyte in all measurements; the system was deoxygenated by bubbling N_2 for 15 min before the experiments. The working electrode was prepared by incorporating the synthesized powders on copper tape substrate to determine the interfacial capacitance for each aluminate-electrolyte system.

Photocatalytic hydrogen evolution tests were performed in a 250 ml quartz reactor coupled to a gas chromatographic equipment. The samples of $MgAl_2O_4$ doped with Cu or Ni at 0.1, 1 and 10% were placed in the reactor in a 1:1 ratio (deionized water: sample), the suspension was bubbled with N_2 to avoid any presence of oxygen. The reaction started when the UV lamp was turned on, using a 254 nm irradiation during 180 min. This reaction was followed by gas chromatographic analysis of the head-space, by using GC containing a column with a TCD detector (Thermo Scientific 3GC

Ultra), pumping 5 ml of the sample every 30 min with a Watson-Marlow® peristatic pump model 101F (Figure 2).

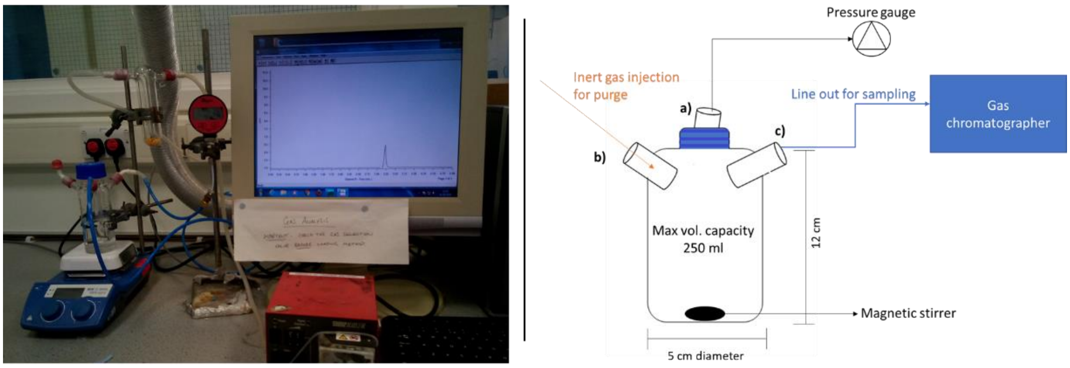

Figure 2. Photocatalytic system used for detecting H_2 (left side) and schematic representation for the reactor used for the H_2 evolution tests.

4.4 Results

X-Ray Diffraction analysis

Figure 3 shows the diffractograms for the aluminates $MgAl_2O_4$ doped with 0.1, 1 and 10% of copper. In the sample with 0.1% of copper, the Cu cannot be detected and only the $MgAl_2O_4$ phase is observed; according to the PDF card 010714914 we can identify a spinel type compound with a face centered cubic structure (FCC). In the sample with 1% copper, different phases are observed. One phase corresponds to the $MgAl_2O_4$, a second phase was identified as Corundum Al_2O_3 with rhombohedral structure that corresponds to the PDF 000431484.

Other diffraction peaks with low intensity were observed, the ones at 2θ values 62° and 42° can be assigned to the 220 and 113 planes, respectively. Both corresponds to the FCC structure of copper with the space group of Fm3m (JCPDS No. 85-1326), therefore, these peaks can be assigned to the formation of CuO and Cu_2O phases (Figure 3 inferior).[25,26]

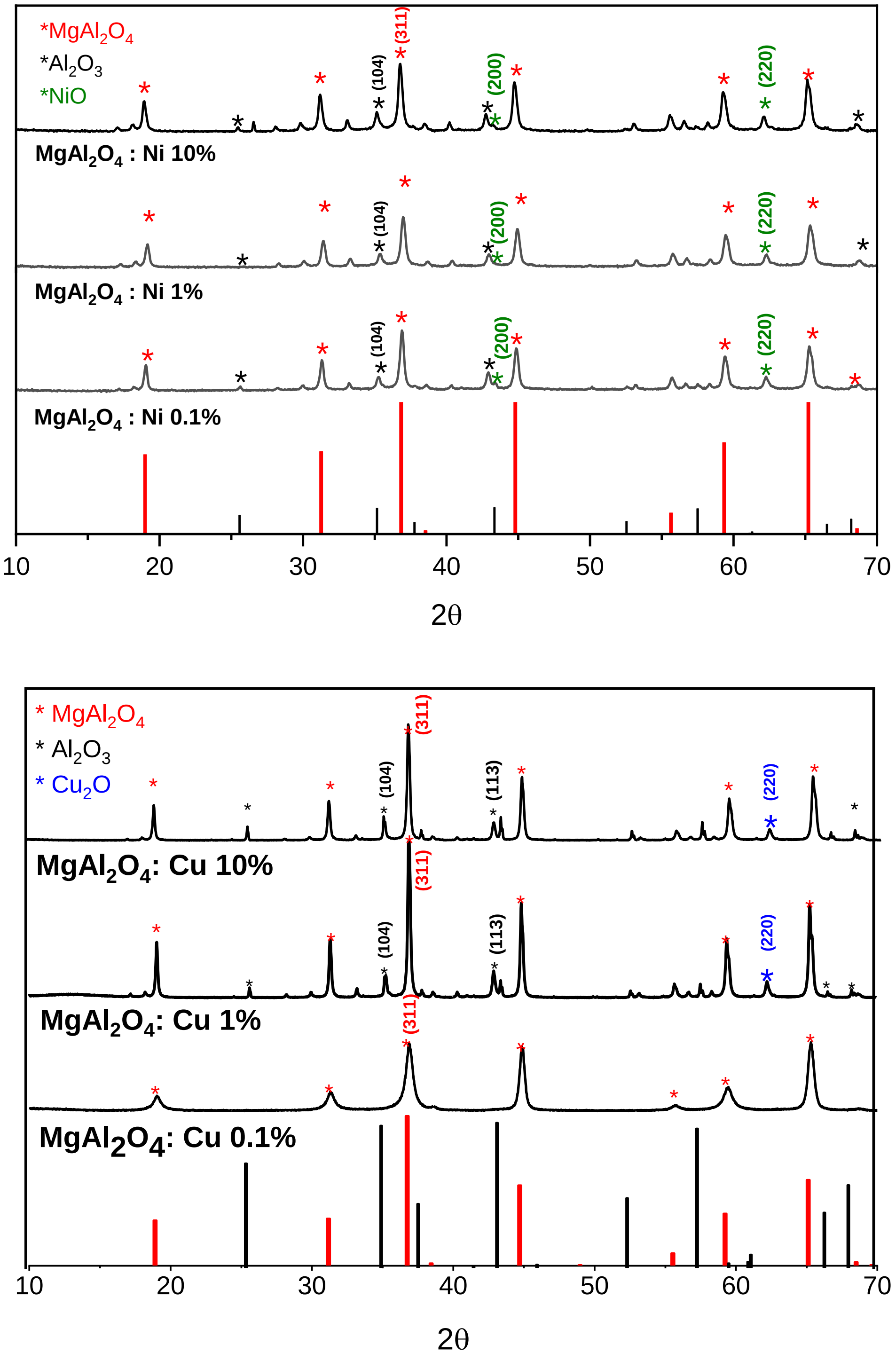

Figure 3. XRD pattern for $MgAl_2O_4$ doped with Cu (inferior) and Ni (superior) at different ratios (0.1, 1 and 10%) and the PDF patterns for $MgAl_2O_4$ and Al_2O_3 phases.

For the sample doped with Ni (Figure 3 superior) same diffraction peaks were observed, that corresponds to the formation of the $MgAl_2O_4$ and Al_2O_3. Additionally, other peaks appeared at 2θ values 62.8° and 43°, according with literature those corresponds to the formation of NiO with the FCC structure (JCPDS no. 075-0269).[27] The sample doped with 10% of Ni presented a different coloration (light greenish) that leads us to think in the formation of the nanocomposite NiO/$NiAl_2O_4$ as a second phase, as it has been reported in the literature and some of the characteristic diffraction peaks present in NiO/$NiAl_2O_4$ (JCPDS card No 01-1299 and No 10-0339) and NiO (JCPDS card No 22-1189) matches with the diffraction peaks and their corresponding planes, observed at 36.7 (311), 44.7 (400) and 65.3 (440) in the samples studied in this work. [28,29]

Another observation was the increase in the within of the peaks, this in the sample with 0.1% of dopant, this can suggest the incorporation of Ni into the crystal structure of the $MgAl_2O_4$ to corroborate this we calculate the particle size form the XRD data using Scherrer equation (Figure 3).[30]

The results show a decrease on crystal size for both samples, when the dopant amount was increased. Cu 0.1% crystal size was 33 nm and 25 nm as we increase the dopant amount to 1%. This supports the theory that the samples with 0.1% the metal (Cu or Ni) could be integrated inside the crystal structure, unfortunately to corroborate this in more detail we need to make another study with use of an internal standard to effectively calculated if the dopants are within the structure or just as a second phase study should be taken in account, unfortunately the lack of time and resources this couldn’t be done within the scope of this project.

$$FWHM(2\theta) = \frac{b\lambda}{Dcos\theta} \qquad \text{Eq. 2}$$

If we put in terms of 2θ, or in terms of Q,

$$D = \frac{b2\pi}{FWHM(Q)} \qquad \text{Eq. 3}$$

We selected the higher intensity peak for this calculations that in this case was the plane (311) the obtained values are summarized in Table 2.

Table 1. Crystal planes and peak positions (2θ) of the main peaks founded in the MgAl$_2$O$_4$ doped samples with Ni and Cu and the XRD patterns that correspond with the founded phases NiO and Cu$_2$O.

					MgAl$_2$O$_4$ Cu 10%				MgAl$_2$O$_4$ Ni 10%			
	h	*k*	*l*	*2θ*	*h*	*k*	*l*	*2θ*	*h*	*k*	*l*	*2θ*
MgAl$_2$O$_4$	3	1	1	36.83	3	1	1	36.95	3	1	1	36.77
JCPDS	4	0	0	44.79	4	0	0	44.86	4	0	0	44.72
010714914	4	4	0	65.21	4	4	0	65.28	4	4	0	65.27
	5	1	1	59.34	5	1	1	59.35	5	1	1	59.31
Al$_2$O$_3$	1	1	3	43.34	1	1	3	43.35	1	1	3	43.35
JCPDS	1	0	4	35.15	1	0	4	35.08	1	0	4	35.13
000431484	1	1	6	57.50	1	1	6	57.48				--
	0	1	2	25.57	0	1	2	25.49	0	1	2	25.54
NiO	1	1	1	37.20					1	1	1	37.78
JCPDS	2	0	0	43.20					2	0	0	43.29
04-0835	2	2	0	62.87					2	2	0	62.33
Cu$_2$O	1	1	0	29.60	1	1	0	29.997				
JCPDS	1	1	1	36.52	1	1	1	--				
05-0667	2	0	0	42.44	2	0	0	42.89				
	2	2	0	61.54	2	2	0	62.17				

UV Vis Absorption and Band Gap calculation

The absorbance spectra of the obtained MgAl$_2$O$_4$ doped Cu and Ni powders were measured in a Cary 5000 NIR-UV-Vis Spectrometer using a Diffuse Reflection accessory.

In Figure 4 the black line corresponding to the MgAl$_2$O$_4$ showed absorption from 200 to 350 nm. The samples doped with copper showed an absorption band from around 250 to 450 nm; this shift to the visible region is due to the copper doping, and an increase in the Cu wt% leads to the absorption bands shift further to lower energies, in the visible range. An additional large absorption band that appears between 600 nm to 800 nm is associated with the d-d transition of Cu^{2+}.[14]

In the samples doped with nickel (Figure 4)(dashed lines), the sample with 10% shows additional absorption bands in the interval from 200 to 300, 350 to 450 nm and 550 to 700 nm. According with literature the bands at 200-300 nm and 350-450 are due the electron transfer between metal (Mg in this case) and the oxygen anion, whilst the bands at 550-700 nm are related to the electronic transitions in the tetrahedrally coordinated Ni^{2+}. This confirms the formation of $NiAl_2O_4$ during the annealing process according with the literature.[29 18,31]

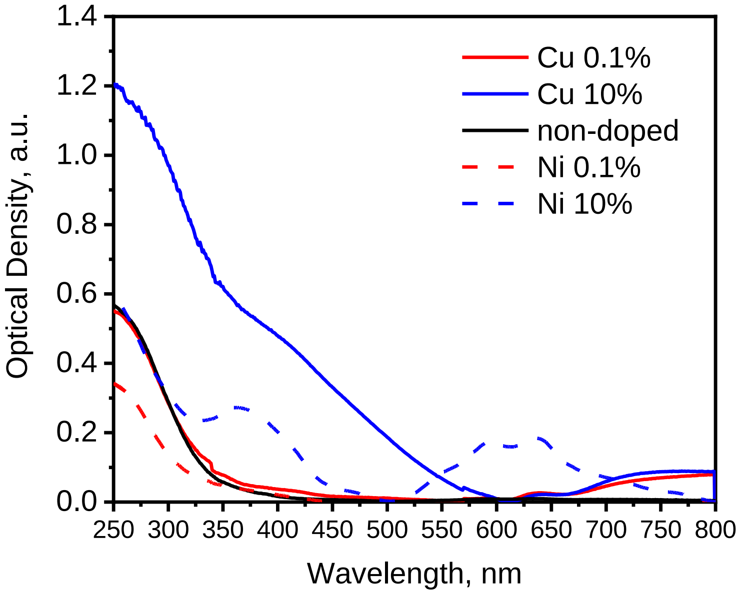

Figure 4. UV Vis absorbance spectra of $MgAl_2O_4$ doped with copper atomic wt% 0% (black), 0.1% (red), 10% (blue) and nickel (dash line).

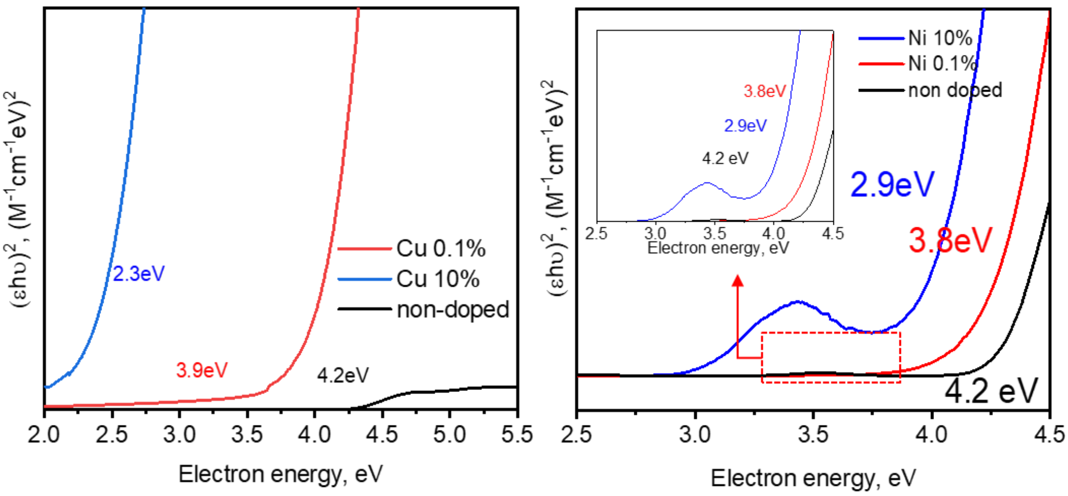

Figure 5. Determination of band gap by UV Vis spectroscopy using Tauc's equation of samples a) $MgAl_2O_4$ doped with Cu 0.1 (red line) and 10% (blue line) and b) $MgAl_2O_4$ doped with Nickel in 0.1 (red) and 10% (blue) wt.% and $MgAl_2O_4$ non-doped (black line).

The optical band gap energy values were determined from Tauc's plot (Figure 5), extrapolating the linear portion of $(\alpha h v)^2$ for the direct band gap versus the photon energy according with the Tauc's equation (Figure 4), where the dependence of the absorption coefficient k on the frequency v can be approximated as:

$$\alpha h v = A(hv - E_g)^{n/2} \qquad \text{Eq. 4}$$

Where α is the absorption coefficient, v is the incident light frequency, E_g band gap, h Planck's constant and A the constant.[32] The n depends on the type of transition and can have different values (2, 3, 1/2 and 1/3) corresponding to indirect allowed, indirect forbidden, direct allowed and direct forbidden transitions, respectively.[33]

The calculated values were 4.2 eV for non-doped $MgAl_2O_4$, 3.9 and 2.3 eV for $MgAl_2O_4$: Cu wt.% 1 and 10%, respectively. For $MgAl_2O_4$: Ni the values were 3.8, 2.9 eV for wt.% 0.1 and 10%, respectively. In the case of Ni 10% we can observe a second transition that extrapolates at 2.9 eV. The possible error range for the band gap is about ±0.10%. The error associated with these measured gaps is extracted from the linear regression used to fit the straight lines and from the data points within the straight line region of the data.[34,35]

Table 2. Particle size calculated by Scherer's equation for the plane (311) and Band gap values for doped and non-doped samples.

Sample		Crystal size, nm	Band Gap, eV
$MgAl_2O_4$ Non doped		16	4.2
$MgAl_2O_4$: Cu	0.1%	33	3.9
	10%	25	2.3
$MgAl_2O_4$: Ni	0.1%	22	3.8
	10%	23	2.9

X-Ray Photoelectron Spectroscopy

The XPS analysis was carried in a Kratos Ultra to analyse the composition of the samples and the oxidation state of Cu and Ni in each sample.

The survey spectra were acquired using a pass energy of 160 eV from $MgAl_2O_4$ powder samples mounted them into indium foil by pressing, doped with Cu in 0,1, 1 and 10% ratios and Ni in 0.1, 10% ratios were Mg 1s, O2 1s, Al 2p peaks are shown in Figure 6 a) and b), respectively. The peaks that correspond to Cu (932 eV) and Ni (855 eV) were only detected in the samples with 10% of dopant in a low intensity this is due to the detection limits of the equipment.

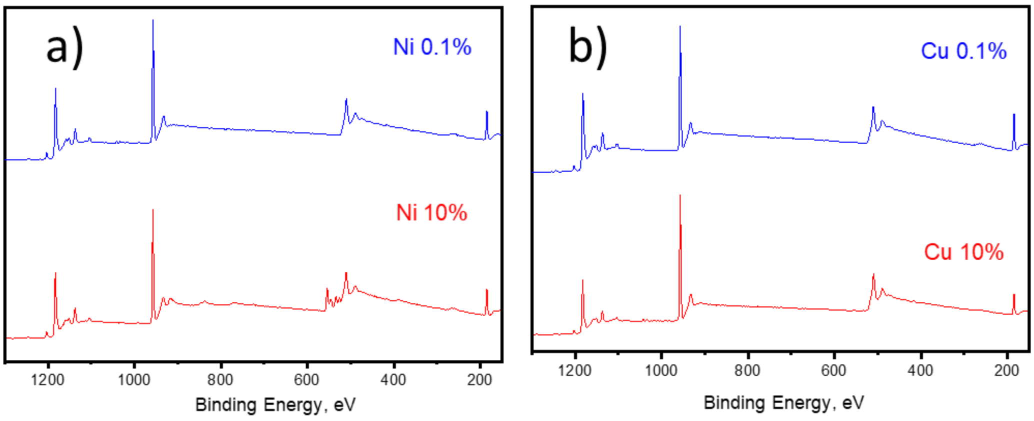

Figure 6. XPS Survey spectra for a) $MgAl_2O_4$ doped with Cu in 0.1, and 10% ratio; b) $MgAl_2O_4$ doped with Ni in 0,1 and 10% ratios.

The high resolution spectra for the $MgAl_2O_4$ doped with Cu 10% are shown in Figure 7, the core level spectra for Cu 2p (Figure 7**a**) shows two strong peaks at 932 and 952 eV, those correspond to the Cu $2p_{3/2}$and Cu 2p ½, characteristic peaks of Cu^{2+} state . Additionally, a peak appears at 943 eV this is ascribed to the multiple splitting form Cu^{2+} species, this suggest the presence of CuO.[16,36,37]. Figure 7b shows peaks at 73, 74 and 77 eV, those correspond to aluminium oxide, magnesium aluminates and a mixture of metallic aluminium and oxides, respectively. The peaks at 1303 eV and 130 eV correspond to the metallic Mg and $MgAl_2O_4$, as shown Figure 7b. The core level spectra for O 1s are shown in Figure 7c, were the peaks at 530 and 531 eV correspond to the metal oxides and aluminium oxides present in the sample.

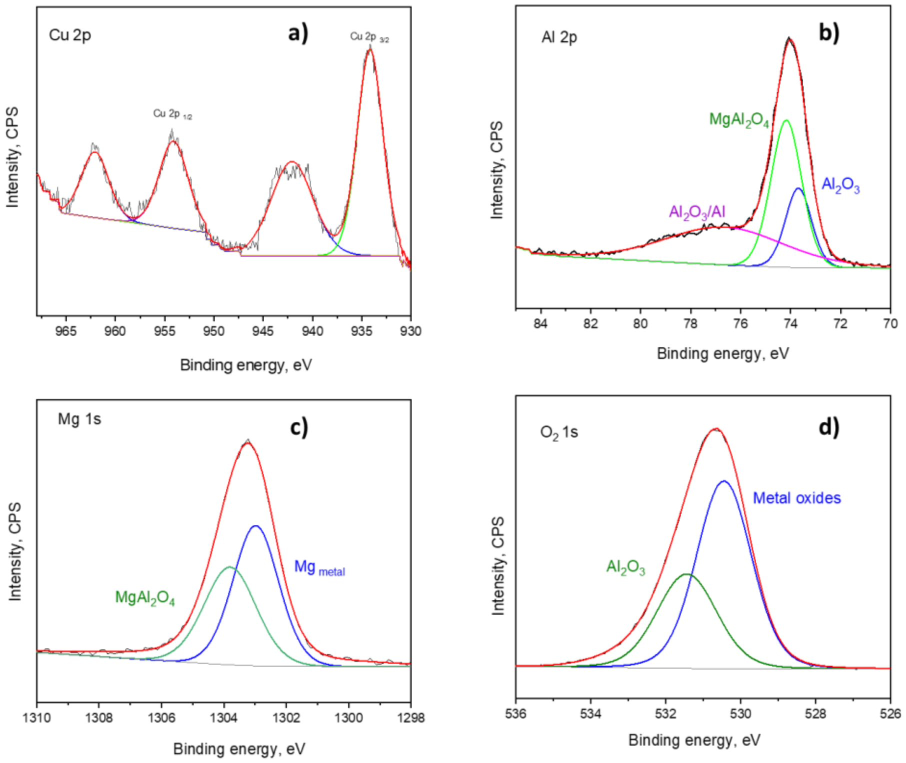

Figure 7. XPS high resolution spectra of $MgAl_2O_4$ Cu 10% sample. ***a)*** *Cu2p,* ***b)*** *A 2p,* ***c)*** *Mg 1s,* ***d)*** *O1s*

Figure 8 shows the peaks correspond to Mg 1s, Al 2p, O 1s and Ni 2p present in the $MgAl_2O_4$ doped with Ni 10% sample. The spectra of Ni 2p showed strong peaks at 854 860, 871 and 878 eV the peaks at 854 and 871 eV can be assigned to the Ni 2p 3/2 and Ni 2p ½ signals of the presence of Ni^{2+}, meanwhile the peaks at 860 and 878 eV correspond to the satellites.[38]

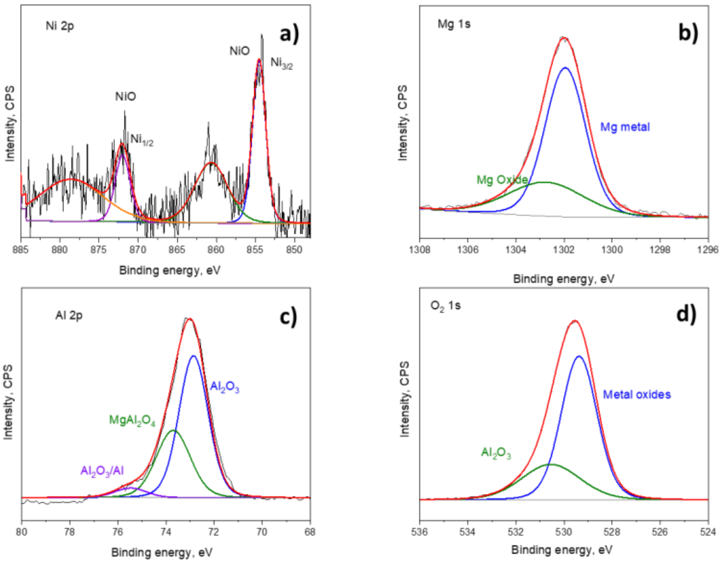

Figure 8. XPS high resolution spectra of $MgAl_2O_4$ Ni 10% sample. ***a)*** *N 2p,* ***b)*** *Mg1s* ***c)*** *A 2p,* ***d)*** *O1s*

Band structure position determination

The position of the bands was determined by Electrochemical Impedance Spectroscopy (EIS). There, we measured the resistivity for each material in a frequency range of 100 kHz to 0.01 kHz. From this data we obtained the Nyquist plots. From these plots, by using the Mott-Schottky equation we determined the flat band potential. Which is, the measurement of the differential capacity of the electronic double layer at the semiconductor/electrolyte interface. Where the total capacitance of the interfacial double layer $C_{Interface}$, principally this comprises the contribution from the semiconductor capacitance, C_{sc}, and the capacitance from the Helmholtz layer in the electrolyte, C_H, which are in series one of each other, following the equation:

$$\frac{1}{C_{Interface}} = \frac{1}{C_{SC}} + \frac{1}{C_H} \qquad \text{Eq. 5}$$

For a semiconductor, the Helmholtz capacitance is typically assigned values between 0.1 F m^{-2} and 0.2 F m^{-2}, assuming that this capacitance on the electrolyte side of interface is too large that it is negligible. Taking in consideration that C_{SC} is much shorter that C_H and that the potential over drop depletion layer, is bigger than the change in Helmholtz potential drop caused by the applied voltage. Assuming that these considerations are valid and for an n-type semiconductor, the donor density N_D and the flat band potential V_{fb} are then deduced from the experimental C^{-2} vs. V plots by using the Mott-Schottky relationship:

$$\frac{1}{C_{SC}^{2}} = \frac{2}{\varepsilon_0 \varepsilon_r e n}\left(U(RE) - U_{FB}(RE) - \frac{k_B T}{e}\right) \qquad \text{Eq. 6}$$

Where ε_0 represents the permittivity of free space, ε_r the relative permittivity of the semiconductor, e the electronic charge, n the concentration donors k_B the Boltzmann constant, T the temperature, U(RE) the electrode potential applied relative to a reference electrode, RE and U_{FB}(RE) the flat band potential, which will be referred to as U and U_{FB} henceforth.[39,40]

Let us consider the Nyquist plots for the samples doped with Ni and Cu in different ratios. In (Figure 9) we can observe the capacitance arc of each sample where the size corresponds to charge transfer resistance. The diameter size of the arc is related to the charge transfer resistance, and all sample showed different arc size, which means that the double-layer capacitance value depends on the metallic cation present in each sample. The samples doped with Cu shown a smaller capacitance values than the ones doped with Ni. The sample with Ni 0.1% is the one with the smaller arc size, therefore smaller resistivity to the electron transfer followed by the sample doped with Cu in a 10% ratio.

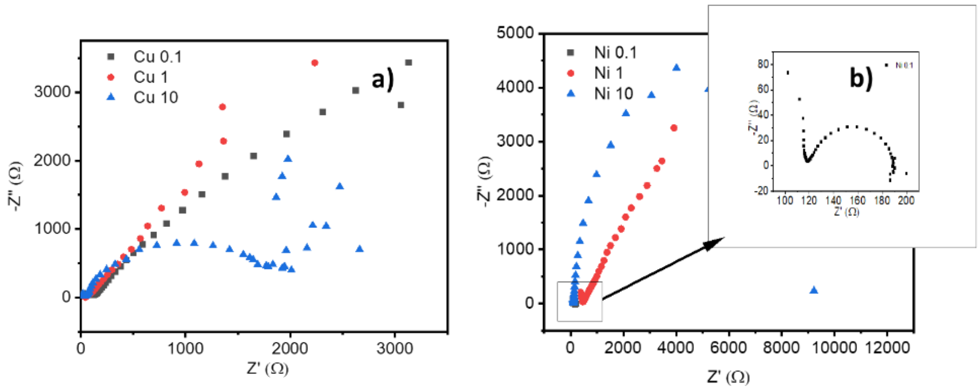

Figure 9. Nyquist plots for the $MgAl_2O_4$ doped with Cu (a) and Ni (b): 0.1 (black), 1 (red), 10% (blue), respectively for each samples.

Figure 10 shows the Mott Schottky plots constructed to determine the Fermi level which approximates to the band edge for the $MgAl_2O_4$ doped with Ni and Cu in different ratios: 0.1, 1 and 10%. In all cases a linear behaviour with a positive slope is observed, that indicates that the Fermi level is approximated to the conduction band which is characteristic of a n-type semiconductor. The values of the band gap were calculated by extrapolating to the x-axis in the Mott Schottky plots. The results are reported in wt.% respectively constructed from the UV-Vis recorded in F(R).

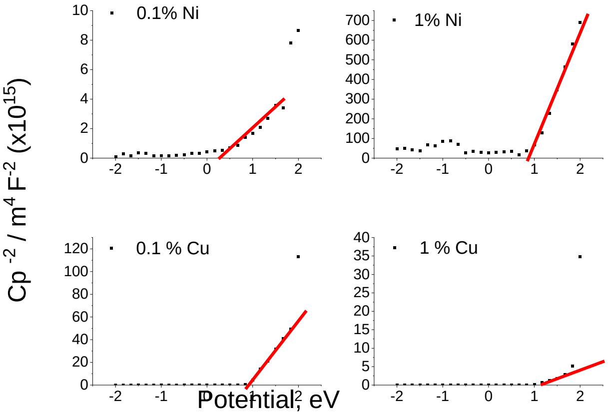

Figure 10. Mott Schottky plots for $MgAl_2O_4$ doped with Cu and Ni in 0.1 and 1% wt.%, respectively. Constructed form the UV Vis spectra recorded in F(R).

Table 3. Summary of collected data in this project: Band edge position values reported vs Ag/AgCl, determined from EIS and UV Vis Absorbance Spectroscopy for the doped samples.

Sample	Band Gap, eV (+/5-10%)	Conduction Band, eV	Valence band, eV
Ni 0.1%	3.8	0.18	-3.62
Ni 1%	2.7	0.84	-1.86
Ni 10%	2.9	-1.98	-4.88
Cu 0.1%	3.9	0.75	-3.15
Cu 1%	3.4	1.21	-2.19
Cu 10%	2.3	-1.92	-4.22
Non-doped	4.2	2.4	-1.6

To predict the thermodynamical feasibility of the electron injection between the SC and the PS. Following the equation $\Delta G = -nF[E°(D^{+/0}) - E°(A^{0/-})]$ (Ref. Section 2.4, Chapter2) we calculate the free Gibbs energy of the ET between the doped aluminates as SC and using Cu complexes (Chapter 5) as PS. the results are summarized on Table 4. Figure 12 shows the energy diagram where it combines the results obtained in this study and the ΔG values, represented in the energy diagram for its comprehension.

Table 4. ΔG of electron transfer calculations in between the doped aluminates studied in this chapter and the Cu complexes studied in Chapter 5, all values are reported in eV vs Ag/AgCl.

	Semiconductor			**Photosensitiser Cu (Xant)(biq-COOH)**		
	Eg	VB	CB	HOMO	LUMO	ΔG
$MgAl_2O_4$ Cu 0.1%	3.9	-3.15	0.75	-1.07	0.95	-2.1
$MgAl_2O_4$ Cu 1%	3.4	-2.19	1.21			-1.64
$MgAl_2O_4$ Ni 0.1%	3.8	-3.62	0.18			-2.6
$MgAl_2O_4$ Ni 1%	2.7	-1.86	0.84			-2.01

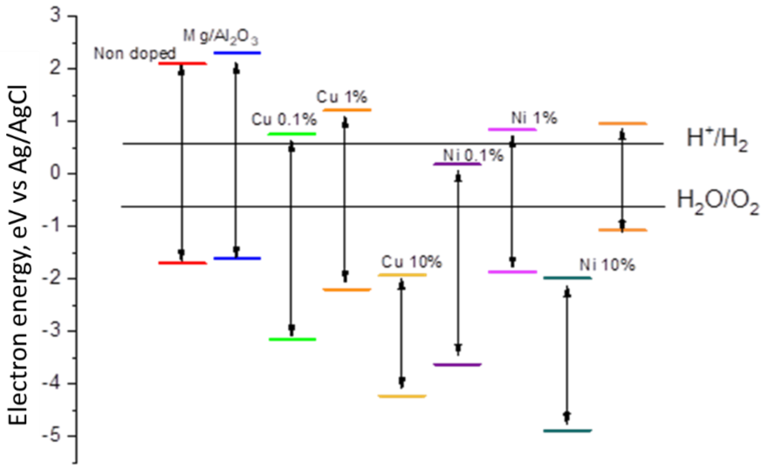

Figure 11. Energy Diagram constructed form the obtained values determined by Mott-Schottky plots and the Band Gap values determined by UV-Vis Absorbance spectroscopy.

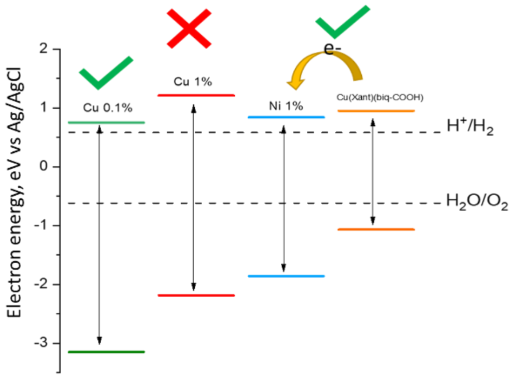

Figure 12. Energy diagram for the doped aluminates studied in this chapter and the Cu complexes studied in chapter 5 after the thermodynamic analysis.

Hydrogen evolution tests

The photocatalytic hydrogen evolution results (Figure 13) indicate that the sample doped with Cu 0.1% was the one with the highest hydrogen evolution rate with 8 µmol $H_2 \cdot g^{-1}$, followed by the sample with Ni 0.1%.In general the samples doped with Cu showed a higher amount of produced hydrogen than the ones doped with Ni. This experiments were carried out in collaboration with the Department of Eco materials and Energy Laboratory in the Institute of Civil Engineering at the Civil Engineering Faculty of the University of Nuevo Leon, Mexico in a reactor described in the Experimental methods section of this chapter.

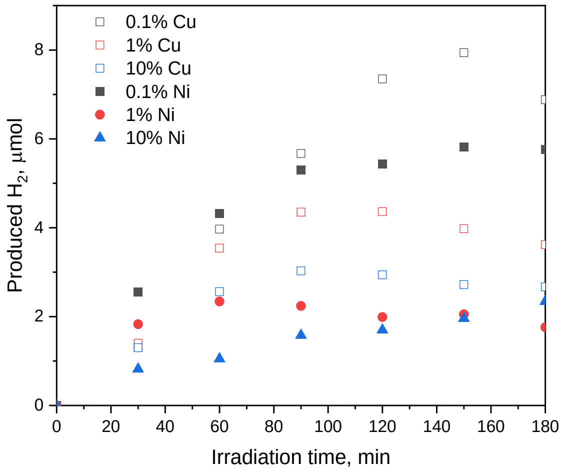

Figure 13. Hydrogen evolution tests under 254 nm irradiation after 180 min of reaction using the powders $MgAl_2O_4$ doped with Cu 0.1, 1 and 10% and Ni 0.1, 1 and 10% as photocatalysts.

In comparison with the previously studied aluminates, from the variety of aluminates without any dopant and synthesized by solid state studied before, the $MgAl_2O_4$ showed the best production rate of 7.3 $\mu molg^{-1}h^{-1}$ under 254 nm irradiation, among the others such as $SrAl_2O_4$ and Ba Al_2O_4 under same conditions.[41]

4.5 Conclusions

In this work $MgAl_2O_4$ Ni and Cu doped in 0.1, 1, 1, and 10% ratio, were synthetized by sol-gel method and characterized by UV-Vis Absorption, XRD and XPS. Band-gap for each material was calculated using Tauc's plots. The results demonstrate that the addition to Cu and Ni to the samples shift the absorbance bands to the visible decreasing the band gap values more drastically in the samples doped with 10% of the dopant, reducing the values from 4.2 eV to 2.3 eV and 2.9 eV for Cu and Ni, respectively. This reduction in the Eg values offer the possibility to make them photo catalytically active at lower energies. Additionally, the presence of Cu^{2+} and Ni^{2+} was confirmed in the form of oxides suggesting that these species are present as impurities and not inside of the crystal structure of the $MgAl_2O_4$ spinel. The photocatalytic hydrogen evolution tests under UV light shown a maximum rate of 8 $\mu molH_2 \cdot g^{-1}$ for the sample doped with 0.1 % of Cu. Even when doped aluminates showed lower rate of production in comparison with the non-doped $MgAl_2O_4$. We must point out that the aim of this project was to modify the semiconductor optical properties by moving the CB to lower energies to make it suitable for the injection of the excited electrons from the LUMO of the PS into the CB of the SC. The value of the CB bands position was successfully engineered, lowering the CB values in all the samples, values are reported in Table 4.

4.6 References

1. Kudo, A. & Miseki, Y. Heterogeneous photocatalyst materials for water splitting. *Chem. Soc. Rev.* **38**, 253–278 (2009).
2. Iwase, A., Kato, H. & Kudo, A. The effect of Au cocatalyst loaded on La-doped NaTaO3 on photocatalytic water splitting and O2 photoreduction. *Appl. Catal. B Environ.* **136**–**137**, 89–93 (2013).
3. Fujishima, a & Honda, K. Electrochemical photolysis of water at a semiconductor electrode. *Nature* **238**, 37–38 (1972).
4. Kenichi Honda, A. F. Electrochemical Photolysis of Water at a Semiconductor Electrode. *Nature* **238**, 37–38 (1972).
5. Chandrasekaran, S. *et al.* Spinel photocatalysts for environmental remediation, hydrogen generation, CO2 reduction and photoelectrochemical water splitting. *J. Mater. Chem. A* **6**, 11078–11104 (2018).
6. Tatarchuk, T., Al-Najar, B., Bououdina, M. & Aal Ahmed, M. A. *Catalytic and photocatalytic properties of oxide spinels*. *Handbook of Ecomaterials* vol. 3 (2019).
7. Zhang, L. W., Wang, L. & Zhu, Y. F. Synthesis and performance of BaAl2O4 with a wide spectral range of optical absorption. *Adv. Funct. Mater.* **17**, 3781–3790 (2007).
8. Diaz-Torres, L. A. *et al.* Efficient hydrogen generation by ZnAl2O4 nanoparticles embedded on a flexible graphene composite. *Renew. Energy* **152**, 634–643 (2020).
9. Diaz-Torres, L. A. *et al.* Long-lasting green, yellow, and red phosphorescence of carbon dots embedded on ZnAl2O4 nanoparticles synthesized by a combustion method. *J. Phys. D. Appl. Phys.* **51**, (2018).
10. Gómez-Solís, C., Peralta-Arriaga, S. L., Torres-Martínez, L. M., Juárez-Ramírez, I. & Díaz-Torres, L. A. Photocatalytic activity of MAl2O4 (M = Mg, Sr and Ba) for hydrogen production. *Fuel* **188**, 197–204 (2017).
11. Hashimoto, K., Irie, H. & Fujishima, A. TiO 2 photocatalysis: A historical overview and future prospects. *Japanese J. Appl. Physics, Part 1 Regul. Pap.*

Short Notes Rev. Pap. **44**, 8269–8285 (2005).

12. Carrasco-Jaim, O. A., Huerta-Flores, A. M., Torres-Martínez, L. M. & Moctezuma, E. Fast in-situ photodeposition of Ag and Cu nanoparticles onto AgTaO3 perovskite for an enhanced photocatalytic hydrogen generation. *Int. J. Hydrogen Energy* 1–14 (2020) doi:10.1016/j.ijhydene.2020.01.242.

13. Wang, C. *et al.* Enhanced hydrogen production by water splitting using Cu-doped TiO 2 film with preferred (0 0 1) orientation. *Appl. Surf. Sci.* **292**, 161–164 (2014).

14. Delsouz Khaki, M. R., Shafeeyan, M. S., Raman, A. A. A. & Daud, W. M. A. W. Enhanced UV–Visible photocatalytic activity of Cu-doped ZnO/TiO2 nanoparticles. *J. Mater. Sci. Mater. Electron.* **29**, 5480–5495 (2018).

15. Križan, J., Možina, J., Bajsić, I. & Mazaj, M. Synthesis and fluorescent properties of chromium-doped aluminate nanopowders. *Acta Chim. Slov.* **59**, 163–168 (2012).

16. Regmi, C. *et al.* Understanding the multifunctionality in Cu-doped BiVO4 semiconductor photocatalyst. *J. Environ. Sci. (China)* **75**, 84–97 (2019).

17. Ran, J., Zhang, J., Yu, J., Jaroniec, M. & Qiao, S. Z. Earth-abundant cocatalysts for semiconductor-based photocatalytic water splitting. *Chem. Soc. Rev.* **43**, 7787–7812 (2014).

18. V. Elakkiya, R. Abhishekram, S. Sumathi. Copper doped nickel aluminate: Synthesis, characterisation, optical and colour properties. *Chinese J. Chem. Eng.* **27**, 2596–2605 (2019).

19. Camarillo, R., Rizaldos, D., Jiménez, C., Martínez, F. & Rincón, J. Enhancing the photocatalytic reduction of CO2 with undoped and Cu-doped TiO2 nanofibers synthesized in supercritical medium. *J. Supercrit. Fluids* **147**, 70–80 (2019).

20. Yathisha, R. O. *et al.* Study on the effect of Zn 2+ doping on optical and electrical properties of CuO nanoparticles. *Phys. E Low-Dimensional Syst. Nanostructures* **108**, 257–268 (2019).

21. V., E., R., A. & S., S. Copper doped nickel aluminate: Synthesis, characterisation, optical and colour properties. *Chinese J. Chem. Eng.* (2019)

doi:10.1016/j.cjche.2019.01.008.

22. de Souza, L. K. C. *et al.* Blue pigments based on CoxZn1-xAl2O4 spinels synthesized by the polymeric precursor method. *Dye. Pigment.* **81**, 187–192 (2009).

23. V Elakkiya, R Abhishekram, S. Sumathi & S., S. Copper doped nickel aluminate: Synthesis, characterisation, optical and colour properties. *Chinese J. Chem. Eng.* **27**, 2596–2605 (2019).

24. Monshi, A., Foroughi, M. R. & Monshi, M. R. Modified Scherrer Equation to Estimate More Accurately Nano-Crystallite Size Using XRD. *World J. Nano Sci. Eng.* **02**, 154–160 (2012).

25. Yin, M. *et al.* Copper oxide nanocrystals. *J. Am. Chem. Soc.* **127**, 9506–9511 (2005).

26. Yang, Y., Xu, D., Wu, Q. & Diao, P. Cu2O/CuO bilayered composite as a high-efficiency photocathode for photoelectrochemical hydrogen evolution reaction. *Sci. Rep.* **6**, (2016).

27. Safeer N. K., M., Alex, C., Jana, R., Datta, A. & John, N. S. Remarkable COxtolerance of Ni3+active species in a Ni2O3catalyst for sustained electrochemical urea oxidation. *J. Mater. Chem. A* **10**, 4209–4221 (2022).

28. Tahereh Gholami, Masoud Salavati-Niasari & Shokufeh Varshoy. Electrochemical hydrogen storage capacity andoptical properties of NiAl2O4/NiO nanocompositesynthesized by green method. *Int. J. Hydrog.* (2017).

29. Han, M. *et al.* Physical properties of MgAl2O4, CoAl2O4, NiAl2O4, CuAl2O4, and ZnAl2O4 spinels synthesized by a solution combustion method. *Mater. Chem. Phys.* **215**, 251–258 (2018).

30. Patterson, A. L. The scherrer formula for X-ray particle size determination. *Phys. Rev.* **56**, 978–982 (1939).

31. Goga, F. *et al.* Influence of the thermal treatment on the colour of ro·Al2O3 (R=Co, Ni) type spinel pigments prepared by a modified sol – gel method. *Stud. Univ. Babes-Bolyai Chem.* **61**, 263–273 (2016).

32. MURPHY, A. Band-gap determination from diffuse reflectance measurements of semiconductor films, and application to photoelectrochemical water-splitting. *Sol. Energy Mater. Sol. Cells* **91**, 1326–1337 (2007).

33. Mir, F. A. Transparent wide band gap crystals follow indirect allowed transition and bipolaron hopping mechanism. *Results Phys.* **4**, 103–104 (2014).

34. Das, S. C. *et al.* Band gap tuning in ZnO through ni doping via spray pyrolysis. *J. Phys. Chem. C* **117**, 12745–12753 (2013).

35. Ghosh, A., Kumari, N. & Bhattacharjee, A. Influence of Cu doping on the structural, electrical and optical properties of ZnO. *Pramana - J. Phys.* **84**, 621–635 (2015).

36. Tian, H. *et al.* Fabrication of an efficient noble metal-free TiO2-based photocatalytic system using Cu-Ni bimetallic deposit as an active center of H2 evolution from water. *Sol. Energy Mater. Sol. Cells* **134**, 309–317 (2015).

37. Parthibavarman, M., Sathishkumar, S., Prabhakaran, S., Jayashree, M. & BoopathiRaja, R. High visible light-driven photocatalytic activity of large surface area Cu doped SnO2 nanorods synthesized by novel one-step microwave irradiation method. *J. Iran. Chem. Soc.* **15**, 2789–2801 (2018).

38. Lee, J. H., Noh, Y. W., Jin, I. S., Park, S. H. & Jung, J. W. Efficient perovskite solar cells with negligible hysteresis achieved by sol-gel-driven spinel nickel cobalt oxide thin films as the hole transport layer. *J. Mater. Chem. C* **7**, 7288–7298 (2019).

39. Hankin, A., Bedoya-Lora, F. E., Alexander, J. C., Regoutz, A. & Kelsall, G. H. Flat band potential determination: Avoiding the pitfalls. *J. Mater. Chem. A* **7**, 26162–26176 (2019).

40. Cesiulis, H., Tsyntsaru, N., Ramanavicius, A. & Ragoisha, G. *Nanostructures and Thin Films for Multifunctional Applications*. *Nanostructures and Thin Films for Multifunctional Applications* (2016). doi:10.1007/978-3-319-30198-3.

41. Gómez-solís, C., Peralta-arriaga, S. L., Torres-martínez, L. M., Juárez-ramírez, I. & Díaz-torres, L. A. Photocatalytic activity of MAl 2 O 4 (M = Mg , Sr and Ba) for hydrogen production. **188**, 197–204 (2017).

Chapter 5

Cu complexes as photosensitisers for photoelectrochemical water splitting.

This chapter describes the synthesis, electrochemical and photophysical characterization of several new Cu(I) complexes, for their use as photosensitisers. Their characteristics, including the fact that they are based on a cheap, abundant metal centre, are photostable, and absorb in the visible region make them suitable photosensitisers (PS) of “sensitized photoanodes” for photoelectrochemical (PEC) water splitting.

Part of this chapter is based on the results obtained by an MSc student, Evie Karkera as part of her MSc project, performed under my supervision and design in 2021 with the collaboration of Martin Appleby.

5.1 List of Figures

5.2 Introduction

As it has been established in previous chapters, the search for new renewable technologies to produce clean fuels such as H_2 has been increasing exponentially in recent decades[1]. Artificial photosynthetic systems (APS) for applications in hydrogen production via water splitting under solar light has been accepted as a promising technology. Unfortunately, there still are a few problems associated with these artificial photosynthetic systems, including photo-corrosion, fast charge recombination, energy losses, and that most of them are not active under visible light.

Several approaches have been taken to understand the mechanism of action of these systems and improve their efficiencies. One of these approaches, inspired by the dye-sensitized solar cells, is the use of metalorganic complexes as light harvesters, mimicking the chlorophyll's function in plants.[2]

The PS must meet the following criteria to be used as a dye on photoanodes.[3]

- Proper alignment of the energy levels of the excited state of the dye so the electron form the PS can be injected into the conduction band of the SC.
- High-rate and high efficiency of electron transfer from the dye to the semiconductor metal-oxide.
- Good thermal and electrochemical stability.
- Strong absorption in the visible region of the spectrum and at the semiconductor conduction band edge.
- Possession of anchoring groups, that can bind to the surface of semiconductor (for example, O or –OH groups that can chelate to the Ti(IV) sites on the surface of TiO_2).

A lot of different semiconductors have been used as supports in photoanodes, of which TiO_2 and aluminates are prominent examples. To improve the SC efficiency under Sunlight, PS have been used as light harvesting antennas. These type of systems are called "hybrid" because they have a heterogeneous and a homogeneous component. There, the SC acts as an electron reservoir, accumulating the charge transferred from the electron injection of the PS into the SC and releasing them "on demand" for catalysis.[4]

Recently, various transition metal complexes especially those of Ru[5,6] and Ir,[7–10] have demonstrated good efficiencies as photosensitizers in photocatalysis. Nevertheless, these materials are expensive due to their scarcity in the Earth's crust. That is why it is important to develop new complexes based on Earth-abundant and cheap transition metals. Various types of catalysts are now based on first row transition metals such as Ni[11–14], Co[15,16], Fe[17–19] and Cu[20]; in both homogeneous and heterogeneous catalysts.

Cu complexes have characteristics that make them promising candidates for application in photocatalysis. Copper is an abundant element; therefore, it is inexpensive and much cheaper than noble metals. The availability of a range of oxidation states (Cu^0,Cu^+, Cu^{2+}, and Cu^{3+}) make them suitable for applications involving electron transfer such as electrocatalysts.[20]

One of the characteristics that make a PS suitable for sensitising the semiconductor is a long-lived excited state and unfortunately most of the 1st row transition metal complexes studied so far have a short lifetime, thus making the electron transfer between the PS and the SC inefficient.

This study is focused on Cu(I) diphosphine-diimine complexes as photosensitisers. Such complexes have two key properties required from an efficient PS: an MLCT absorption extending significantly into the visible region, and the potential to tune their optical properties by modifying the periphery of the ligands or to attach functional groups which allow immobilisation onto a SC surface.[21]

Cu(I) diimine complexes normally possess short-excited state lifetimes, which makes them often not suitable for use as photosensitisers in molecular catalysis. The short excited state lifetime is due to a geometry distortion called "Jahn-Teller distortion", where they change from a pseudo-tetrahedral ground state geometry of Cu(I) to a pseudo square-planar one in the MLCT excited state, which formally contains Cu(II).[22–26] This distortion creates vacancies in the coordination states that interact with the solvent which quenches the excited state.[22,23,27]

Recent studies have shown that Cu(I) complexes containing one diimine ligand, and one diphosphine ligand such as 4,5-bis(diphenylphosphino)-9,9-dimethyl-xanthine (xantphos), which has a large bite angle and high steric hindrance, leads to a longer excited states lifetime (ns–ms).[21,28]

Using a strongly electron-accepting diimine ligand will cause a redshift of the absorbance due to the MLCT transition, Cu(I)→diimine (leading to Cu(II)-diimine(-) excited state). Using the xantphos ligand prevents Jahn-Teller distortion (tetrahedral Cu(I) → towards planar in the formally Cu(II) MLCT excited state), which is usually the cause of fast deactivation of the excited state.[21,28,29]

This chapter describes the synthesis and characterization of two novel copper complexes, [Cu(xantphos)(biq-COOH)]BF_4 and [Cu(xantphos)(phen-COOH)]BF_4 for their subsequent application as PS in the development of new photoanodes for water splitting (Figure 1).

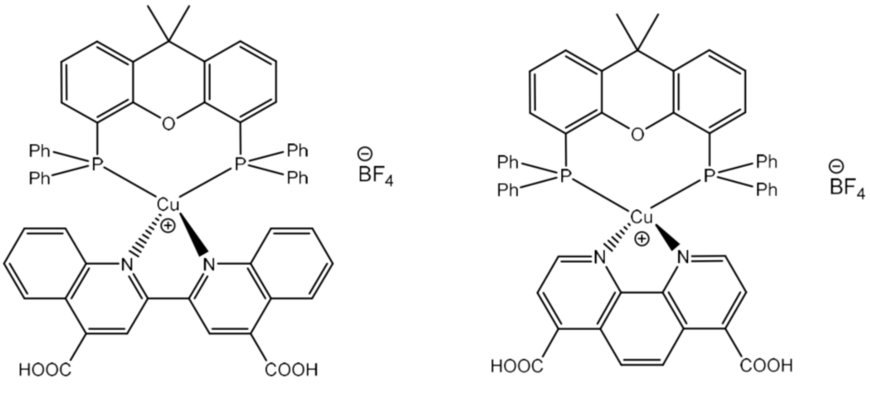

$[Cu(xantphos)(biq\text{-}COOH)]BF_4$ $[Cu(xantphos)(phen\text{-}COOH)]BF_4$

Figure 1. Copper complexes studied in this chapter.

5.3 Experimental methods

Materials

The ligand [1,10-phenanthroline]-4,7-dicarboxylic acid, phen-COOH, was prepared and characterised previously in the group, by Dr Dylan Pritchard. All other reagents were purchased from Sigma-Aldrich and used as received. Dry solvents were obtained from the University of Sheffield Grubbs solvent drying system.

Characterisation

The prepared Cu(I) complexes were characterized by spectroscopic and electrochemical techniques.

Nuclear Magnetic Resonance (NMR) of the synthetized complexes: ^{1}H and ^{13}C spectra were recorded at 400 MHz on a Bruker Avance 400 spectrometer. Deuterated solvents were purchased from Sigma-Aldrich and were of spectroscopic grade. All chemical shifts are reported in parts per million (ppm), with ^{1}H NMR spectra being calibrated relative to the residual solvent signal.

Mass Spectroscopy was analysed in a Water LTC Mass Spectrometry equipment with Atmospheric Pressure Chemical Ionisation (APCI) for non-polar molecules in the mass range 100 to 3000 Daltons.

Absorption spectra and extinction coefficients were measured on a Cary 5000 NIR-UV-Vis Spectrometer using a 1-cm pathlength quartz cell in different solvents, from 200 to 800 nm.

Emission spectroscopy. All spectra were recorded using a Horiba Jobin-Yvon Fluoromax-4 spectrofluorometer at room temperature using a quartz 1 cm-pathlength cuvettes.

Cyclic voltammetry was recorded with an Autoloab® STAT100 potentiostat. A conventional 3-electrodes cell was used, with an Ag/AgCl reference electrode, Pt as counter electrode and a glassy-carbon as working electrode (Figure 2). $TBAPF_6$, at 0.2M was used as an electrolyte in dry acetonitrile, concentration of the compound studied was approximately 1 mM.

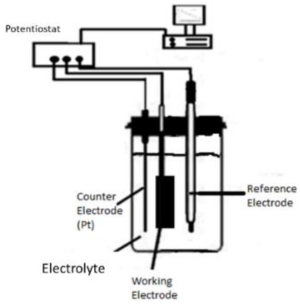

Figure 2. Simplified scheme of an Electrochemical 3-electrode cell.

Femtosecond Transient Absorption (TA) spectroscopy was performed at the Lord Porter Laser Laboratory, University of Sheffield. A Ti:Sapphire regenerative amplifier (Spitfire ACE PA-40, Spectra-Physics) provided 800 nm pulses (40 fs FWHM, 10 kHz, 1.2 mJ). 400 nm pulses for excitation were generated by doubling a portion of the 800 nm output in a β-barium borate crystal within a commercially available doubler/tripler (TimePlate, Photop Technologies). White light supercontinuum probe pulses in the range 340–790 nm, were generated by tightly focusing ca. 1 µJ of the 800 nm output on a CaF_2 crystal (continuously displaced to avoid damage). Detection was achieved using a commercial transient absorption spectrometer (Helios, Ultrafast Systems) using a 2048-pixel CMOS sensor for the UV-vis spectral range. The relative polarisation of the pump and probe pulses was set to the magic angle of 54.7˚ for anisotropy-free measurements. Samples were held in 2 mm pathlength quartz cells and were stirred during experiments. The optical density at the excitation wavelength was kept at approximately 0.5. The optical density across the probe range was kept below 1.0. Excitation energies were kept below 2 µJ.

5.4 Results

Synthesis and characterization of Cu complexes

Synthesis of [Cu(xantphos)(biq-COOH)]BF$_4$ complex was synthesized by dissolving tetrakis(acetonitrile)copper-(I) tetrafluoroborate (0.101 g, 0.320 mmol), xantphos (0.200 g, 0.346 mmol), and biq-COOH (0.093 g, 0.271 mmol) in methanol (30 mL). The resulting mixture was sonicated for 30 minutes, a change in colour from cloudy whit to orange was observed, confirming the formation of the product. After this the solvent was evaporated leaving behind a reddish solid. The latter was re-dissolved in a minimal amount of DCM. This solution was added dropwise to cold diethyl ether (150 mL) producing a red solution and an orange precipitate. The precipitate was filtered to produce a very fine orange powder (Figure 3). The obtained product was purified by column chromatography using a Sephadex LH-20 column and methanol as the eluent. Crude yield = 0.1553 g, 0.145 mmol (53%) orange solid. ^{1}H NMR (400 MHz, DMSO-d_6/acetone-d) δ (ppm): 9.27 (s, 1H, ArH), 8.34 (d, J = 8.74 Hz, 1H, ArH), 7.93 (d, J = 7.56 Hz, 2H, ArH), 7.74 (d, J = 8.09 Hz, 1H, ArH), 7.42 (s, 13H, ArH), 7.39 – 7.30 (m, 6H, ArH), 7.30 – 7.12 (m, 4H, ArH), 7.07 (s, 1H, ArH), 6.91 (s, 6H, ArH), 6.65 (s, 1H, ArH), 1.63 (s, 6H, CH3). ES-MS m/z: calculated for [C59H44CuN2O5P2]+: 986.48; found: 986 [M]+.

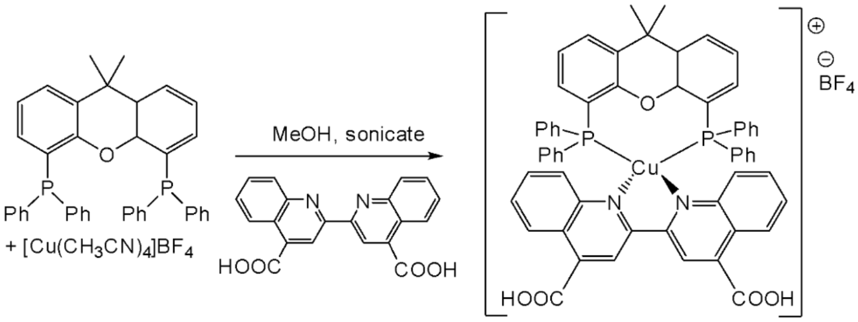

Figure 3. Reaction scheme for the synthesis of [Cu(xantphos)(biq-COOH)]BF_4.

Preliminary ^{1}H NMR analysis coupled with comparison of the maximum absorbance peaks of each product indicated that the complexes were not pure. This was expected to a degree due to the inefficiencies mentioned above which led to unreacted starting material present in the sample. Characterisation by mass spectrometry showed that the desired complex was indeed present in each sample, however it was clear each product was not pure. Spectra of the crude products (^{1}H NMR, mass spectrometry, UV-visible absorbance) can be found in Appendix B/C5.

The first method used to purify the products was a vapour diffusion recrystallisation in dichloromethane and *n*-hexane. Since the complex was known to be soluble in dichloromethane but insoluble in *n*-hexane, the gradual diffusion of *n*-hexane into the sample solution would slowly crash out the pure product as crystals. Unfortunately, only one of the prepared samples produced crystals after the solvent had evaporated. This was potentially due to the evaporation occurring too fast, or because the boiling point of *n*-hexane (69 °C) is higher than that of dichloromethane (40 °C), so it was more likely that the dichloromethane was diffusing into the *n*-hexane. Consequently, the vapour diffusion was repeated using diethyl ether in place of *n*-hexane, since the former has a boiling point of 35 °C. While this approach did appear to produce orange crystals, the limited time available meant that it was not possible to get the results of a single crystal X-ray diffraction analysis.

Due to time constraints, it was not possible to use the vapour diffusion method to purify all the products after verifying that crystals were produced. Column chromatography was therefore performed using a Sephadex LH-20 column and methanol as the eluent. Sephadex was chosen as the stationary phase due to the incompatibility of more commonly used silica and alumina stationary phases with aromatic carboxylic acids.[30] This powder, while certainly purer than the original products, still contains some impurities as seen in the further characterisation described below on this chapter.

Figure 4. Orange product obtained from the synthesis of [Cu(xantphos)(biq-COOH)]BF_4 after purification.

Synthesis of [Cu(xantphos)(phen-COOH)]BF4 Tetrakis(acetonitrile)copper-(I) tetrafluoroborate (0.0457 g, 0.145 mmol) and xantphos (0.0755 g, 0.130 mmol) were dissolved separately in acetonitrile (5 mL each). The xantphos solution was added dropwise to the Cu(I) solution and then stirred for 15 minutes at room temperature in the dark. 1,10-phenanthroline-4,7-dicarboxylic acid (phen-COOH, 0.0323 g, 0.0120 mmol) in methanol (5 mL) was then added dropwise to the reaction mixture, resulting in a clear yellow solution. Excess solvent was removed, and the resulting concentrated solution was dropwise added to cold deionised water (100 mL), producing a yellow precipitate. The solution was cooled in the fridge at approx. 5ºC overnight, the precipitate formed was filtered to produce a yellow powder. Crude yield = 0.0146 g, 0.0146 mmol (12%) yellow solid (Figure 5). ^{1}H NMR (400 MHz, Chloroform-d) δ (ppm): 7.69 (d, J = 7.48 Hz, 2H, ArH), 7.59 (d, J = 7.49 Hz, 2H, ArH), 7.47 (q, J = 6.21 Hz, 13H, ArH), 7.23 (q, J = 7.44 Hz, 14H, ArH), 7.04 (t, J = 7.43 Hz, 9H, ArH), 6.92 – 6.83 (m, 10H, ArH), 6.74 – 6.64 (m, 5H, ArH), 1.83 (s, 6H, CH3). 31P NMR (162 MHz, Chloroform-d) δ (ppm): -16.17. ES-MS m/z: calculated for [C53H40CuN2O5P2]+: 910.41; found: 910 [M]+.

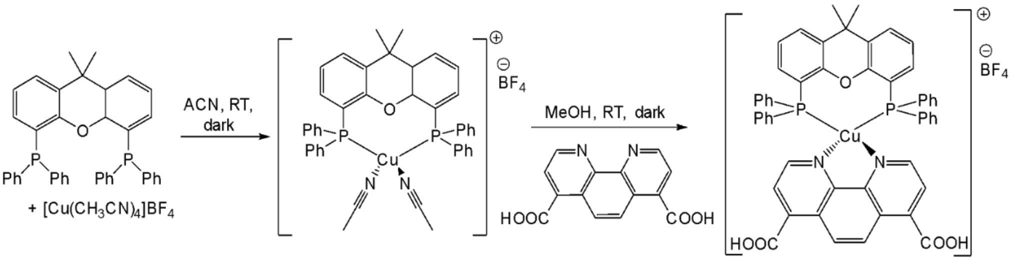

Figure 5. Reaction scheme for the synthesis of [Cu(xantphos)(phen-COOH)]BF$_4$

The obtained yellow powder product was purified by column chromatography a Sephadex LH-20 column and methanol as the eluent. Sephadex was chosen as the stationary phase due to the incompatibility of more commonly used silica and alumina stationary phases with aromatic carboxylic acids (Figure 6).[30]

Figure 6. Yellow product obtained from the synthesis of [Cu(xantphos)(phen-COOH)]BF_4 after purification.

Nuclear Magnetic Resonance

The ^{1}H NMR spectrum of [Cu(xantphos)(biq-COOH)]BF_4 is shown in Figure 7. The complex has 13 distinct proton environments, 6 on the biquinoline-COOH ligand and 7 on the xantphos ligand. The spectrum shows roughly 10 environments, however taking the integration ratios into account there appear to be the right number of hydrogens, but some of the signals are merged with each other and occasionally with impurity signals (marked with a star in Figure 7). There are two singlet peaks which can be assigned to the isolated protons: in H13 (9.08 ppm) and the methyl group protons H1 (1.92 ppm).

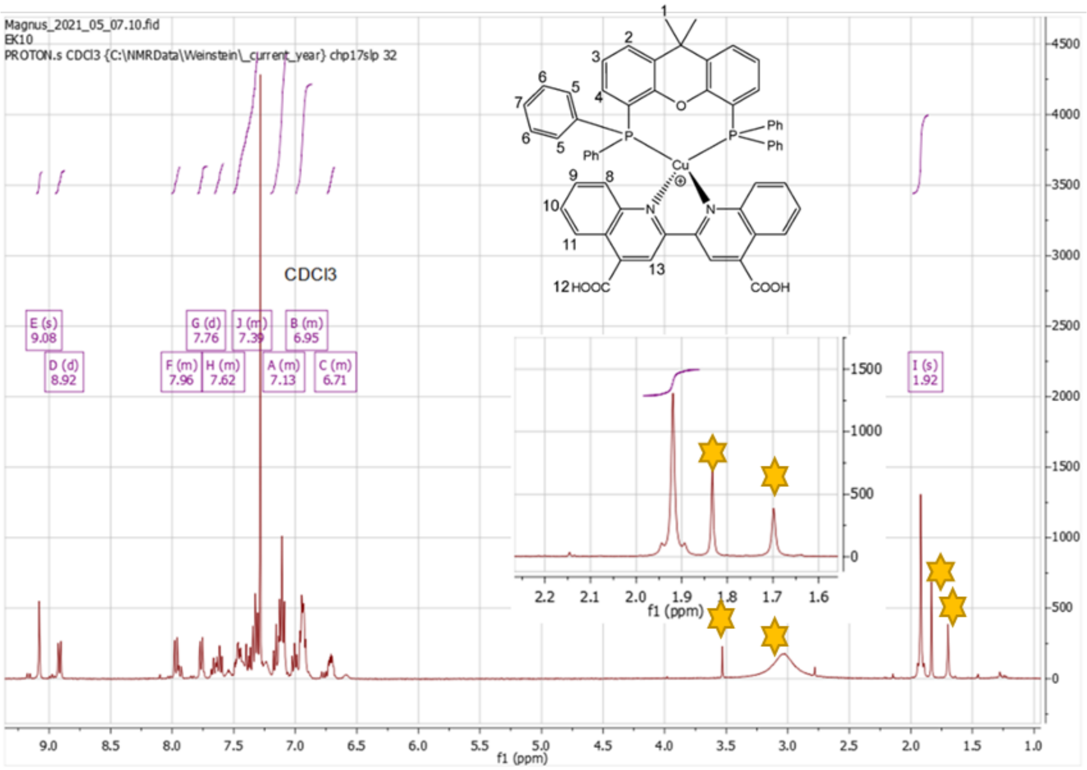

Figure 7. ^{1}H NMR of [Cu(xantphos)(biq-COOH)]Bf4 in $CDCl_3$.

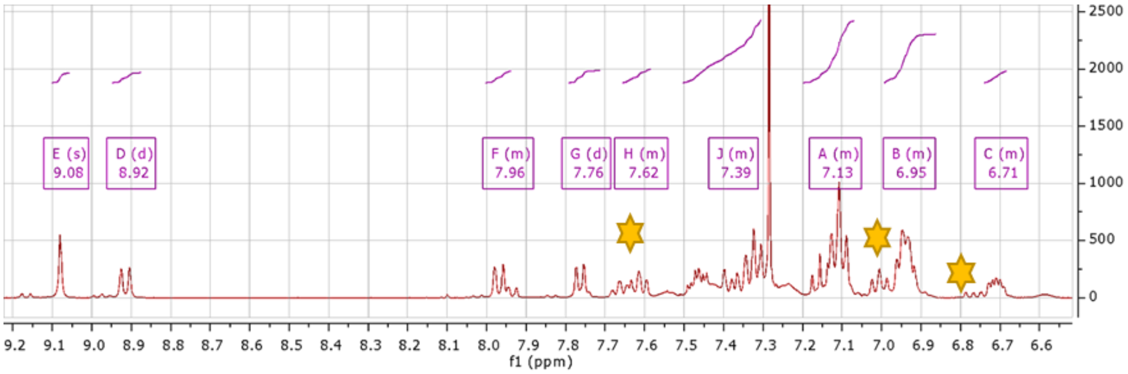

Figure 8. Expansion of the aromatic region of the 1H NMR spectrum (Figure 7) of Cu(xantphos)(biq-COOH)Bf4 in CDCl3.

Figure 8 shows peaks that corresponds to the xantphos ligand (D, F, G and A, C) and some impurities where detected (marked with a start in Figure 8) near “ H”, “B” and C signals. The high intensity signal at 7.28 ppm is a chloroform solvent peak which unfortunately partially obscures signal ‘J’.

The ^{31}P NMR of [Cu(xantphos)(biq-COOH)]BF_4 is shown in Figure 9. It presents two peaks, one at -11.01 and one at -17.70 ppm.[31]

The resonance at -11.01 ppm represents the equivalent environment of the two P atoms in the coordinated xantphos ligand. The other peak at more negative ppm can be attributed to free xantphos remaining in the product solution. Figure 10 shows the NMR of the complex [Cu(xantphos)(phen-COOH)]BF_4 recorded in $CDCl_3$.

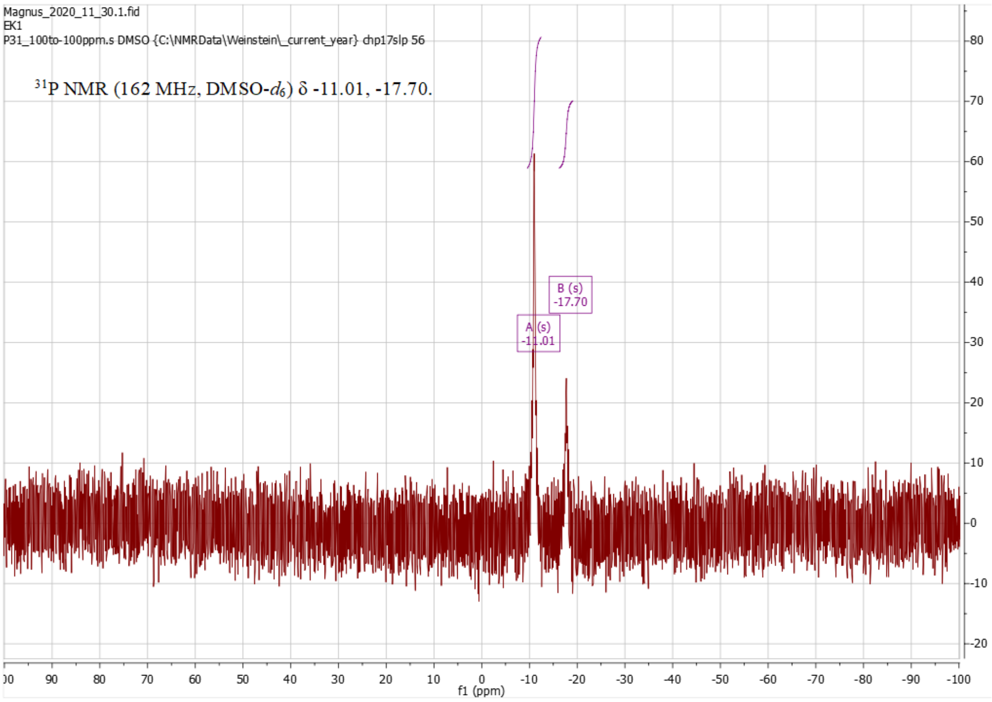

Figure 9. ^{31}P NMR spectrum of the orange solid in d6-DMSO showing the main resonance at -11.01 ppm corresponding to [Cu(xantphos)(biq-COOH)]BF_4 at 162 MHz.

[Cu(xantphos)(phen-COOH)]BF_4 ^1H NMR (Figure 10) confirms the presence of eight of the predicted eleven proton environments. To an extent this is expected due to the similar environments present in xantphos as discussed previously, as well as the elusiveness of the carboxylic acid environment. Since the complex is symmetrical, each peak is expected to contain an even number of protons greater than or equal to two. This is not the case, as especially the peaks corresponding to xantphos (peaks ‘C’ to ‘G’) correspond to a higher number of protons than expected in these environments. This implies that there is possibly some unattached xantphos ligand present in the sample. There are also several solvent peaks and impurities present, mainly at lower ppm values.

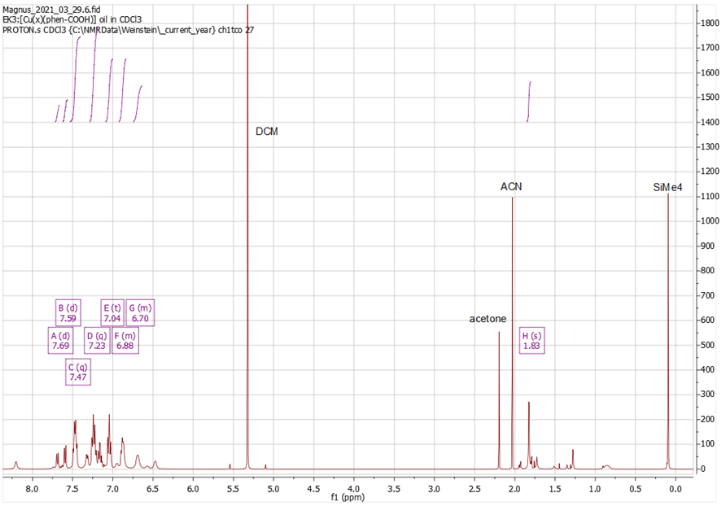

Figure 10. ^{1}H NMR of [Cu(xantphos)(phen-COOH)]BF_4 in $CDCl_3$.

The expansion of the aromatic region shown in Figure 11, shows the peaks assigned to the complex. There is a singlet peak missing that corresponds to 2H in environment 11, however the other peaks correspond to the [Cu(xantphos)(phen-COOH)]BF_4. Peaks ‘A’ and ‘B’ can be assigned to environments 8 and 9, while ‘C’ to ‘G’ match similar spectra of xantphos although the lower ppm peaks are not very well defined.

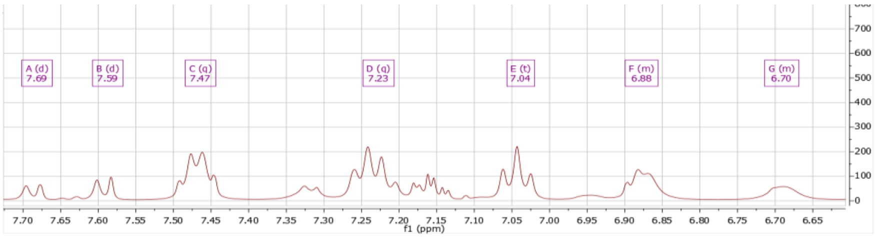

Figure 11. *Expansion of the aromatic region of the ^{1}H NMR spectrum of* [Cu(xantphos)(phen-COOH)]BF_4 *in $CDCl_3$.*

Mass Spectrometry

The electrospray mass spectrum for [Cu(xantphos)(biq-COOH)]BF_4 is shown in Figure 12. The calculated molecular weight for the complex ($C_{59}H_{44}CuN_2O_5P_2^+$) was 986.50 g mol^{-1}. The spectrum shows a peak at 985 m/z which corresponds to the $[M]^+$ ion minus one hydrogen atom. The peak at 641 m/z corresponds to the molecular weight of a Cu-xantphos fragment (molecular weight = 642.18 g mol^{-1}) missing one hydrogen. The peak at 611 m/z could be a fragment of $[Cu(xantphos)_2]^{2+}$ which has a total molecular weight of 1220 g mol^{-1}.

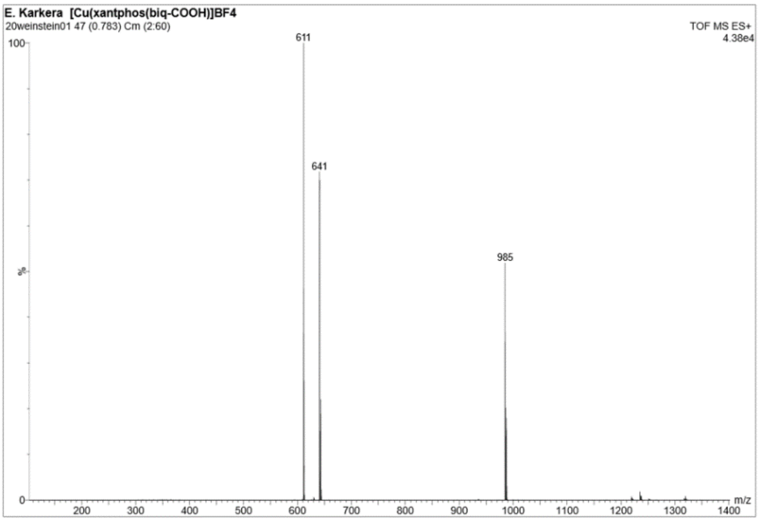

Figure 12. *ES Mass spectrum of* [Cu(xantphos)(biq-COOH)]BF_4*.*

Copper has two stable isotopes, ^{63}Cu (69%) and ^{65}Cu (31%). The combinations of these isotopes with the presence and absence of one hydrogen atom account for the four peaks seen in the expansion of the mass spectrum in Figure 13.

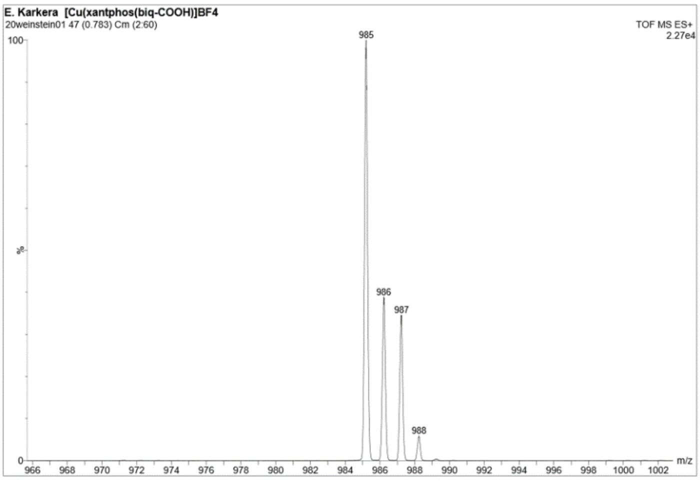

Figure 13. Enlargement of the spectrum showing isotopic distribution about the $[M]^+$ peak of $[Cu(xantphos)(biq\text{-}COOH)]BF_4$.

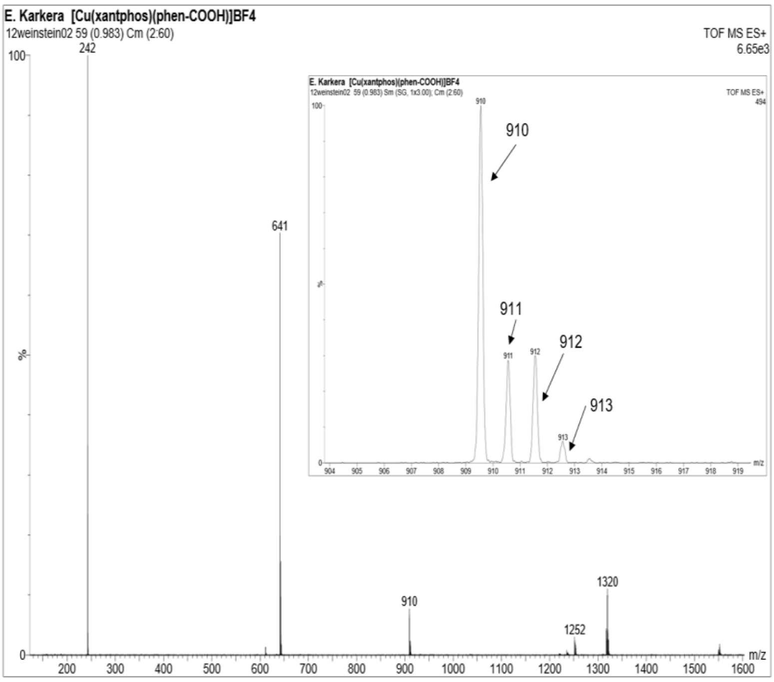

Figure 14. *ES Mass spectrum of* $[Cu(xantphos)(phen\text{-}COOH)]BF_4$.

The calculated molecular weight for the complex ($C_{53}H_{40}CuN_2O_5P_2^+$) was 910.40 g mol^{-1}. The spectrum in Figure 14, shows a peak at 910 m/z which corresponds to the $[M]^+$ ion. The peak at 641 m/z matches the molecular weight of a Cu-xantphos fragment (molecular weight = 642.18 g mol^{-1}). The peaks at 910 – 913 m/z correspond to the two isotopes of copper (^{63}Cu and ^{65}Cu) and the addition or removal of one proton.

Steady state UV-Vis Absorption spectroscopy

The absorption spectra were recorded in DCM for both complexes and is shown in Figure 15. [Cu(xantphos)(biq-COOH)]BF_4 exhibit an intense band at 370 nm and a weaker band at 500 nm (max = 445nm, ε = 2930 M^{-1} cm^{-1}). [Cu(xantphos)(phen-COOH)]BF_4 shows one MLCT transition band at lower energies with a maximum absorbance at 400 nm.

Both bands are characteristic of an MLCT transitions from the $S_0 \rightarrow S_2$ and $S_0 \rightarrow S_1$ involving electron transfer of a Cu d-electron to the π*-orbital of the N^N ligand (biq, biq-COOH, phen-COOH).[26] This difference can be a result of the change in structure of the N^N ligand, whereby a more conjugated structure decreases the energy of the LUMO. In [Cu(xantphos)(biq)]BF_4, an MLCT transition occurs at 455 nm.[32] In [Cu(xantphos)(biq-COOH)]BF_4 studied in this project, the MLCT peak is red-shifted to 480 nm, which can be attributed to the electron withdrawing character of the carboxylic groups, which reduce the energy of the diimine-localised LUMO.[32,3334]

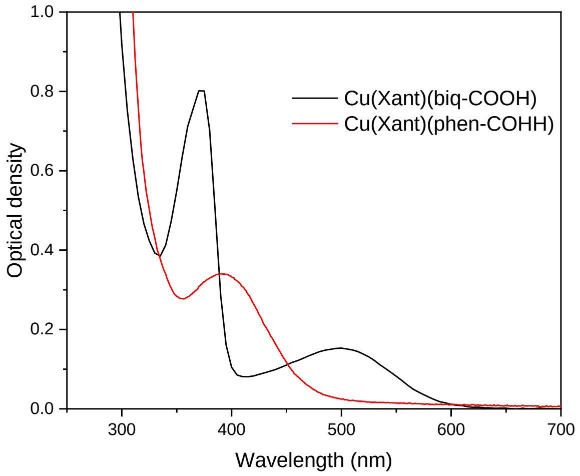

Figure 15. UV-vis absorption spectra of [Cu(xantphos)(biq-COOH)]BF_4 (black) and [Cu(xantphos)(phen-COOH)]BF_4 (red), both recorded in DCM at room temperature.

Emission Spectroscopy

The emission spectra of both copper complexes are shown in Figure 16, both complexes exhibit a long emission in the range of 600–800nm. [Cu(xantphos)(biq-COOH)]BF_4 complex presents a maximum emission band at 730 nm after excitation at 485 nm. [Cu(xantphos)(phen-COOH)]BF_4 showed an emission band at ~670 nm after excitation at 390 nm. The results are summarized Table 1.

Another Cu complexes with bulky substituents in the ligand, such as $[Cu(dmphen)_2]^+$ and $[Cu(dpphen)_2]^+$, has been studied showing that those type of structures exhibits long-lived emission around 700-800 nm due to the phosphorescence process happening form the lowest ^{3}MLCT state to the ^{1}MLCT state.[26]

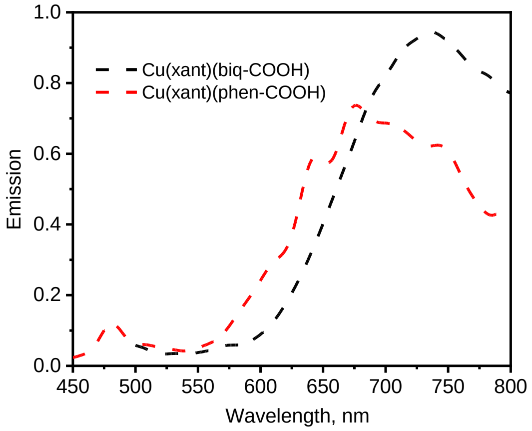

Figure 16. Emission spectra of Cu complexes studied in this work, recorded in DCM, excitation at 390 nm for the phen-COOH complex, and at 485 nm for the biq-COOH complex.

Additionally, [Cu(xantphos)(phen-COOH)]BF_4 spectra (Figure 16) shows a broad band that seems to be formed by different overlapped absorption bands, this could be a sign on the presence of impurities on the product. For this reason, decided to go ahead with the other complex and purify this one again but due to lack of time this couldn't been completed so we only used the [Cu(xantphos)(biq-COOH)]BF_4 for further experiments and analysis.

Cyclic Voltammetry

The cyclic voltammogram of [Cu(xantphos)(biq-COOH)]BF_4 in dry acetonitrile is shown in Figure 17. It shows a quasi-reversible $Cu^{I/II}$ oxidation at 1.67 V (*vs.* Fc/Fc^+) which indicates Cu-based HOMO.[33] This value is similar to the oxidation couple of [Cu(xantphos)(biq)]tfpb reported in the literature (0.95 V).[233] Additionally, multiple reduction processes (-0.67 V, -1.67 V) which do not appear to be reversible, where found whereas the $N^\wedge N^{0/I}$ reduction of biquinoline-COOH is expected. Since the difference ($\Delta E_{1/2}$) between $E_{1/2}(Cu_{I/II})$ and $E_{1/2}(N^\wedge N^{0/I})$ is the energy gap between the

HOMO and LUMO, the UV-visible absorption spectrum for [Cu(xantphos)(biq-COOH)]BF_4 can be used to estimate which of the three reduction processes is most likely to be the biquinoline-COOH. The energy of the photon absorbed by the MLCT transition of the complex (promoting an electron from the Cu-based HOMO to the ligand-based LUMO) corresponds to $\Delta E_{1/2}$ (Eq. 3 and 456).

$$\Delta E_{1/2} = E_{1/2}\left(Cu^{\frac{I}{II}}\right) - E_{1/2}\left(N^{\frac{0}{I}}\right) \qquad \text{Eq. 1}$$

$$E_{1/2}\left(N^\wedge N^{\frac{0}{I}}\right) = E_{1/2}\left(Cu^{\frac{I}{II}}\right) - \Delta E_{1/2} \qquad \text{Eq. 2}$$

Using this equation and the MLCT absorption wavelength at 485 nm which gives a photon energy of 2.56 eV, the biquinoline-COOH reduction $E_{1/2}$ is expected at -1.65 V. This is an approximation because different solvents were used for each measurement, however there is a reduction process peak at -1.67 V (red squared). This value matches the predicted value.

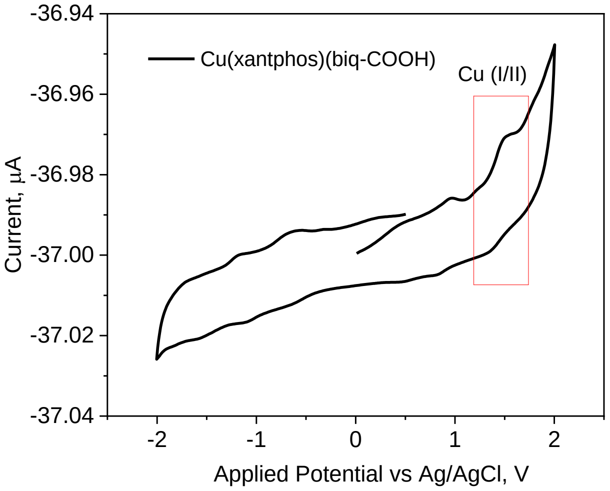

Figure 17. Cyclic voltampergramm of [Cu(xantphos)(biq-COOH)]BF_4 in 0.5 M [NBu4]PF_6 solution in dry acetonitrile. Scan rate 100 mV/s. Potentials are reported vs Ag/AgCl.

Transient Absorption

The ultrafast transient absorption studies of [Cu(xantphos)(biq-COOH)]BF_4 were carried out in a 1mM solution of the Cu complex in two different solvents: DCM and MeOH excited at 400 nm, measured with a ~40 fs laser pulse. Figure 18 (a) and (c) show the obtained spectra for both samples with the appearance of a broad band in the range of 500 to 600 nm right after irradiation due to the excited state absorption, while contributions of the ground state bleaches seem to be below 400 nm.

In both samples, but more noticeable in the MeOH sample, there is a change in the spectra that appears in between 5 and 10 ps, this could be assigned to the intersystem crossing from the excited flattened state to the triplet state ($S_1 \rightarrow T_1$).[26]

Structural changes might be happening due to a Pseudo Jahn Teller distortion (the second order Jahn teller effect) right after the generation of the excited state S_2 resulting in a MLCT state with a flattened tetrahedral coordination, the relaxation of the excited state $S_2 \rightarrow S_1$ by internal conversion has been reported to happen at ~50 -100 fs.[26] The kinetic traces at selected wavelengths were fitted in Origin using the monoexponential decay function yielded the lifetime values of 473 ps for the solution in MeOH and 15 ps in DCM (Figure 18: b and d), that are assigned to the relaxation of the intersystem crossing (S1→T1).

The reported mechanism for photogeneration of the MLCT, propose that after the absorption of a photon an electron gets promoted form the Cu^{I} metal centre to the ligand, generating a Frank-Condon MLCT state with Cu^{II*} centre coordinated to one reduced neutral ligand, this has a pseudo-tetrahedral coordination geometry as the ground state. A difference from the Cu^{II*} which is susceptible to a Jahn-teller distortion this results on a MLCT state with a flattened tetrahedral coordination. This process normally happens in the range of the ns or microseconds.[35]

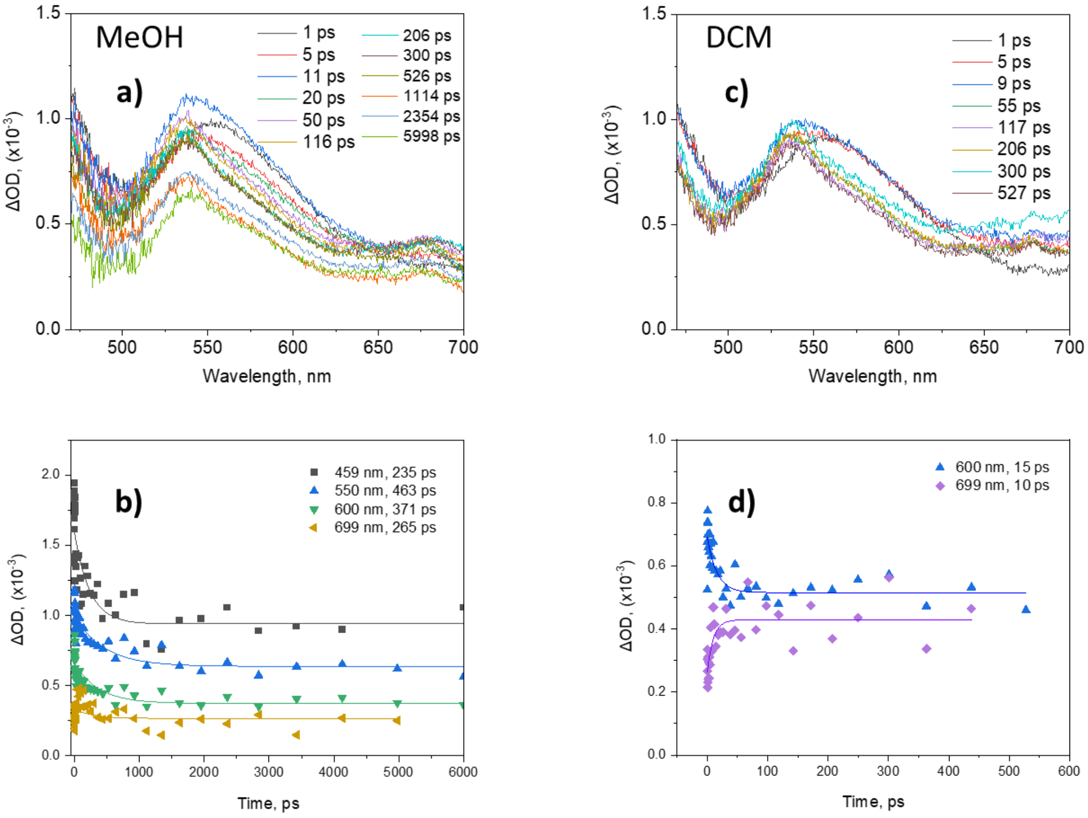

Figure 18. Transient absorption spectra of [Cu(xantphos)(biq-COOH)]BF_4 under 400 nm excitation. (a) Recoded in a 1mM MeOH solution. (b) kinetic traces in the MeOH solution from 0 to 6000 ps. (c) Spectra recoded in a 1mM DCM solution. (d) kinetic traces in DCM at stated wavelengths from 0 to 600 ps.

Additionally, the lifetime decay was measured by Time-correlated single-photon counting (TCSPC) in DCM (Figure 19), the obtained spectra was fitted in OriginPro® using a biexponential decay equation, the obtained values were : τ_1 = 11.0 ± 0.3 ns and τ_2 = 124 ± 3 ns, the longest one τ_2 is assigned to the relaxation of the triplet state back into the ground state (T1 → S_0) and (τ_1) could correspond to the intersystem crossing. The lifetime decay for the complex [Cu(xantphos)(biq)]tfpb in degassed dichloromethane is 410 ± 5 ns according with literature.[32] As the values obtained from degassed samples are longer due to quenching by oxygen we cannot compare directly our results with literature. Nevertheless, this value can be compared with modified [Cu(P^P)(N^N)]PF_6 complexes, which report excited state lifetimes in aerated dichloromethane in the range of 40 to 450 ns, confirming that the lifetime of [Cu(xantphos)(biq-COOH)]BF_4 is consistent with complexes of a similar structure.[25]

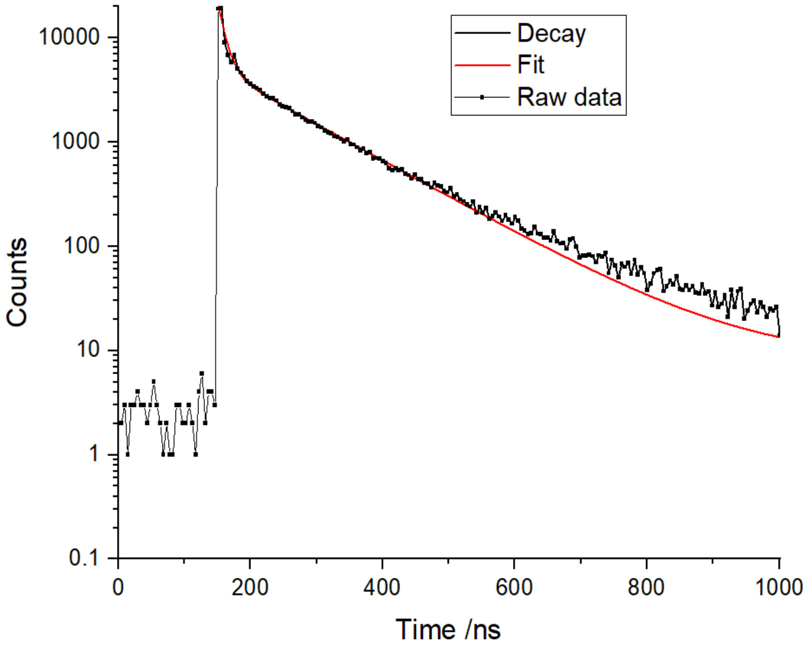

Figure 19. Time-correlated single-photon counting (TCSPC) spectra of [Cu(xantphos)(biq-COOH)]BF_4 recorded in DCM and fitted in Origin® using a biexponential decay equation, the obtained values were τ_1 = 11.0 $\pm$ 0.3 ns and τ_2 = 124 $\pm$ 3 ns.

5.5 Conclusions

In this chapter we presented the results obtained from the studies of the new copper complexes [Cu(xantphos)(biq-COOH)]BF_4 and [Cu(xantphos)(phen-COOH)]BF_4. Both complexes showed MLCT absorbance in the visible region, as desired and all had energy of the excited state (as estimated from emission maximum) than the value required water splitting. Both the UV-visible absorbance and emission spectra showed that the addition of carboxylic acid groups on to the biquinoline ligand shifted the energy of the ^{1}MLCT singlet and triplet excited states to lower energies (visible region). It's been reported that large stokes shift of the emission indicates a large structural changes occurs in the excited states, in this work we observed a shift of 360 nm for the [Cu(xantphos)(biq-COOH)]BF_4 complex and 270 nm for the [Cu(phen-COOH)$_2$]BF_4. This can give us an indication of a major distortion on the structure for the biquinoline complex.[36] The addition of the xantphos ligand significantly reduced the excited state lifetime and decreased the detectable emission from the copper complex. The $E_{1/2}$ value for the oxidation of Cu(I) in [Cu(xantphos)(biq-COOH)]BF_4 is more positive than that of the complex [Cu(biq-COOH)$_2$]BF_4 indicating that the *d*-orbital on Cu from which the MLCT transition occurs is at a lower energy in the former. This suggestion was supported by the energy of the MLCT absorption maximum, which occurred at a higher wavelength for [Cu(xantphos)(biq-COOH)]BF_4 than for [Cu(biq-COOH)$_2$]BF_4.[37] Lifetime decay of [Cu(xantphos)(biq-COOH)]BF_4 and their comparison with reported values are summarized in Table 1. Interestingly, [Cu(xantphos)(biq-COOH)]$^+$ possesses a sufficiently long excited state lifetime to make it suitable for its application as PS for sensitized films but not longer than other Cu complexes previously reported.

Table 1. Summary table of Cu complexes in solution

Complex	*Absorbance (MLCT) /nm	*Emission /nm	ΔE (^{3}MLCT-S$_0$) /eV**	Lifetime decay
[Cu(xantphos)(biq-COOH)]$^+$	485	690	1.80	124 ns$^{\text{(DCM)}}$
[Cu(xantphos)(phen-COOH)] $^+$	390	650	1.91	---
[Cu(I)(xantphos)(dmp)]tfpb[21]	378	550	---	0.064 μs$^{\text{(DCM)}}$
[Cu(dmp)(dppe)]$^{+e}$ [23]	400	630	---	1.33 μs$^{\text{(DCM)}}$
[Cu(xantphos)(dipp)]tfpb[38]		523	---	9.6 μs$^{\text{(DCM)}}$
[Cu(phen)(DPEphos)]$^+$ [39]	391	700	---	0.19 μs$^{\text{(DCM)}}$
[RuII(bpy)$_3$]$^{2+}$ [39]	450	650	---	0.85 μs$^{\text{(ACN)}}$
[Cu(dmp)$_2$]$^{+}$[40]	460	750	---	0.09 μs$^{\text{(DCM)}}$

*Absorbance and emission were recorded in DCM.

**CV values were recorded in dry Acetonitrile and reported against the Fc/Fc$^+$ pair.

5.6 References

1 S. Zhang, H. Ye, J. Hua and H. Tian, *EnergyChem*, 2019, **1**, 100015.

2 J. J. Concepcion, R. L. House, J. M. Papanikolas and T. J. Meyer, *Proc. Natl. Acad. Sci. U. S. A.*, 2012, **109**, 15560–15564.

3 S. N. H. Jaafar, L. J. Minggu, K. Arifin, M. B. Kassim and W. R. D. Wan, *Renew. Sustain. Energy Rev.*, 2017, **78**, 698–709.

4 P. Xu, N. S. McCool and T. E. Mallouk, *Nano Today*, 2017, **14**, 42–58.

5 L. Duan, A. Fischer, Y. Xu and L. Sun, *J. Am. Chem. Soc.*, 2009, **131**, 10397–10399.

6 L. Duan, F. Bozoglian, S. Mandal, B. Stewart, T. Privalov, A. Llobet and L. Sun, *Nat. Chem.*, 2012, **4**, 418–423.

7 T. Nakagawa, N. S. Bjorge and R. W. Murray, *J. Am. Chem. Soc.*, 2009, **131**, 15578–15579.

8 J. Lim, D. Park, S. S. Jeon, C. W. Roh, J. Choi, D. Yoon, M. Park, H. Jung and H. Lee, *Adv. Funct. Mater.*, 2018, **28**, 1–7.

9 Y. Lee, J. Suntivich, K. J. May, E. E. Perry and Y. Shao-Horn, *J. Phys. Chem. Lett.*, 2012, **3**, 399–404.

10 T. P. Brewster, J. D. Blakemore, N. D. Schley, C. D. Incarvito, N. Hazari, G. W. Brudvig and R. H. Crabtree, *Organometallics*, 2011, **30**, 965–973.

11 J. Hou, M. Fang, A. J. P. Cardenas, W. J. Shaw, M. L. Helm, R. M. Bullock, J. A. S. Roberts and M. O’Hagan, *Energy Environ. Sci.*, 2014, **7**, 4013–4017.

12 A. S. Weingarten, R. V. Kazantsev, L. C. Palmer, M. McClendon, A. R.

Koltonow, A. P. S. Samuel, D. J. Kiebala, M. R. Wasielewski and S. I. Stupp, *Nat. Chem.*, 2014, **6**, 964–970.

13 L. Gan, T. L. Groy, P. Tarakeshwar, S. K. S. Mazinani, J. Shearer, V. Mujica and A. K. Jones, *J. Am. Chem. Soc.*, 2015, **137**, 1109–1115.

14 B. C. M. Martindale, G. A. M. Hutton, C. A. Caputo and E. Reisner, *J. Am. Chem. Soc.*, 2015, **137**, 6018–6025.

15 and X. S. Jiahai Wang , Wei Cui , Qian Liu , Zhicai Xing , Abdullah M. Asiri, *Adv. Mater.*, 2016, **28**, 215–230.

16 J. Lai, A. Nsabimana, R. Luque and G. Xu, *Joule*, 2018, **2**, 76–93.

17 W. Wang, M. J. Nilges, T. B. Rauchfuss and M. Stein, *J. Am. Chem. Soc.*, 2013, **135**, 3633–3639.

18 S. Pullen, H. Fei, A. Orthaber, S. M. Cohen and S. Ott, *J. Am. Chem. Soc.*, 2013, **135**, 16997–17003.

19 D. L. D. and R. M. B. Tianbiao Liu, Xiaoping Wang, Christina Hoffman, *Angew. Chemie*, 2014, **53**, 5300–5304.

20 H. Lee, X. Wu and L. Sun, *Nanoscale*, 2020, **12**, 4187–4218.

21 M. V. Appleby, P. G. Walker, D. Pritchard, S. Van Meurs, C. M. Booth, C. Robertson, M. D. Ward, D. J. Kelly and J. A. Weinstein, *Mater. Adv.*, 2020, **1**, 3417–3427.

22 M. W. Blaskie and D. R. Mcmillin, *Inorg. Chem.*, 1980, 3519–3522.

23 D. G. Cuttell, S. M. Kuang, P. E. Fanwick, D. R. McMillin and R. A. Walton, *J. Am. Chem. Soc.*, 2002, **124**, 6–7.

24 and T. B. K. Mark T. Miller, Peter K. Gantzel, *J. Am. Chem. Soc*, 1999, 4292–

4293.

25 L. X. Chen, G. B. Shaw, I. Novozhilova, T. Liu, G. Jennings, K. Attenkofer, G. J. Meyer and P. Coppens, *J. Am. Chem. Soc.*, 2003, **125**, 7022–7034.

26 M. Iwamura, S. Takeuchi and T. Tahara, *Acc. Chem. Res.*, 2015, **48**, 782–791.

27 D. R. McMillin, J. R. Kirchhoff and K. V. Goodwin, *Coord. Chem. Rev.*, 1985, **64**, 83–92.

28 D. Pritchard, University of Shefffield, 2020.

29 S. Keller, Universität Basel, 2017.

30 F. R. Mansour, C. L. Kirkpatrick and N. D. Danielson, *J. Chromatogr. Sci.*, 2013, 51, 655–665.

31 A. M. Kranenburg, Y. E. M. Van Der Burgt, P. C. J. Kamer, P. W. N. M. Van Leeuwen, J. H. Van't Hoff, K. Goubitz and J. Fraanje, *New Diphosphine Ligands Based on Heterocyclic Aromatics Inducing Very High Regioselectivity in Rhodium-Catalyzed Hydroformylation: Effect of the Bite*, 1995, vol. 14.

32 B. J. McCullough, B. J. Neyhouse, B. R. Schrage, D. T. Reed, A. J. Osinski, C. J. Ziegler and T. A. White, *Inorg. Chem.*, 2018, **57**, 2865–2875.

33 N. Arnosti, M. Meyer, A. Prescimone, E. C. Constable and C. E. Housecroft, *Crystals*, 2021, **11**, 1–15.

34 S. Keller, A. Pertegás, G. Longo, L. Martínez, J. Cerdá, J. M. Junquera-Hernández, A. Prescimone, E. C. Constable, C. E. Housecroft, E. Ortí and H. J. Bolink, *J. Mater. Chem. C*, 2016, **4**, 3857–3871.

35 L. X. Chen, G. B. Shaw, I. Novozhilova, T. Liu, G. Jennings, K. Attenkofer, G. J. Meyer and P. Coppens, *J. Am. Chem. Soc.*, 2003, **125**, 7022–7034.

36 C. T. Cunningham, J. J. Moore, K. L. H. Cunningham, P. E. Fanwick and D. R. McMillin, *Inorg. Chem.*, 2000, **39**, 3638–3644.

37 E. Karkera, University of Sheffield, 2021.

38 C. S. Smith, C. W. Branham, B. J. Marquardt and K. R. Mann, *J. Am. Chem. Soc.*, 2010, **132**, 14079–14085.

39 P. Andrea and F. Cortés, .

40 C. A. Tolman, *Chem. Rev.*, 1977, **77**, 313–348.

Chapter 6

Sensitization of SC films for their application as photoanodes on water splitting.

This chapter describes the application of the previously studied (Chapter 5) Cu complexes for its application as PS on sensitized photoanodes for photoelectrochemical (PEC) water splitting. Using different preparation techniques for the films and evaluating the influence of these techniques in the optical and photophysical properties of the photoanodes. Additionally, we evaluate the performance of the different semiconductors, used as support for the photoanodes, proposed in this project: the Aluminates $MgAl_2O_4$:X (X : Ni, Cu) and TiO_2 as comparison.

6.1 List of Figures

6.2 Introduction

An APS is formed by a sensitizer and electron donor and an acceptor a difference from an artificial photosynthetic hybrid system for PEC water splitting is generally formed by the cathode where the proton reduction reactions have place (Eq. 2) and the photoanode where the water oxidation reaction happens (Eq. 1) (Figure 1).

$$2H_2O \rightarrow O_2 + 4H^+ + 4e^- \qquad \text{Eq. 1}$$

$$4H^+ + 4e^- \rightarrow 2H_2 \qquad \text{Eq. 2}$$

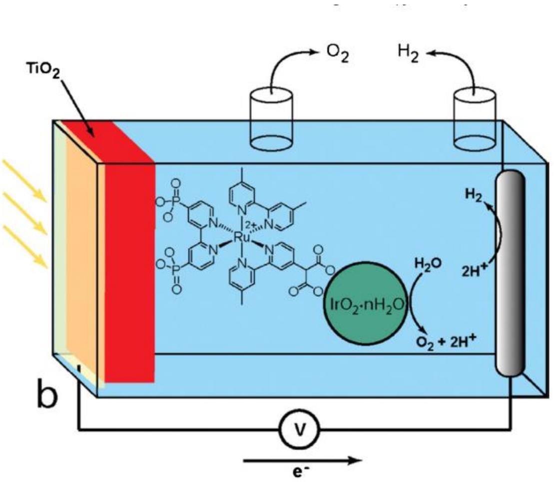

Figure 1. Schematic representation of a PEC Artificial Photosynthetic water splitting cell to generate hydrogen.

Sensitized photoanodes are composed by a semiconductor (SC) that acts as a support and a photosensitizer (PS) that acts as an antenna collecting the photons from the solar irradiation and transferring them into the SC conduction band to start the water splitting reactions to produce the hydrogen. This approach helps to compensate the negative effect of the recombination processes on the SC surface therefore increasing the efficiency of the SC and making it active under the visible irradiation (400 -700 nm).

When photosensitizer molecules on the TiO_2 or any other SC absorb incident photons from visible light, electrons (e^-) in the molecules become excited from the HOMO to the LUMO, consequently leaving electron holes (h^+) in the HOMO. If the LUMO energy level is higher than the CB of a corresponding photoelectrode, then the photoexcited electrons can be injected rapidly towards the VB and into the CB of a semiconductor (Figure 2)[1,2].

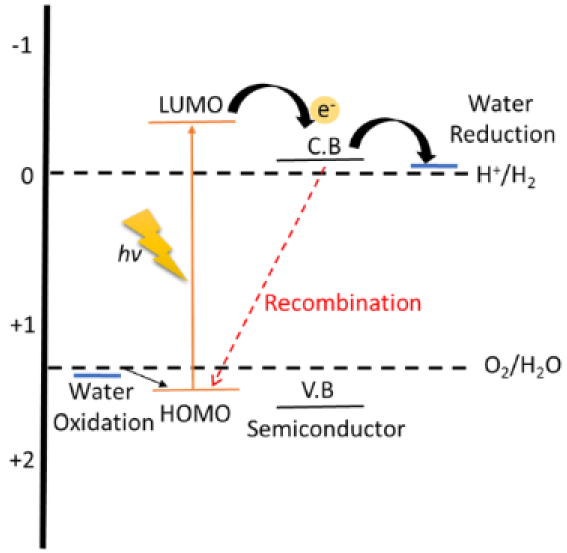

Figure 2. Schematic representation of the electron transfer between a SC and a PS in an artificial photosynthetic system using.

Anchoring groups

One of the characteristics that make a PS suitable for this application, is a long-lived emissive excited state. However, most of the complexes studied so far have a very short lifetime, which makes the electron transfer very inefficient between the PS and the SC. The efficiency can be increased by assembling the PS onto the surface of the SC. This will shift the absorbance to the visible region increasing the efficiency of the system.

One strategy used to anchor dyes on to semiconductor surface is the use of linkers that can form covalent attachment to the SC surface (Figure 3). The selection of the appropriate linker plays an important role in the development of new photoanodes, and it will depend on the system and their properties. This linker can provide a faster charge transfer between the SC and the PS, and the nature of their bonding can be influenced by the properties of the solvent used as different linker groups have different properties, for example the polarity, pH, and redox properties. Therefore, a good anchoring group would be resistant to this environment, such that it could provide strong adsorption between the photosensitiser and semiconductor and facilitate fast electron transfer. There are a lot of varieties of different anchoring groups that have been studied but the more commonly studied are carboxylic acids, phosphonic acids and siloxanes[3,4]. In case of the water splitting applications, the PS should be difficult to oxidise or hydrolyse under the conditions required for oxidising water.

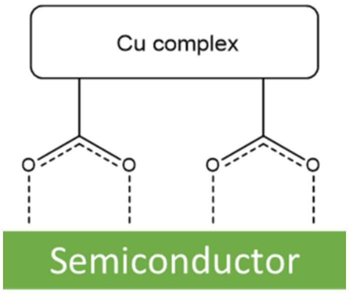

Figure 4. Representation of a PS assembled on to a SC surface using -COOH groups as linker.

This chapter describes the application of two novel copper complexes with a carboxylic group as a linker to be assembled on to the SC surface, and their application as PS in photoanodes for water splitting. The photophysical and electrochemical properties of sensitized $MgAl_2O_4$:X (X= Ni and Cu) and TiO_2 photoanodes are investigated for their application as APS for hydrogen production using the $[Cu(xantphos)(biq\text{-}COOH)]^+$ complex as the photosensitizer.

6.3 Experimental methods

Materials

Chemicals and solvents were purchased form Sigma Aldrich ® and the TiO_2 paste from Soleronix®.

Preparation of Semiconductor films

The films were prepared using two different deposition techniques: spin coating and Dr blade, spin coating gives thinner films more suitable for optical and electrochemical characterization in contrast with the ones prepared by Dr blade which gives ticker film. Two different substrates were used: silica glass and glass cover with a conductive film of ITO. This last one is for the electrochemical applications.

The first step was to prepare pastes of the SC studied and prepared by sol-gel, (described in Chapter 4), $MgAl_2O_4$:X (X : Ni, Cu), this was achieved by a modified version of the method described by Seigo, Ito and Gratzel for screen printing, described in Figure 5.[5]

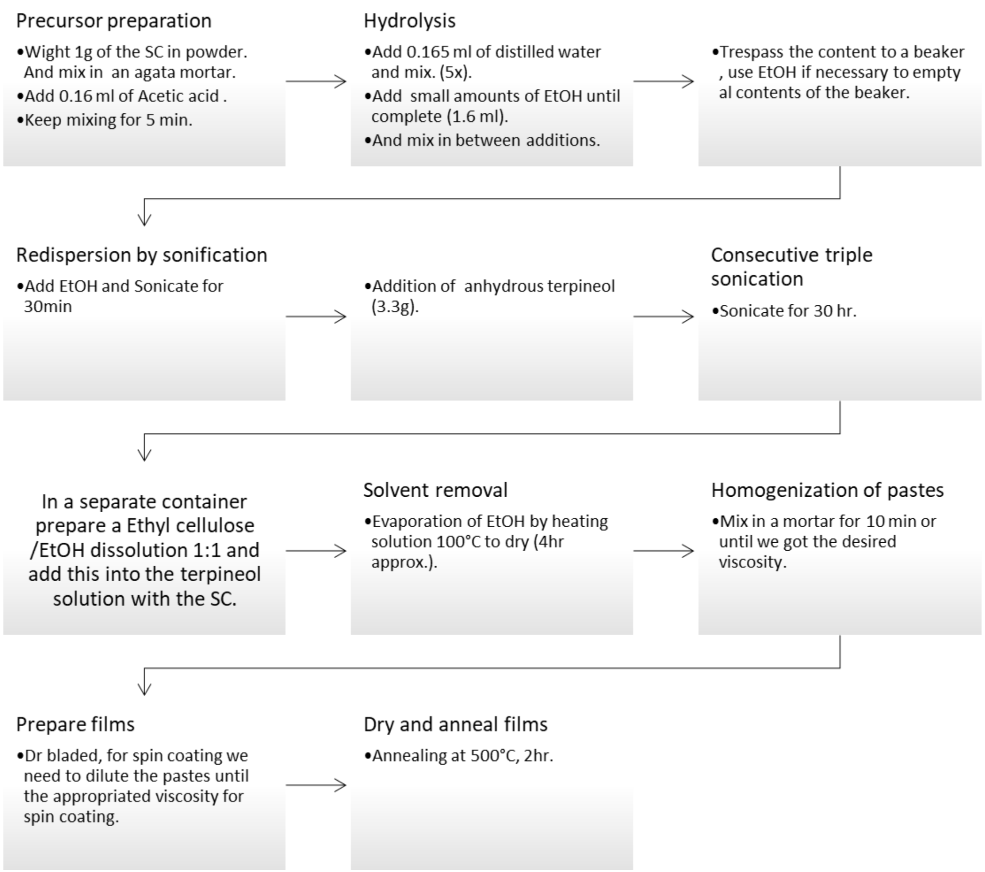

Figure 5. Flow diagram of the modified method used for the preparation of semiconductor pastes used to prepare the films.

Once the aluminates $MgAl_2O_4$:X (X : Ni, Cu) pastes were ready, the films were prepared by Dr Blade and Spin coating techniques. The last one was achieved in a vacuum-free Ossila® Spin Coater under the following conditions: 60 seg @2000 rpm 100µL of sample (Figure 6).[6] the samples were after annealed at 550 °C by 2 hr on air in a 3 litre 1600ºC RHF Carbolite® furnace.

Figure 6. Vacuum-free Ossila® Spin Coater used to prepare the films.

Sensitization of films

From the Cu complexes studied in chapter 5 we selected [Cu(xantphos)(biq-COOH)]$^+$ to sensitize the films by dipping the previously annealed films in an 1M solution of the [Cu(xantphos)(biq-COOH)]$^+$ in methanol. The films were soaked in the solution overnight and then rinsed with deionised water and dried at room temperature in air for their characterization (Figure 7).

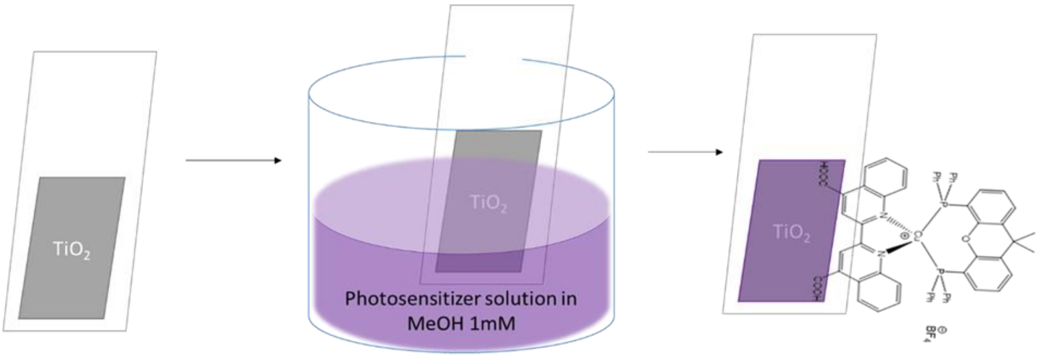

Figure 7. Schematic representation for the procedure used for sensitizing the films. Using *silica glass and glass/ITO coated with the semiconductor films prepared by screen print and spin coating.*

6.4 Characterization

The prepared films were characterized by spectroscopic and electrochemical techniques.

The **Absorption** spectra of the films were recorded in a Cary 5000 NIR-UV-Vis Spectrometer in function of the Reflectance and in Abs modes from 200 to 800 nm.

Scanning Electron Microscopy and EDS

Samples were deposited on silicon wafers, dried in air for 6 h, and coated with 2 nm of platinum using a Cressington 328 Ultra High-resolution EM Coating System. The images were obtained using an FEI Helios NanoLab DualBeam microscope in immersion mode, with beam settings of 1.5 kV and 0.17 nA.

Atomic Force Microscopy

Atomic force microscopy images were recorded using a Bruker Multimode 5 atomic force microscope, operating in soft-tapping mode in air under standard ambient temperature and pressure, fitted with Bruker OTESPA-R3 silicon cantilevers operated with a drive amplitude of ~18.70 mV and resonance frequency of ~236 kHz. Samples were prepared by placing the film over the metallic holder with a carbon tape. Images were processes using Gwyddion software.

Emission spectroscopy. All spectra were recorded using a Horiba Jobin-Yvon Fluoromax-4 spectrofluorometer.

Photocurrent ON-OFF was recorded in an Autoloab® STAT100 potentiostat. a conventional 3-electrodes cell is used, with an Ag/AgCl electrode as a reference, Pt as counter electrode and a glassy-carbon as working electrode (figure). Using a TBAPF6 0.2M as electrolyte in dry acetonitrile, and with a concentration of the compound studied of 1 mM; this concentration should be sufficient to avoid large ohmic voltage losses across the electrolyte.

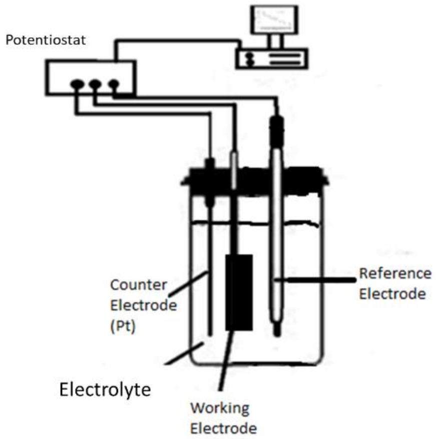

Figure 8. Simplified scheme of an Electrochemical 3-electrode arrange cell.

Femtosecond Transient Absorption (TA) spectroscopy was performed at the Lord Porter Laser Laboratory, University of Sheffield. A Ti:Sapphire regenerative amplifier (Spitfire ACE PA-40, Spectra-Physics) provided 800 nm pulses (40 fs FWHM, 10 kHz, 1.2 mJ). 400 nm pulses for excitation were generated by doubling a portion of the 800 nm output in a β-barium borate crystal within a commercially available doubler/tripler (TimePlate, Photop Technologies). White light supercontinuum probe pulses in the range 340–790 nm, were generated by tightly focusing ca. 1 µJ of the 800 nm output on a CaF2 crystal (continuously displaced to avoid damage). Detection was achieved using a commercial transient absorption spectrometer (Helios, Ultrafast Systems) using a 2048-pixel CMOS sensor for the UV-vis spectral range. The relative polarisation of the pump and probe pulses was set to the magic angle of 54.7˚ for anisotropy-free measurements. Samples were held in 2 mm path length quartz cells and were stirred during experiments. The optical density at the excitation wavelength was kept at approximately 0.5. The optical density across the probe range was kept below 1.0. Excitation energies were kept below 2 µJ.

6.5 Results

Preparation of the films

As described in the methods section, films were prepared using Dr Blade and Spin coating techniques to evaluate the influence of the method on the thickness of the films and their optical properties.

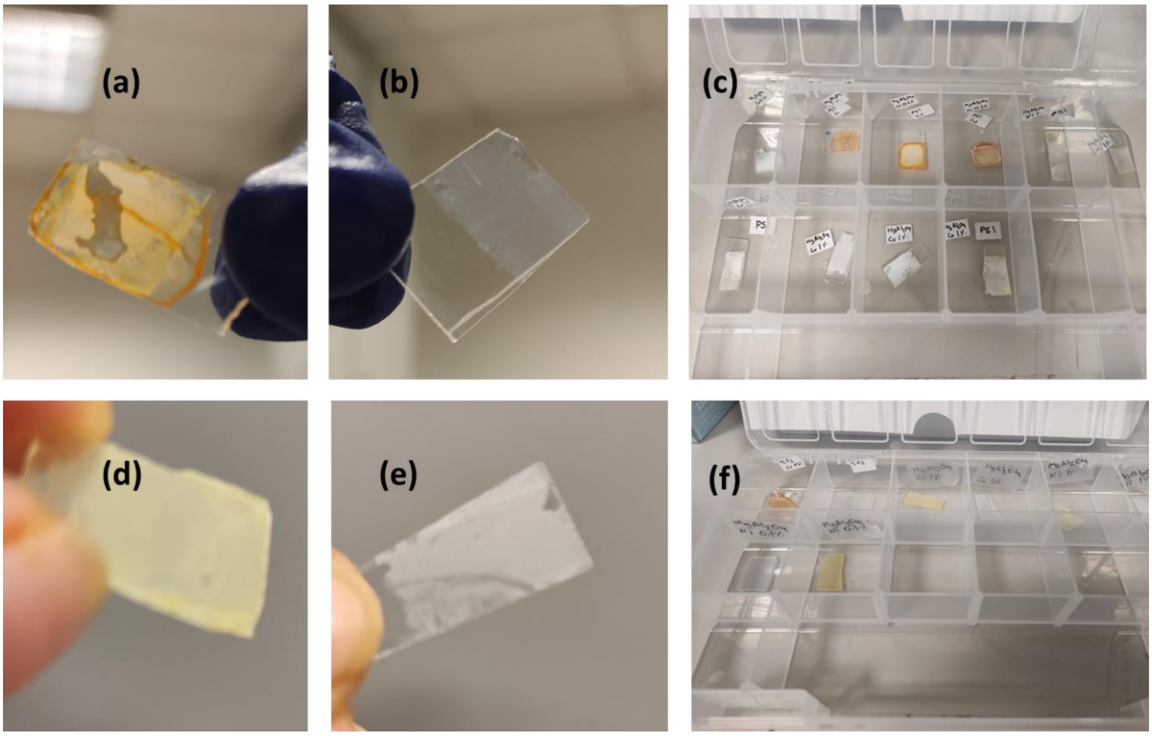

Figure 9. Films prepared by Dr blade (c, d and e) and Spin coating techniques (a, b and f). (a) TiO_2 sensitized with $[Cu(xantphos)(biq\text{-}COOH)]^+$ (b) TiO_2 without sensitizer (d) $MgAl_2O_4$ 0.1% Ni with $[Cu(xantphos)(biq\text{-}COOH)]^+$ and (e) $MgAl_2O_4$ 0.1% without PS.

From chapter 4 the aluminates with the best photophysical characteristics and photocatalytic performance were selected for use as sensitized photoanodes. These were the samples with 0.1% of the dopant. Figure 9, shows the prepared films where we can observe clearly that the films prepared with Dr Blade technique (c and d) are much thicker than the ones prepared by spin coating (a and b) which normally leads to thin films. Also, the films were not very uniform by visual inspection.

SEM/EDS

The micrographs of the prepared films were taken to understand the effect of the morphology and composition on the films. The results showed the presence of Ni and Cu in doped samples detected by EDS analysis of the surface.

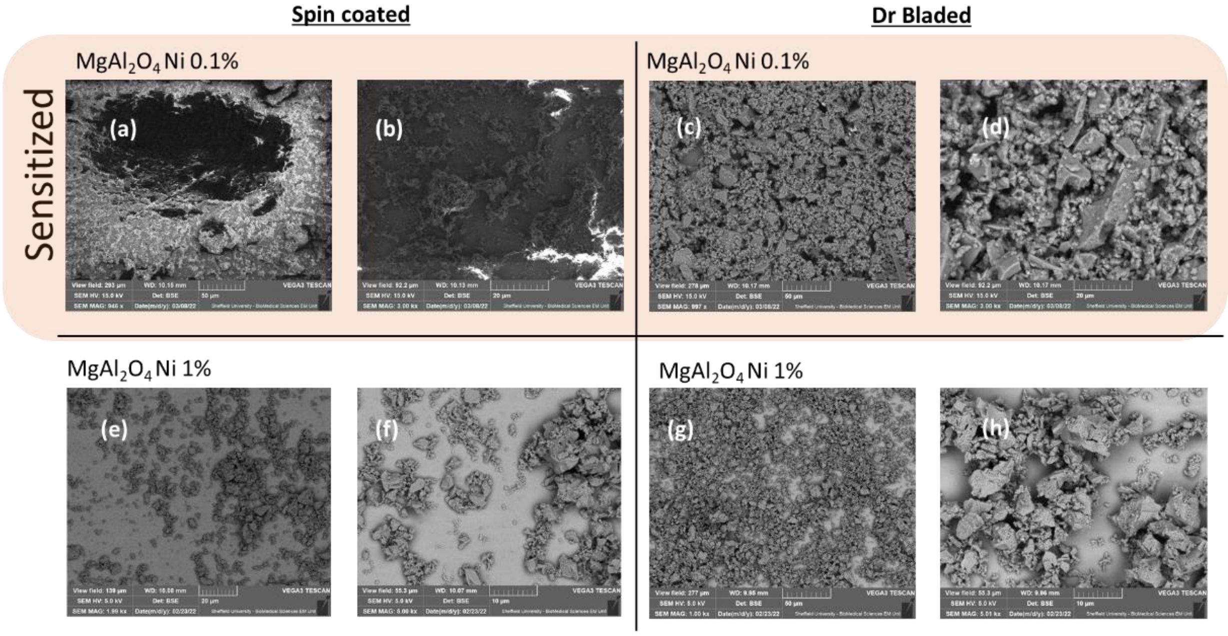

Figure 10. SEM images of the films prepared by Dr blade (right side) and Spin coating (left side). Sensitized samples (orange highlighted area). $MgAl_2O_4$ Ni 0.1% (a) 50 μm (b) 20 μm and (c) 50 μm and (d) 20 μm.

Figure 10 shows that generally the samples prepared by spin coating shown films are less crowded with visible empty spaces without any particles of the semiconductor. Also, there are some agglomerations of the particles in some parts. The average particle size for these samples is about 2 μm. In contrast, the samples prepared by Dr Blade technique the images look a bit more uniform and populated, this means that there is a higher amount of deposited semiconductor which is easy to detect by simple eye and was expected to have thinner films with spin coating and thicker ones with Dr Blade.

This can be explained due to a different concentration of the nanoparticles on the suspension used to prepare the films.

The EDS analysis (Figure 11) shows the presence of Ni in the sample $MgAl_2O_4$ doped with Ni 0.1 wt%. Cu was detected over the agglomerated areas, this can corroborate the presence of the $[Cu(xantphos)(biq\text{-}COOH)]^+$ on those areas, therefore we can say that those agglomerated particles correspond to the PS.

Other elements such as Mg, Al, O were detected those corresponds to the aluminate. Some contamination was also detected in much less amount such as F, Na, P and Fe and Cr, often present to the similarity on energy (eV) with some of the other elements present in the analysed area.

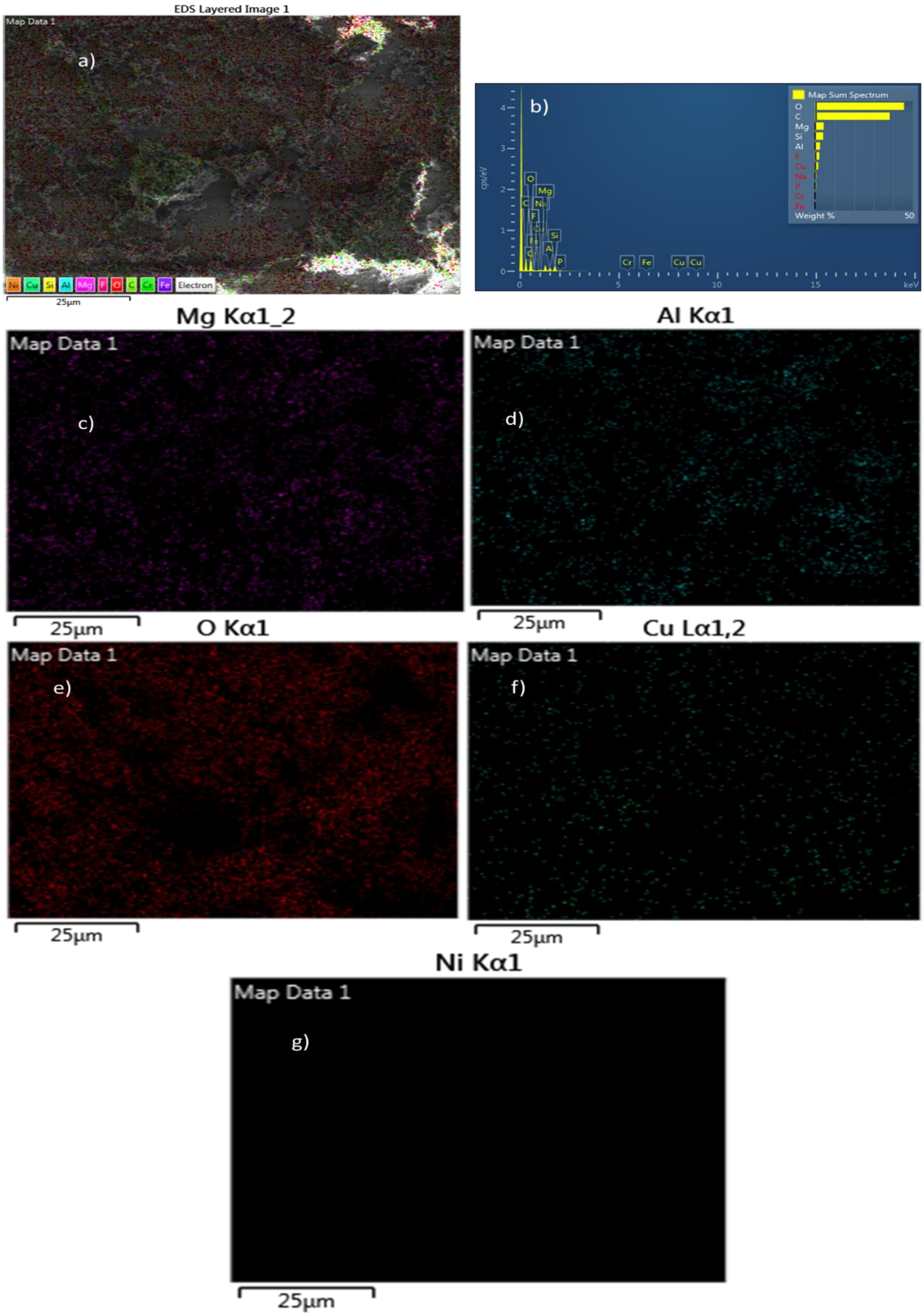

Figure 11. EDS analysis of the film $MgAl_2O_4$ Ni 0.1% prepared by Dr Blade and sensitized with $[Cu(xantphos)(biq\text{-}COOH)]^+$. a) EDS layered map b) Map spectrum of selected area. c) Mg d) of Al e) O f) Cu g) Ni.

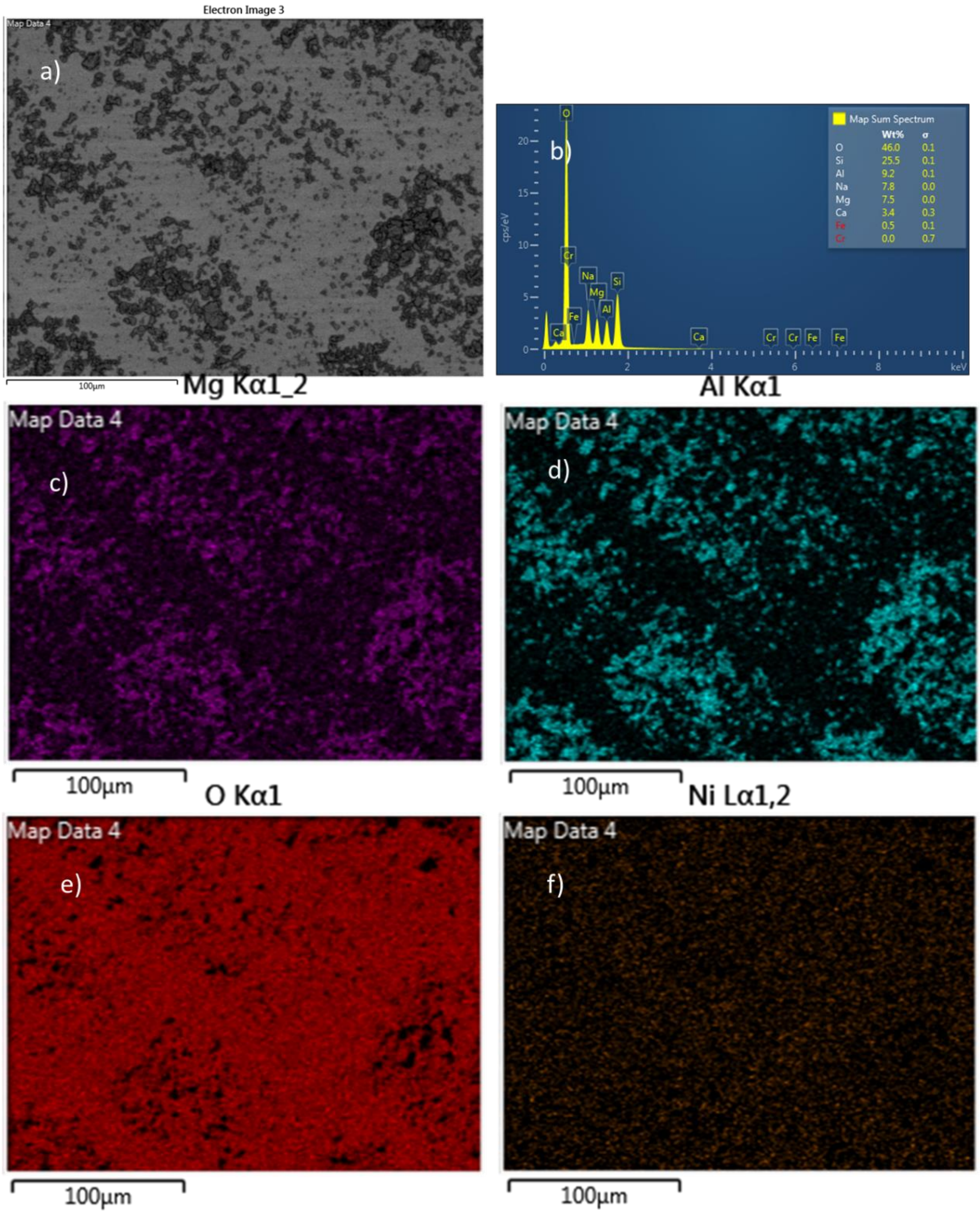

Figure 12. EDS analysis of the film $MgAl_2O_4$ Ni 0.1% prepared by Spin coating and without sensitizer a) EDS layered map b) Map spectrum of selected area. c) Map of Mg d) map of Al e) map of O f) map of Ni.

Figure 12 shows the results obtained for the sample $MgAl_2O_4$ Ni 0.1% prepared by spin coating without PS. This analysis confirms the presence of Mg, Al and O corresponding to the SC film and Ni was detected in a lower amount on the mapping but not in the spectrum which can be due to the low concentration in the sample.

Atomic Force Microscopy

AFM images were taken in an AFM Bruker® Multimode 5 in tapping mode. Figure 13, shows the images taken for the samples $MgAl_2O_4$ Ni 0.1% prepared by Spin coating and Dr Blade.

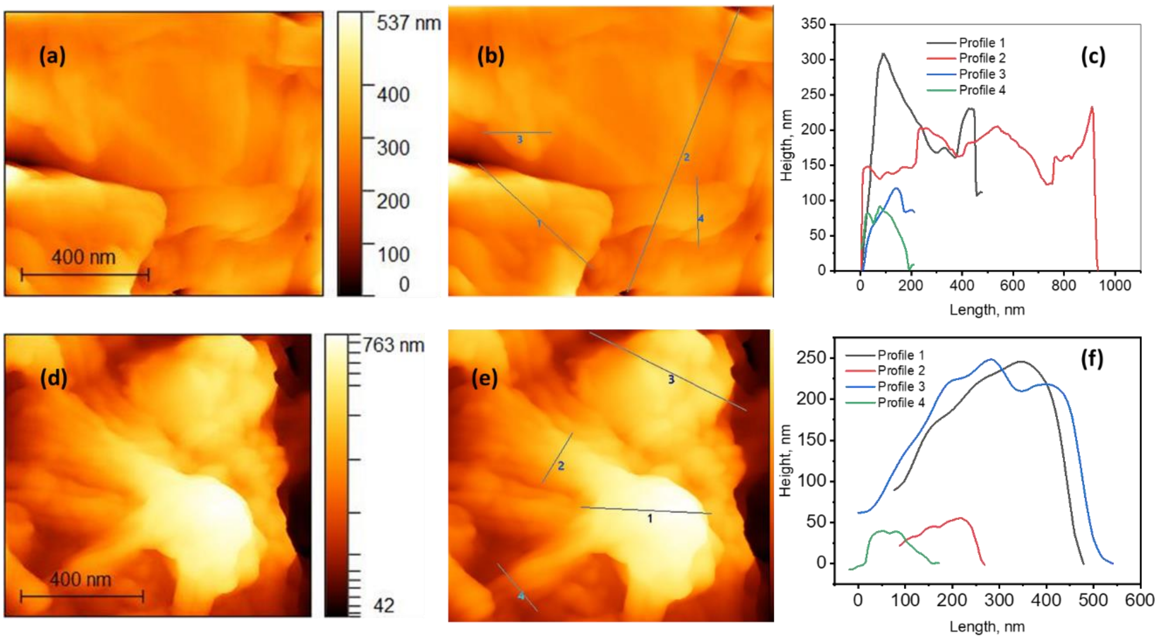

Figure 13. Transmission electron micrograph of the films $MgAl_2O_4$ Ni 0.1% **(a)** Dr Bladed film at 400 nm **(b)** selection of profiles. **(c)** Profiles graph. $MgAl_2O_4$ Ni 0.1% sensitized with Cu(xantphos)(biq-COOH) and prepared by **(d)** spin coating 400 nm and its corresponding **(e)** selection of profiles and **(f)** profiles graph.

The results of AFM confirm that the films prepared by Blade are thicker than the ones spin coated. Nanoparticles on the size of 800 nm length by 300 nm height for the DB sample were found. For the spin coated sample a maximum particle size of 500 nm length by 200 nm height was found. As expected, the samples with a bigger thickness where the ones prepared by Dr Blade.

UV Vis absorption

The UV Vis recorded spectra of the sensitized films prepared by spin coating shows a maximum absorption band at 480 nm, which corresponds to the MLCT band of the [Cu(xantphos)(biq-COOH)]$^+$ complex (Figure 14). The presence of this band indicates that the complex is assembled on to the surface of the film shifting the overall absorption of the films to the visible region.

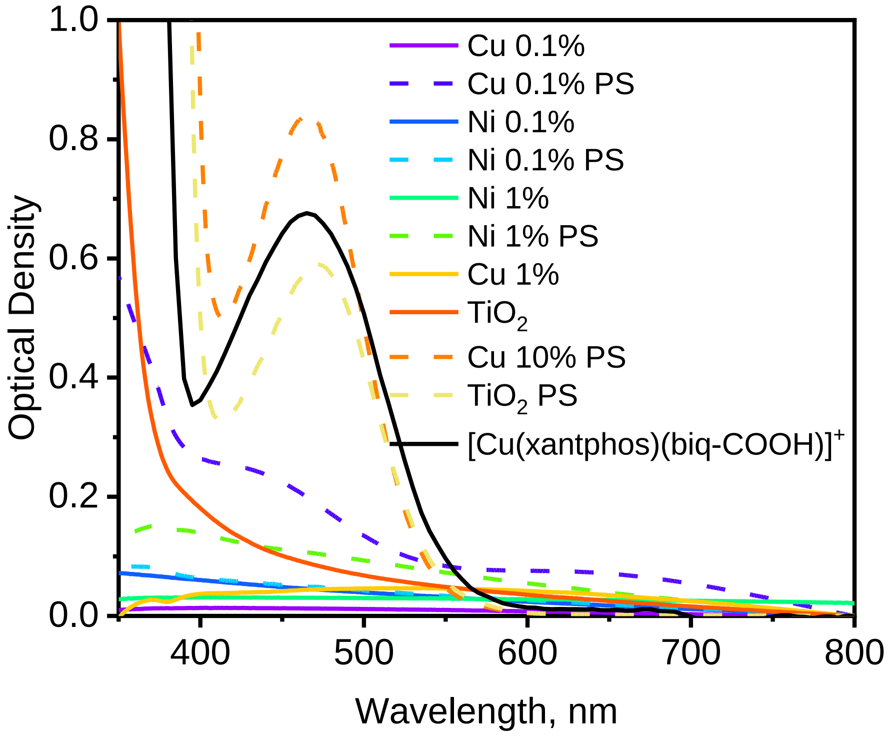

Figure 14. Absorption spectra of the sensitized films, prepared by spin coating and sensitized with [Cu(xantphos)(biq-COOH)]$^+$ in a 1M methanol solution. (Black line) [Cu(xantphos)(biq-COOH)]$^+$ solution in methanol, dotted line represents the sensitized films and straight lines the semiconductors without PS.

The films prepared with the Dr Balde technique were visible much thicker (Figure 9), therefore was not possible to record the UV visible spectrum by absorbance. Due to this the samples were recorded as function of the reflectance F(R). Figure 15 shows the results obtained for the sensitized films prepared by Dr Blade technique, only the samples doped with Ni 0.1%, Cu 0.1% and TiO_2 were successfully sensitized. This can be confirmed by the presence of the band at 450 which corresponds to the MLCT band of the [Cu(xantphos)(biq-COOH)]$^+$ and additional band was detected in both figures this broad band that appears from 600 to 750 nm could be due to the d-d transitions of the dopant Cu and Ni, also this peak is more intense in the aluminate samples in comparison with the TiO_2, this is in accordance with the absorbance spectra collected for the doped aluminates (reported in Chapter 4).

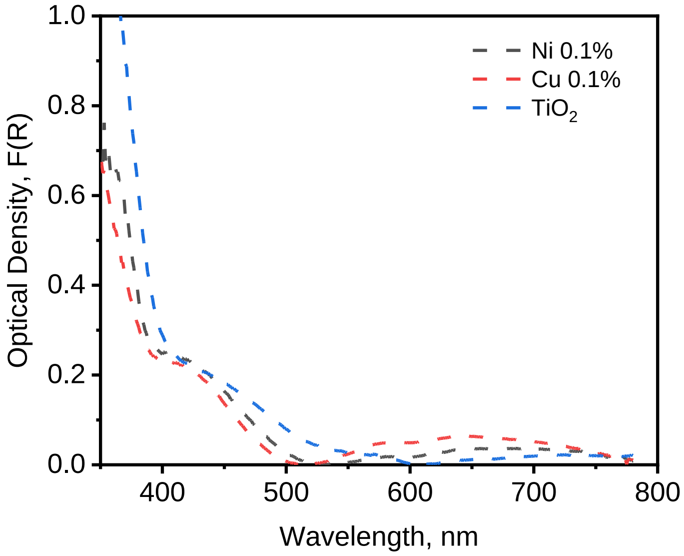

Figure 15. Absorbance spectra recorded in F(R) of the sensitized films prepared by Dr Blade technique and sensitized with [Cu(xantphos)(biq-COOH)]+ in a 1M methanol solution.

Emission

The emission of the films was recorded in function of the reflectance and in transmittance modes as well as the [Cu(xantphos)(biq-COOH)]$^+$ in methanol. Figure 16 shows the spectra where we can observe clearly a significantly reduction on the emission intensity of the films in comparison with the [Cu(xantphos)(biq-COOH)]$^+$ in solution.

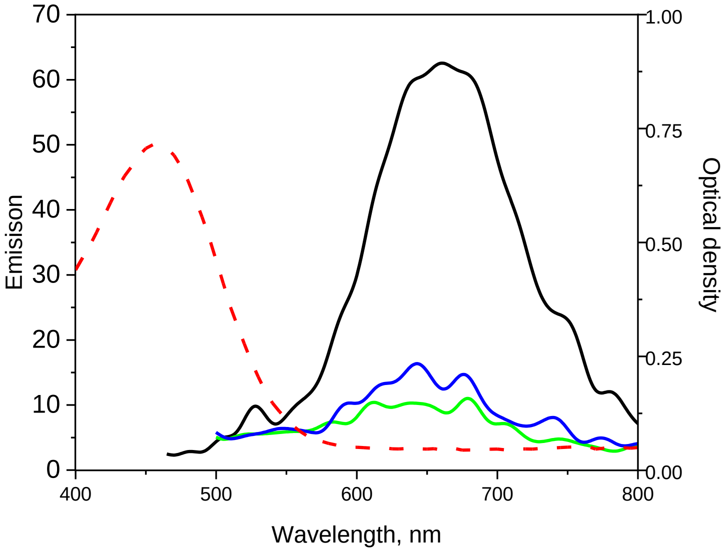

Figure 16. Emission spectra of [Cu(xantphos)(biq-COOH)]$^+$ recorded in methanol (black line). Sensitized films prepared by spin coating, $MgAl_2O_4$ Cu 10% at 1000 rpm (blue line) and $MgAl_2O_4$ Cu 10% at 400 rpm (green line). Absorption spectra of films [Cu(xantphos)(biq-COOH)]$^+$ recorded in methanol (red dash line)

This results shown that the presence of the [Cu(xantphos)(biq-COOH)]$^+$ is quenching the emission this because of the electron transfer from the excited states of the [Cu(xantphos)(biq-COOH)]$^+$ to the conduction band of the semiconductor.

Transient Absorption

Time resolved pump and probe studies are a key tool to understand the carrier dynamics that underline photocatalytic processes. For the ultrafast transient absorption studies on the selected films, sensitized and unsensitized TiO_2 was used as reference due to the low absorbance of the sensitized aluminate films. Analysis was carried out in by placing the sample in the sample holder and recording the absorbance in transmittance mode. Obtained spectra shown a broad band in the range of 400 to 600 nm after irradiation with 400 nm, ~40 fs laser pulse (Figure 17).

Figure 17 (a) shows the spectra of TiO_2 without any PS, whereas no absorption bands were observed, even when the UVVIS absorption in the ground state spectra show and very low absorption at 400 nm (OD_{max} 0.2), the TA analysis didn't show any broad TA bands after 400 nm irradiation because of the low absorption of TiO_2 under visible light.[7]

(c) shows the kinetic traces at selected wavelengths pf TiO_2 sensitized with $[Cu(xantphos)(biq\text{-}COOH)]^+$ (PS1). The kinetics fitted in Origin using the tri exponential decay function yielded the lifetime values for the films (τ_1 <1 ps, τ_2 250 ps and τ_3 >2000 ps). Other works have reported the TA analysis of TIO_2 doped and non-doped with an exponential decay of 360 ps for the undoped TiO_2.[7] Nonetheless, most of this studies use excitations on the UV region (330 – 360 nm),[8,9] more commonly used excitation at 355 nm which is the main band absorption for TiO_2.

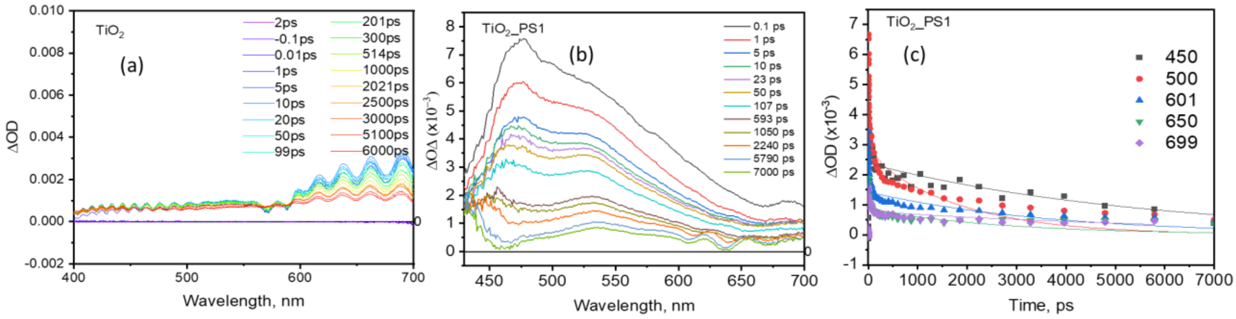

Figure 17. Transient absorption spectra of TiO_2 film prepared by Spin coating and sensitized with $[Cu(xantphos)(biq\text{-}COOH)]^+$ under 400 nm excitation.(a) TiO2 without PS (b) TiO_2/PS1 (c) kinetic traces 0 to 7000 ps.

After excitation the instant formation of free charge carriers happened, this carriers are trapped near the surface sites very rapidly. The spectroscopy signature of this free and trapped carriers has been studied by Yoshihara et al. who showed that this response is mainly compose by three components, trap holes (TH), trapped electrons

(TE) and free electrons in the conduction band (FE).[10] The rise time of signals related to this components allows us to explore the trapping dynamics of the charge carriers. The values reported in literature are relatively similar ~180 fs,[11] ~260 fs[12] and ~170 fs.[13] However, since this signals are superimposed, it is not clear the assignation of this times to the physical processes.

After the initial formation, the TE and FE decay by various processes on timescales of 10 to 100 s of ps or more, depending on the carrier density. In case of the TH timescales different values has been reported ~220fs[12] and <50 fs.[12]

Reported spectra found in literature shows a broad band at from 400 to longer wavelengths (1600nm) with a long live excited state.[14] In comparison with the spectra in this work looks quite similar, this could be because explained because as the excitation is at 400 nm we are exciting the PS MLCT band, and the generated excited e^- form the Cu complex, instead of relax into the ground state are been injected into the TiO_2 CB then these electrons will decay to ground state (VB), giving the same shape of the spectra because this transitions in TIO_2 doesn't change but the electron source does, they come from injection from the LUMO of the PS. according with this we assigned the calculated values in this work as its follows: τ_1 <1 ps is assigned to the TH process in the TiO_2 surface, and τ_2 250 ps to the electron injection from the LUMO to the CB and τ_3 >2000 ps are assigned to the retarded recombination process.

This results of sensitized TiO_2 presented int his work, in comparison with the values obtained for the $[Cu(xantphos)(biq\text{-}COOH)]^+$ in solution, shown a big increase in the lifetime decay to when the Cu complex is assembled on to the SC surface and this has been reported to be due to the electron injection form the LUMO of the PS into the CB of the SC, retarding the recombination charge of the excited charges of the PS.

In contrast with the results obtained for the sample of TiO_2 the $MgAl_2O_4$ Cu 0.1% sensitized didn't show any intense signals (above 0.0015) after the 400 nm excitation, this can be due to the lack of absorbance at 400 nm, as it was shown on the UV Vis absorbance the aluminate samples didn't get a good assembly of the PS to the SC surface this can be due to different factors one can be the protonation of the surface this passivate the surface preventing the binding to happen. Also, could be the poor availability of oxygen in the surface that can form enlaces with the -COOH groups of the PS.

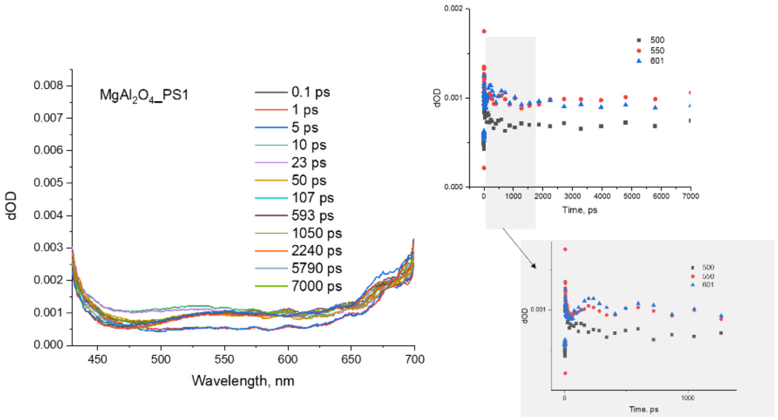

Figure 18. Transient absorption spectra of $MgAl_2O_4$ Cu 0.1% film prepared by Spin coating and sensitized with Cu(xantphos)(biq-COOH) under 400 nm excitation. (a) Recoded in absorbance mode. (b) kinetic traces 0 to 7000 ps.

6.6 Conclusions

This chapter has presented the results obtained for the application of the complex $[Cu(xantphos)(biq\text{-}COOH)]^+$ and its assembly on to different semiconductors $MgAl_2O_4$ Ni 0.1%, $MgAl_2O_4$ Cu 0.1% and TiO_2. The films were prepared by two different techniques and the results showed that the films prepared with spin coating presented better optical characteristics and were easier to analyze by TA. The Absorption analysis showed that the method used for sensitizing the films worked. Nevertheless, there was a big impact in the preparation of the films that affected the assembly of the PS on the SC, emission results confirm the ET between the PS and the SC in the analysed samples. Additionally, the TA results showed an improvement in the lifetime decay of the PS when it is assembled onto a SC surface in comparison to when it is in solution increasing from 200 to 2000 ps, retarding the recombination processes that occur on the SC surface (Figure 19). These results suggest the potential application of the [Cu(xantphos)(biq-COOH)]$^+$ assembly on TiO_2 and its application as photoanode for water splitting. Further studies should be conducted to understand the effect on the different factors studied in this work, unfortunately due to the COVID affectations we were unable to complete with the established goals (See Appendix C-COVID form).

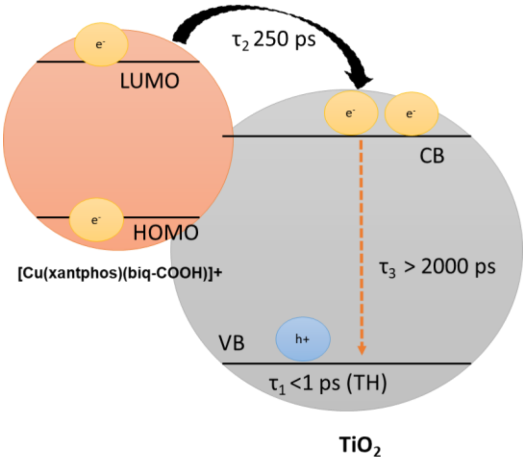

Figure 19. Proposed electron transfer mechanism of TiO_2 film sensitized with [Cu(xantphos)(biq-COOH)]$^+$.

6.7 References

1 K. Maeda, *J. Photochem. Photobiol. C Photochem. Rev.*, 2011, **12**, 237–268.

2 S. N. H. Jaafar, L. J. Minggu, K. Arifin, M. B. Kassim and W. R. D. Wan, *Renew. Sustain. Energy Rev.*, 2017, **78**, 698–709.

3 W. D. Zabka, T. Musso, M. Mosberger, Z. Novotny, R. Totani, M. Iannuzzi, B. Probst, R. Alberto and J. Osterwalder, *J. Phys. Chem. C*, 2019, **123**, 22250–22260.

4 A. Baktash, B. Khoshnevisan, A. Sasani and K. Mirabbaszadeh, *Org. Electron.*, 2016, **33**, 207–212.

5 S. Ito, T. N. Murakami, P. Comte, P. Liska, C. Grätzel, M. K. Nazeeruddin and M. Grätzel, *Thin Solid Films*, 2008, **516**, 4613–4619.

6 T. Allison, *Gravure*, 2007, **21**, 32–35.

7 G. Rossi, L. Pasquini, D. Catone, A. Piccioni, N. Patelli, A. Paladini, A. Molinari, S. Caramori, P. O'Keeffe and F. Boscherini, *Appl. Catal. B Environ.*, 2018, **237**, 603–612.

8 Guido Rothenberg, Jacques Moser, Michael Gratzel, Nick Serpone and Devendrá K. Sharma, *J. Am. Chem. Soc.* , 1985, **107**, 8054–8059.

9 N. Serpone, D. Lawless and R. Khairutdinov, *Size Effects on the Photophysical Properties of Colloidal Anatase T1O2 Particles: Size Quantization or Direct Transitions in This Indirect Semiconductor?*, 1995, vol. 99.

10 T. Yoshihara, R. Katoh, A. Furube, Y. Tamaki, M. Murai, K. Hara, S. Murata, H. Arakawa and M. Tachiya, *J. Phys. Chem. B*, 2004, **108**, 3817–3823.

11 D. E. Skinner, D. P. Colombo, J. J. Cavaleri and R. M. Bowman, *Femtosecond*

Investigation of Electron Trapping in Semiconductor Nanoclusters, 1995, vol. 99.

12 X. Yang and N. Tamai, *Phys. Chem. Chem. Phys.*, 2001, **3**, 3393–3398.

13 Y. Tamaki, A. Furube, M. Murai, K. Hara, R. Katoh and M. Tachiya, *Phys. Chem. Chem. Phys.*, 2007, **9**, 1453–1460.

14 R. Katoh, M. Murai and A. Furube, *Chem. Phys. Lett.*, 2010, **500**, 309–312.

CONCLUSIONS AND RECOMMENDATIONS FOR FUTURE WORK

At the beginning for this thesis, established the research questions that wanted to answer with this research project, and we will answer to each of one in this section.

In Chapter 3 we wanted to evaluate the effect of the ligand of the newly synthesized [FeFe] complex on the photophysical and electrochemical properties and their performance as catalyst for proton reduction.

The results showed that the inclusion of an additional aromatic ring in the new complex $Fe_2(dpet)(CO)_6$ decreases its reduction potential relative to $Fe_2(bdt)(CO)_6$ (making it less negative), making the complex easier to reduce and therefore more suitable for hydrogen evolution.

Chapter 4 reports the use of Ni and Cu as co catalyst in the $MgAl_2O_4$ semiconductors, the effect on their photophysical properties and how will this affect the position of the energy bands, therefore their performance for water splitting.

With the conducted research we can confirm that the addition of Cu and Ni have an impact in the photophysical properties shifting the absorbance to the visible light but also modifying the position of their CB and VB bands, make than more suitable for electron injection from our photosensitiser. Additionally, we measured the hydrogen evolution of the samples and even when they are not more efficient than their samples without dopants, they do have photocatalytic activity and now they are suitable to be used as support for the PS for their application as photoanodes, which is the overall goal of this thesis.

In Chapter 5 we studied the stability, electrochemical and photophysical properties of the new Cu complexes. Finding that both complexes studied in this project: [Cu(xantphos)(biq-COOH)]BF_4 and [Cu(biq-COOH)$_2$]BF_4 showed MLCT absorbance in the visible region, as desired and all had energy of the excited state (as estimated from emission maximum) than the value required water splitting. The $E_{1/2}$ value for the oxidation of Cu(I) in [Cu(xantphos)(biq-COOH)]BF_4 is more positive than that of the complex [Cu(biq-COOH)$_2$]BF_4 indicating that the *d*-orbital on Cu from which the MLCT transition occurs is at a lower energy in the former. This suggestion was supported by the energy of the MLCT absorption maximum, which occurred at a higher wavelength for [Cu(xantphos)(biq-COOH)]BF_4 than for [Cu(biq-COOH)$_2$]BF_4.[258] Interestingly, [Cu(xantphos)(biq-COOH)]$^+$ possesses a sufficiently long excited state lifetime in MeOH to make it suitable for its application as PS for sensitized films.

In Chapter 6 contains the results of the films prepared by spin coating and Dr blade techniques, sensitized with the [Cu(xantphos)(biq-COOH)]BF_4 complex and their characterization by SEM, EDX, AFM, UV Vis Absorbance, emission, and TA. The results show their potential application for Hydrogen evolution via PEC.

Future work

Unfortunately, due to COVID-19 restrictions and the time we weren't allowed to go into the laboratories we couldn't complete all the objectives from chapter 6 that we planned. Detailed description in Appendix C. Additionally, I would like to mention some considerations to future work and plans for future.

Further studies on the electron transfer mechanism between the Cu complexes and the SC when those are assembled on the surface of the SC to understand the effect of different factors like the different amount of dopant in the SC film or the preparation method. Stablish the type of binding of the PS assembled on the surface of the SC studied in this project. The overall impact of this factors on their performance as photoanodes for PEC water splitting.

And propose a ET mechanism for the hybrid system “Semiconductor – Photosensitiser – Hydrogenase” and evaluate its efficiency for H_2 PEC evolution.

APENDIX A-C3
Supporting Information
Chapter 3

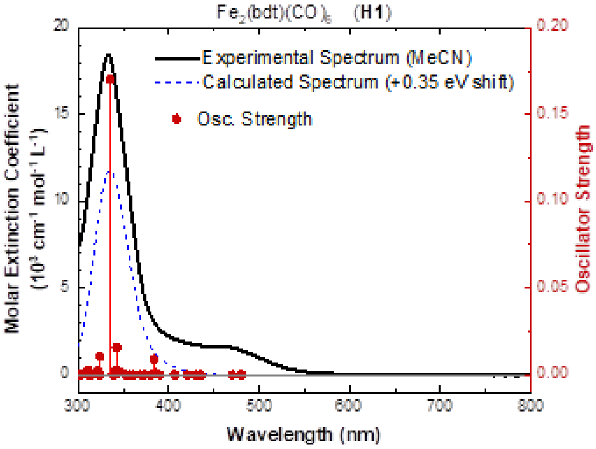

Fig. S3: Experimental (black solid line) and calculated (dashed line and red sticks) UV-Vis absorption spectra of complex H1.

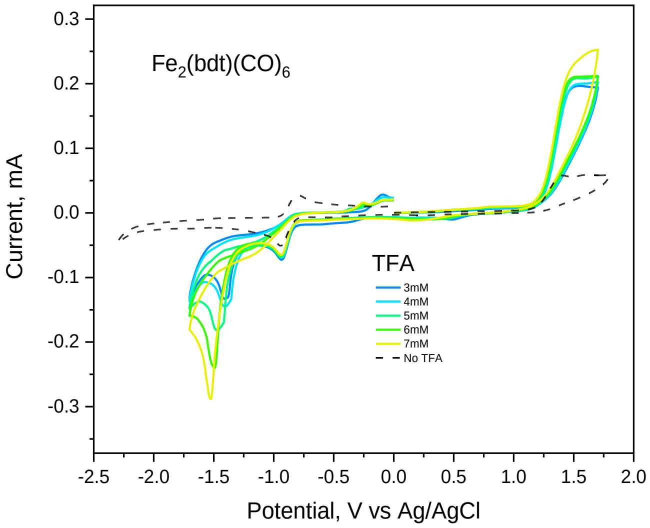

Figure S3. Cyclic voltammetry of the current enhancement analysis of the **H1** hydrogenase by the addition of TFA in arrange of concentration from 3mM to 10 mM solutions in 0.1 M of nBu_4NPF_6 supporting electrolyte solution in dry acetonitrile at a scan rate of 100 mV s^{-1} under N_2 atmosphere against Ag/AgCl.

Appendix A-C5
Supporting Information
Chapter 5

Spectra of the crude ligands.

- *[1,10-phenanthroline]-4,7-dicarboxylic acid*

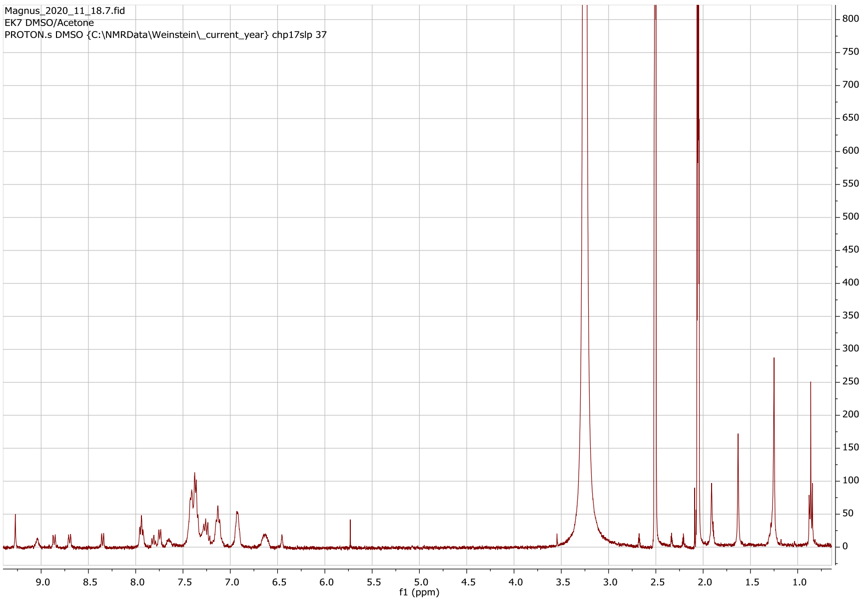

^{1}H NMR spectrum in DMSO-d$_6$/acetone-d of the ligand [1,10-phenanthroline]-4,7-dicarboxylic acid, synthesised prior to this project, predicted to show 3 signals.

- Xantphos

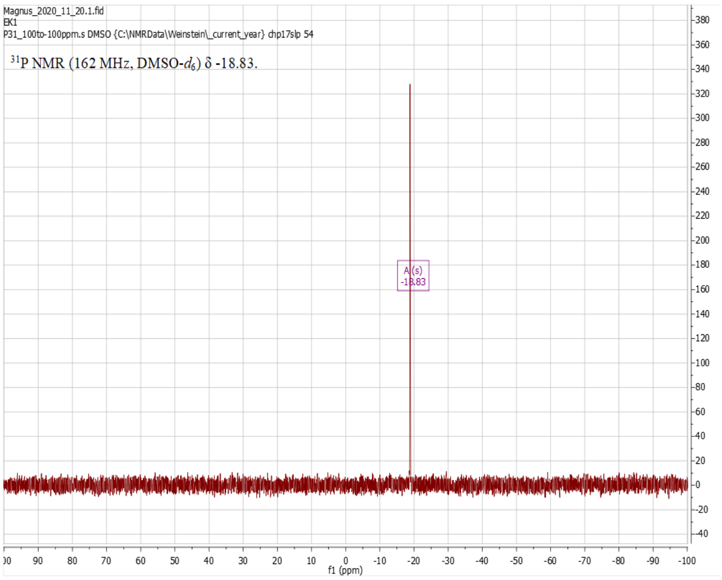

^{31}P NMR spectrum in DMSO-d of xantphos.

APENDIX B

THE UNIVERSITY OF SHEFFIELD: COVID-19 IMPACT FORM

This form is not compulsory but is intended to be a helpful note to examiners. You may submit this form alongside (not in) your thesis. The purpose of the form is to detail how your thesis has been impacted by the Covid-19 disruption.

STUDENT'S DETAILS	
Name: Samantha L Peralta-Arriaga	Registration Number: 170276588
Department: Chemistry	Faculty: Science
Please provide a brief summary of the work you were planning to complete before covid-19 restrictions were implemented (max 300 words)	

The main goal of the project was to develop a hybrid artificial photosynthetic system for hydrogen production from water splitting based on the use of Aluminates $MgAl_2O_4$ as doped with Cu and Ni as support for in photoanodes, Cu complexes as photosensitizer and FeFe hydrogenase mimic complexes as cocatalyst for proton reduction. To achieve this goal, we stablish specific objectives:

- The synthesis of the semiconductors $MgAl_2O_4$ modified by doping with Ni and Cu in 0.1, 1 and 10% wt. in ratio with the metal cation to improve their photocatalytic performance.
- The synthesis and characterization of the new [FeFe] hydrogenase mimic complex $Fe_2(dpet)(CO)_6$ and $Fe_2(bdt)(CO_6)$ as comparison.
- Investigate the photophysical and electrochemical properties of the FeFe complex $Fe_2(dpet)(CO)_6$ for its application in water splitting.

- Development of a synthetic approach to covalently link the PS to the SC surface.
- Systematically vary the light-absorbing properties of the PS, to evaluate the performance of the PS at different excitation energies and their limits to avoid the photo-corrosion processes.
- Investigate the photophysical and electrochemical properties of the hybrid photocatalytic systems. The absorption properties of each component of the system will be evaluated.
- The photophysical characterization includes emission properties of the photosensitiser, and the rates of electron transfer obtained from quenching experiments. These will be obtained by emission spectroscopy, and time-resolved laser spectroscopy.
- For the electrochemical characterization, cyclic voltammetry will be used to obtain the redox potentials of the different materials, chronoamperometry will be performed for the photo corrosion tests, and electrochemical impedance spectroscopy analysis will be done to know the position of the valence band and the conduction band (HOMO and LUMO).
- The efficiency of the H_2 evolution will be evaluated by conventional gas chromatography. All the above will be performed on a variety of PS-linker-Catalyst systems to evaluate the influence of the systematic variation in the reductive ability of the photosensitizer; the electronic coupling between the components by varying the structure of the linker and the efficiency of various sacrificial electron donors which traditionally are organic amines. Thus, the overall performance, photostability and efficiency, will be optimized.

Please provide a summary of plans for specific studies you were intending to conduct in the future (see note 1) (max 300 words)

- Study the efficiency on hydrogen evolution of the hybrid integrated PEC system proposed in this project (SC-PS-Hase).
- Conduct electrochemical tests of the response to the irradiation of visible light of the prepared photoanodes. More in specific, ON/OFF Photocurrent tests and J/V curves.
- Optimization of the online reactor set up for hydrogen evolution measurements.

Where relevant, please provide details of changes to your personal circumstances (see note 2) (max 150 words)

During this period as everyone else life was abruptly changed by the COVID-19 and the measures applied during the last 2 years. Specifically, when the first lockdown came in place in March 2020, I was starting my 3rd year which usually is the most productive year as a PhD student is the period when you are now done all the preliminary experiments and record some data, so you know what you need to do in order to achieve the established goals. Unfortunately, the laboratory was closed for almost 6 months and when we came back the use of the facilities was very limited and giving priority to some student whom were about to graduate so I got behind and even when I adjusted the number of experiments to save the wasted time but even that some experiments weren’t possible to complete.

If your thesis includes Covid-related research, please include a brief statement of how it relates to your overall research aims (see note 3) (max 150 words)
No
Please provide details of any previous funded extension, tuition-free extension or non-medical Covid-related leave of absence approved since March 2020
I didn’t have any extensions or funded extensions or LOA during the 4 years of my course.

Note 1. This information could form a basis for discussion at the viva examination and give Examiners additional means to assess the volume and standard of the work completed. Detailed information could be included in a future work section in the thesis itself.

Note 2. For example, ill health or additional caring responsibilities. additional difficulty related to an underlying disability, returned to clinical service, or has worked in a voluntary capacity for Covid-related research. These data could contextualise the judgement made by Examiners as to the most appropriate outcome.

Note 3. If in doubt, consult with your supervisor and Departmental PGR